AD-A072 541 OREGON GRADUATE CENTER BEAVERTON F/G 14/2
FIELD ELECTRON AND ION SOURCE RESEARCH FOR HIGH DENSITY INFORMA--ETC(U)
NOV 78 L W SWANSON F33615-76-C-1327
UNCLASSIFIED AFAL -TR-78-174 NL

1 OF 2
AD
A072541

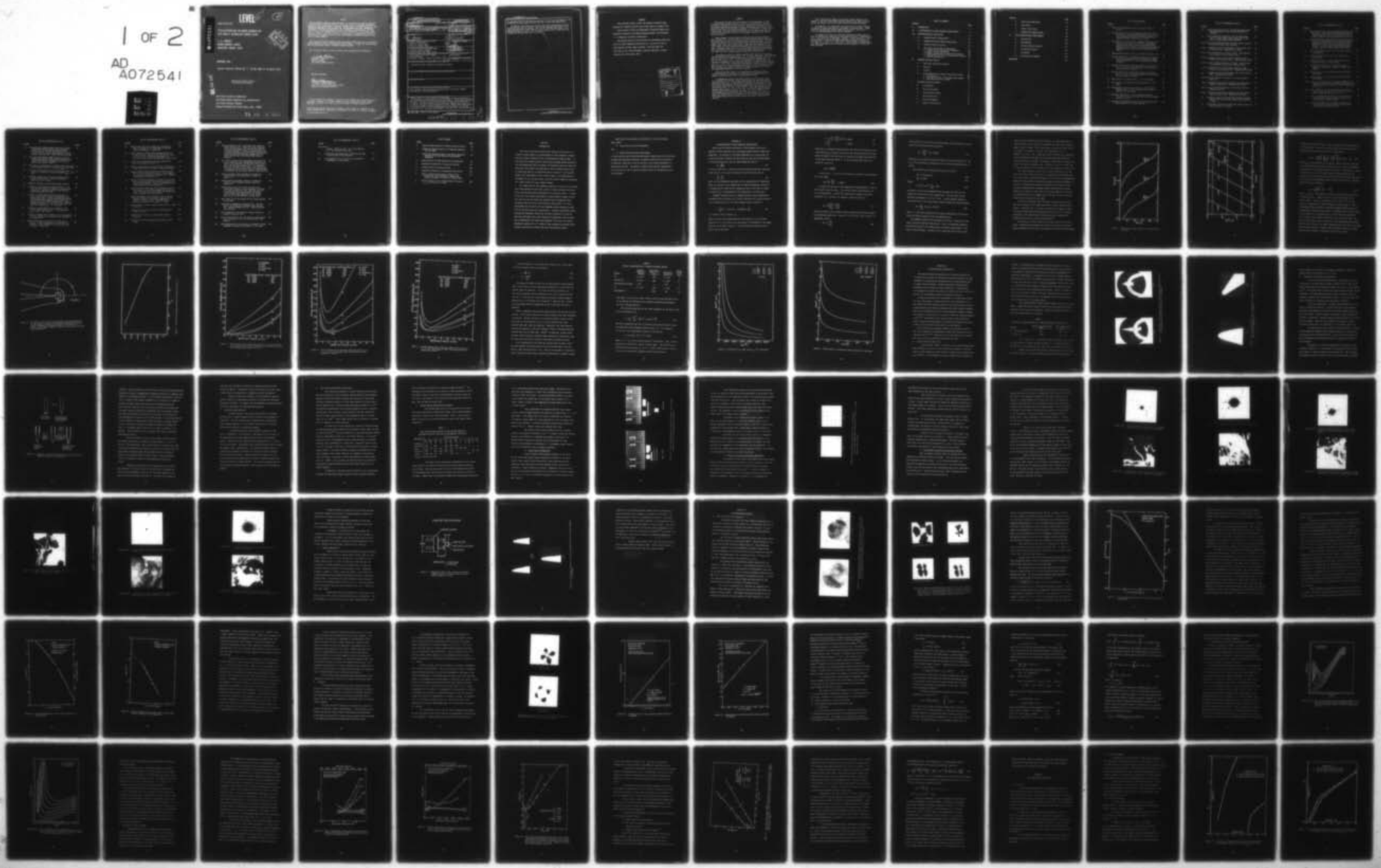

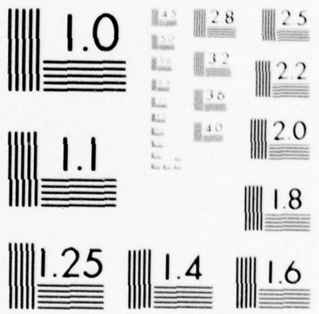

MICROCOPY RESOLUTION TEST CHART

②
B.S.

AFAL-TR-78-174

FIELD ELECTRON AND ION SOURCE RESEARCH FOR HIGH DENSITY INFORMATION STORAGE SYSTEM

L. W. SWANSON
OREGON GRADUATE CENTER
BEAVERTON, OREGON 97005

NOVEMBER 1978

INTERIM TECHNICAL REPORT NO. 4 - 15 MAY 1976 TO 15 AUGUST 1977

Approved for public release;
distribution unlimited.

AIR FORCE AVIONICS LABORATORY
AIR FORCE WRIGHT AERONAUTICAL LABORATORIES
AIR FORCE SYSTEMS COMMAND
WRIGHT-PATTERSON AIR FORCE BASE, OHIO 45433

NOTICE

This report has been reviewed by the Information Office (OI) and is releasable to the National Technical Information Service (NTIS). At NTIS, it will be available to the general public, including foreign nations.

This technical report has been reviewed and is approved for publication.

Dr. Millard G. Mier
MILLARD G. MIER
Project Engineer
Electronic Research Branch

FOR THE COMMANDER:

Robert J Almassy
ROBERT J. ALMASSY, Maj, USAF
Actg Chief, Electronic Research Branch
Electronic Technology Division

"If your address has changed, if you wish to be removed from our mailing list, or if the addressee is no longer employed by your organization please notify AFAL/DHR *,W-PAFB, OH 45433 to help us maintain a current mailing list".*

AIR FORCE/56780/3 August 1979 — 170

Unclassified
SECURITY CLASSIFICATION OF THIS PAGE (When Data Entered)

REPORT DOCUMENTATION PAGE

READ INSTRUCTIONS BEFORE COMPLETING FORM

1. REPORT NUMBER (18) AFAL-TR-78-174	2. GOVT ACCESSION NO.	3. RECIPIENT'S CATALOG NUMBER (9)
4. TITLE (and Subtitle) (6) FIELD ELECTRON AND ION SOURCE RESEARCH FOR HIGH DENSITY INFORMATION STORAGE SYSTEM.		5. TYPE OF REPORT & PERIOD COVERED Interim Technical Report, No. 4 15 May 1976 — 15 August 1977
AD-A048 9042		6. PERFORMING ORG. REPORT NUMBER
7. AUTHOR(s) (10) L. W. Swanson		8. CONTRACT OR GRANT NUMBER(s) (15) F33615-76-C-1327
9. PERFORMING ORGANIZATION NAME AND ADDRESS Oregon Graduate Center 19600 N.W. Walker Road Beaverton, Oregon 97005	(16)	10. PROGRAM ELEMENT, PROJECT, TASK AREA & WORK UNIT NUMBERS (17) 3164-01-01
11. CONTROLLING OFFICE NAME AND ADDRESS Air Force Avionics Laboratory (DHR) Air Force Systems Command Wright-Patterson AFB, Ohio 45433	(11)	12. REPORT DATE November 1978
		13. NUMBER OF PAGES 144
14. MONITORING AGENCY NAME & ADDRESS (if different from Controlling Office) Advanced Research Projects Agency 1400 Wilson Blvd. Arlington, Virginia 22209	(12) 161p.	15. SECURITY CLASS. (of this report) Unclassified
		15a. DECLASSIFICATION/DOWNGRADING SCHEDULE

16. DISTRIBUTION STATEMENT (of this Report)

Approved for public release; distribution unlimited.

17. DISTRIBUTION STATEMENT (of the abstract entered in Block 20, if different from Report)

18. SUPPLEMENTARY NOTES

19. KEY WORDS (Continue on reverse side if necessary and identify by block number)

Field electron, field ionization, electron source, ion source, thermal field emission, energy distribution

20. ABSTRACT (Continue on reverse side if necessary and identify by block number)

The purpose of this program is the development and characterization of high brightness field emission and field ion sources. Several emitter materials and modes of operation for both field electron and ion sources have been investigated. The most promising sources have been examined with respect to fabrication techniques, source stability and life, spatial energy distribution of the emitted beam. Optical characteristics of the source, e.g. virtual source size, etc., have also been examined. From this study two electron and

DD FORM 1 JAN 73 1473 EDITION OF 1 NOV 65 IS OBSOLETE

Unclassified
SECURITY CLASSIFICATION OF THIS PAGE (When Data Entered)

390 077 79 08 8 004

one gas phase field ion emitters have met most of the source requirements to be of interest for high current density submicron focussed beam applications.

In addition, the liquid gallium source has been investigated with respect to both electron and ion emission. The electron emission mode exhibits an unusual high peak current pulse mode while the ion emission mode results in an extremely intense d.c. mode. The ion emission mode is 100 to 1000 times more intense than the gas phase field ion sources.

PREFACE

This technical report covers the research performed under Contract No. F33615-76-C-1327 from 15 May 1976 to 15 August 1977. This contract is with the Department of Applied Physics and Electronic Science of the Oregon Graduate Center, with Professor L. W. Swanson as principal investigator.

The primary thrust of the work was the development and evaluation of high brightness electron and ion sources for use in high density archival memory systems. Work was under the direction of Mr. John Blasingame, Avionics Laboratory, Wright-Patterson Air Force Base, Ohio.

SUMMARY

The purpose of this research program is the development of high brightness field emission sources of both ions and electrons suitable for use in information storage systems. Progress has been made in the development and characterization of high brightness sources using field electron and field ion emission phenomenon. In addition, a novel pulsed electron and very high brightness gallium (Ga) ion source has been developed which appears to be one of the highest brightness ion sources nature provides.

Three classes of field electron (FE) sources have been examined which include (1) a clean tungsten (W) (100) oriented emitter which has been field built-up so as to confine emission along the (100) crystallographic direction; (2) a W(100) emitter that has an adsorbed zirconium/oxygen (ZrO) layer which specifically lowers the work function of the (100) plane; (3) rare earth hexaboride emitters which mostly includes LaB_6. Included in the class of (1) above are iridium (Ir) and tantalum (Ta) which form field built up ends forms which confine emission along the (110) and (111) crystallographic directions respectively.

At present the built-up W(100) and Zr/W(100) emitters operated in the thermal-field (TF) mode appear to be the most promising. Both emitters exhibit long life ($\gtrsim$ 1000 hrs) operating at angular intensities I' of 10^{-4} to 10^{-3} A sr^{-1} in $\sim 1 \times 10^{-8}$ torr pressure of residual gas. An anomalous broadening of the energy distribution of these emitters occurs for $I' > 2 \times 10^{-4}$ A sr^{-1} which has been studied. This will cause chromatic aberration to be the most dominant aberration for low voltage guns and must be taken into careful consideration when designing a microprobe gun using high brightness FE electron sources.

Both Ta and LaB_6 appear to be promising TF emitters, however, further work will be required to establish their capabilities with respect to the built-up W(100) and Zr/W(100) sources.

A substantial study of gas phase field ion (FI) sources using an Ir emitter and hydrogen, argon and xenon as the ionized particles has been carried out. A differentially pumped FI source and electrostatically focussing ion microprobe column have been developed. With the emitter operating at 77 K the maximum source sensitivity observed for H_2 and Ar is $\sim 5 \times 10^{-5}$ A sr^{-1} $torr^{-1}$. With the existing source design a gas pressure of 10 to 20 $\times 10^{-3}$ torr can be employed which provides an ion source angular intensity of 2 to 4 $\times 10^{-7}$ A sr^{-1}. Source sensitivity with Xe was much lower presumably due to the formation of solid films on the emitter at 77 K. Noise studies showed that large signal to noise ratios can be obtained for gas phase FI sources.

The Ir emitter was found to be the most durable emitter with respect to the well known field induced chemical etch which severely limits the useful life of most other field ion emitter materials.

In addition, it is shown that the field built-up (110) oriented Ir emitter provides good angular confinement of the ion beam. Using existing electrostatic einzel lenses we anticipate $> 10^{-11}$ A in ~ 0.1 μm focussed beams of Ar^+ can be obtained.

An unusual 50 to 250 A by 5-10 nsec repetitive pulsed electron mode of emission was observed for the liquid Ga source. Unfortunately, a d.c. mode could not be obtained. However, a very intense d.c. ion emission mode could be obtained which gave an angular intensity in the range of 1×10^{-4} to 1×10^{-5} A/sr. Several source configurations have been investigated and continuous source operation of 25 hrs has been achieved.

TABLE OF CONTENTS

LIST OF ILLUSTRATIONS

LIST OF ILLUSTRATIONS (Cont'd)

LIST OF ILLUSTRATIONS (Cont'd)

LIST OF ILLUSTRATIONS (Cont'd)

LIST OF ILLUSTRATIONS (Cont'd)

LIST OF ILLUSTRATIONS (Cont'd)

LIST OF ILLUSTRATIONS (Cont'd)

LIST OF TABLES

SECTION I

INTRODUCTION

This report describes progress made during the first year on a research program aimed at the development of high brightness charged particle sources suitable for use in information storage systems. In particular the charged particle source and focussing system envisioned for this application must be capable of providing a particle beam with sufficient flux density and smallness of size to address and/or read at least less than 0.1 μm resolution and at a rate of ~ 10^7 bits/sec. Because such requirements place a severe limit on the brightness requirements of the particle source, very few sources remain in contention as a viable option for such a memory system.

The primary aim of this research program is to evaluate high brightness field emission sources with respect to their potential for satisfying the above mentioned requirements for a particle source. In view of the fact that present high density archival memory schemes include both ion and electron beams this research will be examining field ionization (FI) as well as field electron (FE) sources. It is now established that FE and FI are the brightest sources presently available for electrons and ions respectively. Although considerable understanding and knowledge concerning the basic processes of FI and FE have been developed since their theoretical formulation some 50 years ago by Oppenheimer[1] and Fowler and Nordheim,[2] and their experimental embodiment pioneered by E. W. Müller,[3] many questions concerning their ultimate suitability as stable and long lived emitters remain.

Specifically this research is divided into the two following major tasks:

1) Field Electron Source Development

and

2) Field Ionization Source Development

In each task new source materials and modes of operation will be developed coupled with detailed evaluation of emission characteristic properties. In addition, some effort will be devoted to the further development of existing FE sources. The method of approach and specific measurements to be carried out will be given in greater detail in following sections of this report.

SECTION II

A CONSIDERATION OF FIELD EMISSION SOURCE OPTICS

The attractive feature exhibited by field emission sources in regards to their potential use in microbeam applications is their high brightness. An electron or ion beam brightness B at a given point in a given direction is defined as the current dI per unit area dA normal to the given direction, per unit solid angle dΩ, that is

$$B = \frac{dI}{d\Omega dA} \tag{1}$$

It can be shown that a charged particle beam whose electric potential varies from V_1 to V_2 cannot increase the ratio of B_1/V_1 that is

$$\frac{B_1}{V_1} = \frac{B_2}{V_2} \tag{2}$$

which is the fundamental expression of the conservation of brightness. Thus, for a given Ω_2 the maximum rate at which information carried by a charged particle beam can be transmitted into a unit area of target at potential V_2 is determined by the brightness B_1 at the source.

Langmuir[4] showed that for a charged particle source exhibiting a semi-Maxwellian distribution of initial velocities the current density J at the image plane or at the beam crossover point is given by

$$J = \frac{J_o}{M^2} \left[1 - (1-x) \exp - [eV_2X/kT(1-x)]\right] \tag{3}$$

$$(x = M^2\sin^2\theta \text{ and } 0 \leq M\sin\theta \leq 1)$$

where M is the overall magnification of the system, J_o, the current density at the source and θ, the semi angle of convergence in the image plane or at the beam crossover. The following two limiting forms of Eq.(3) can be obtained:

$$J = J_o \left(1 + \frac{eV_2}{kT}\right) \sin^2\theta, \text{ x small} \tag{4}$$

$$J = \frac{J_o}{M^2} \quad , \quad \text{x large} \tag{5}$$

Physically the Langmuir equation gives the limit on the initial transverse energy E_{xy} a particle can have at the source and still be transmitted through a lens and arrive at a point on the image plane through a beam semi-convergent angle θ. It can be easily shown that this condition is given by

$$E_{xy} \leqq E_2\left(\frac{x}{1-x}\right)$$

Since $eV_2/kT > 1$, Eq.(4) can be written in terms of the brightness B_2 at the image:

$$B_2 \cong \frac{J_o}{\pi} \frac{eV_2}{kT} \quad , \text{ x small} \tag{6}$$

An important question arises regarding the applicability of Eq.(3) for FE and FI sources since, the initial velocity distributions are not semi-Maxwellian. Worster[5] has shown that in general the axial brightness in a cylindrically symmetric system is given by

$$B_2 = \frac{J_o}{\pi}\left(\frac{eV_2}{\overline{E}_t} + \frac{\overline{E}_n}{\overline{E}_t}\right) \tag{7}$$

where $\overline{E}_t$ and $\overline{E}_n$ are the average initial transverse and normal energies of the emitting particles. Since $eV_2 >> \overline{E}_t$ the last term of Eq.(7) is negligible, giving

$$B_2 \cong J_o \frac{eV_2}{\pi \overline{E}_t} \tag{8}$$

Worster[6] goes on to show that the directional beam intensity at a given point off the optical axis is given by

$$B_2 = \frac{J_o eV_2}{\pi \overline{E}_t} \exp\left(-E_t/\overline{E}_t\right) \tag{9}$$

where E_t is the initial transverse energy of the emitted particle. For $E_t = 0$ Eq.(9) becomes the expression for the axial brightness given in Eq.(8).

For Schottky and FE emission the values of $\overline{E}_t$ are[7]

$$\overline{E}_t = kT \text{ (Schottky)} \tag{10}$$

$$\overline{E}_t = d \text{ (FE)} \tag{11}$$

where

$$d \cong 9.75 \times 10^{-9} \frac{F}{\phi^{1/2}} \text{ (eV)} \tag{12}$$

and where F and ϕ are the applied field strength (in V/cm) and the surface work function (in eV) respectively. For the usual current densities attainable d = 0.1 to 0.3 eV. In the paraxial region at the cross-over of a FE electron gun, Worster[6] shows that Eq.(9) becomes

$$B_2 = \frac{J_o}{\pi \overline{E}_t} eV_2 \exp\left(-r^2/M^2a^2\right) \tag{13}$$

where r, a and M are respectively the radial displacement at the cross over, the emitter radius and the gun magnification.

The Langmuir equations as expressed in the form of Eqs.(3) to (6) lead to several important observations. First, the maximum brightness and current density at the image plane is directly proportional to the source current density. Secondly, for a specified value of eV_2, there exists a value of $M^2 \mathrm{Sin}^2\theta$ above which $JM^2/J_o \cong 1$. This means that all particles emitted from the source, regardless of their initial emission angle, reach the image. Fig. 1 gives plots of Eq.(3) for three values of $eV_2/\overline{E}_t$. For example, if $eV_2/\overline{E}_t = 10^5$ then $JM^2/J_o \cong 1$ for $M^2 \sin\theta^2 \gtrsim 5 \times 10^{-5}$. Fig. 2 shows the values of M and θ for a specified value of $M^2\sin^2\theta$ and the values of the latter above which $JM^2/J_o \cong 1$ for various values of $eV_2/\overline{E}_t$. For example, if the value of $eV_2/\overline{E}_t = 10^5$ and $M = 10$, then, according to Fig. 2, $JM^2/J_o \cong 1$ for $\theta \gtrsim 7 \times 10^{-4}$ rad. On the other hand, if $M = 0.01$ then $\theta \gtrsim 0.7$ rad in order that $JM^2/J_o \cong 1$.

For a high brightness source with a small virtual size as is the case for FE and FI particle sources, a microprobe gun will operate near $M = 1$; thus, since θ generally exceeds 7×10^{-4} rad Eq.(5) appropriately gives the current density relationship between the source and image. In contrast a microprobe gun employing a Schottky source with its lower intrinsic brightness and accordingly larger virtual source size will operate at or below $M \cong 0.01$; thus for the usual range of $\theta < 0.1$ rad, the limiting form of the Langmuir Eq.(4) will give the current density relationship between source and image.

It should be emphasized that the above discussion gives the maximum current density at the image plane based on ideal (aberrationless) lenses. A real gun will, of course, be limited by the degree to which the probe forming optics system approaches the ideal case. A detailed discussion of the optimum probe forming optics and a comparison of Schottky and FE sources is given by Veneklasen.[8]

In the case of FE and FI sources the virtual source size is very small. Wiesner[9] has determined the virtual source size for an emitter shape approximated by the sphere-on-orthogonal-cone (SOC) model developed

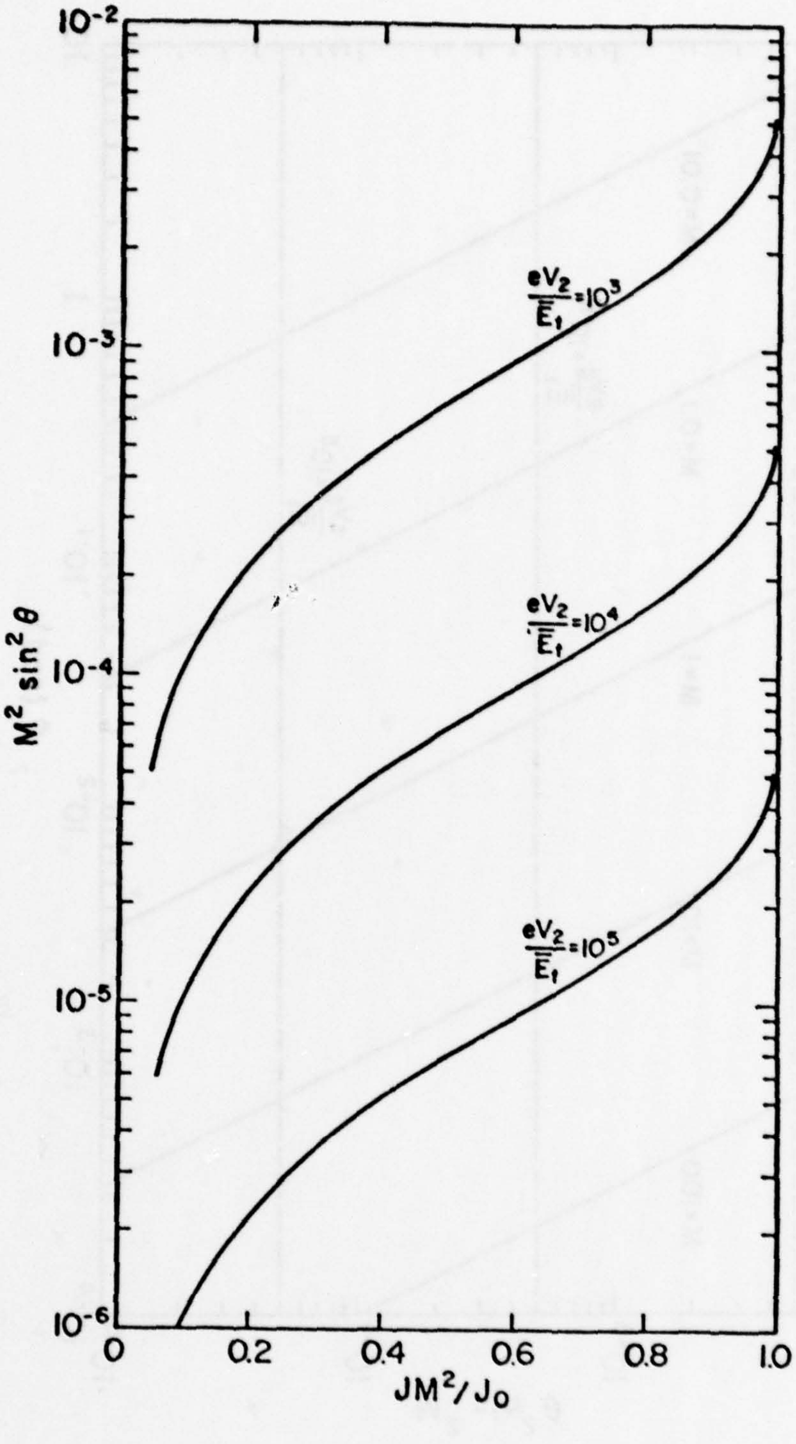

Figure 1. Plots of the Langmuir Eq. (3) for various values of eV_2/kT.

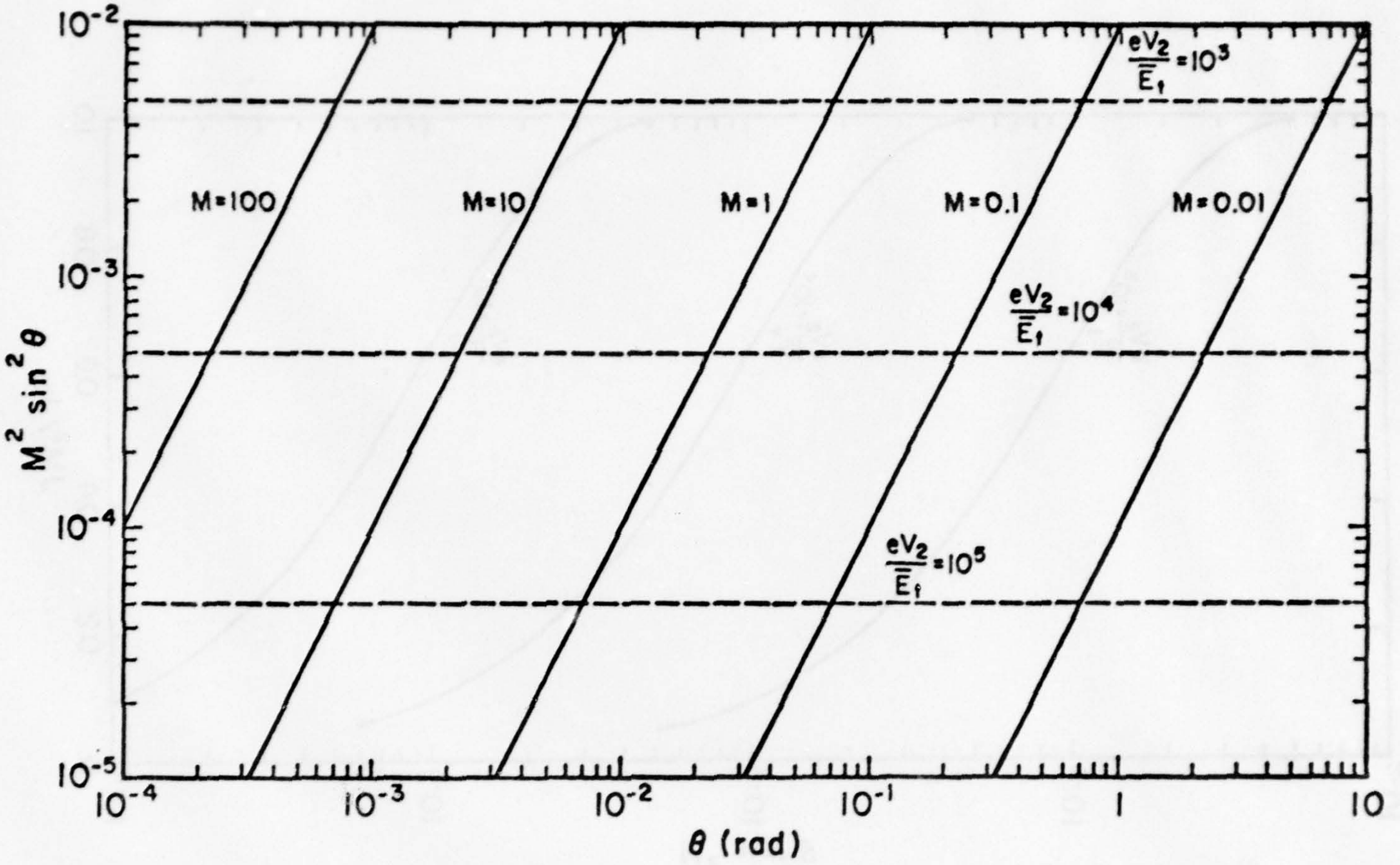

Figure 2. Plots of $M^2 \sin^2\theta$ vs θ for various values of M. The horizontal lines represent values of $M^2 \sin^2\theta$, for the indicated values of eV_2/kT, above which the Langmuir equation reduces to $J \cong J_o/M^2$.

by Dyke and coworkers.[10] Fig. 3 shows a diagram and relevant parameters of the SOC model. Based on this model, equipotential surfaces $V(\rho,\theta)$ depicting a particular emitter shape are generated by

$$V(\rho,\theta) = V_R\left(\frac{r_o}{R}\right)^n \left[\left(\frac{\rho}{r_o}\right)^n - \left(\frac{r_o}{\rho}\right)^{n+1}\right] P_n(\cos\theta_o) - V_{oo} \qquad (14)$$

where V_{oo} is the potential of the emitter surface relative to the SOC, V_R is the potential on an anode a distance R from center of the sphere and $P_n(\cos\theta)$ is the Legendre function of index n. The value of n, which varies from 0.1 to 0.5 for typical emitter shapes establishes the exterior cone angle θ and is determined by the condition that $P_n(\cos\theta_o) = 0$. Fig. 4 gives the relationship between n and θ_o for the latter condition. The value of V_{oo} is given by

$$V_{oo} = V_R\left(\frac{r_o}{R}\right)^n \left[\gamma^n - \gamma^{-n-1}\right] \qquad (15)$$

where $\gamma = \rho_{oo}/r_o$. The degree of "necking" of the emitter (see Fig. 3) is determined by γ - larger values of γ cause less necking of the emitter shape. Typically, the range of n and γ are 0.1 to 0.4 and 2.0 to 3.0 respectively. Based on Wiesner's results, Figs. 5-7 give the respective source sizes for typically shaped FE and FI sources of varying radii and aperture half angle. The smaller size of the FI source is due primarily to a negligible $\overline{E}_t$ at the low operating temperature of the source and the smaller diffraction limit of a proton beam. Because of their small virtual source size, probe forming guns using field emission sources need not be highly demagnifying thus only one or, at most, two lenses are required. Compared with conventional sources the field emission source requires a relatively simple optics system.

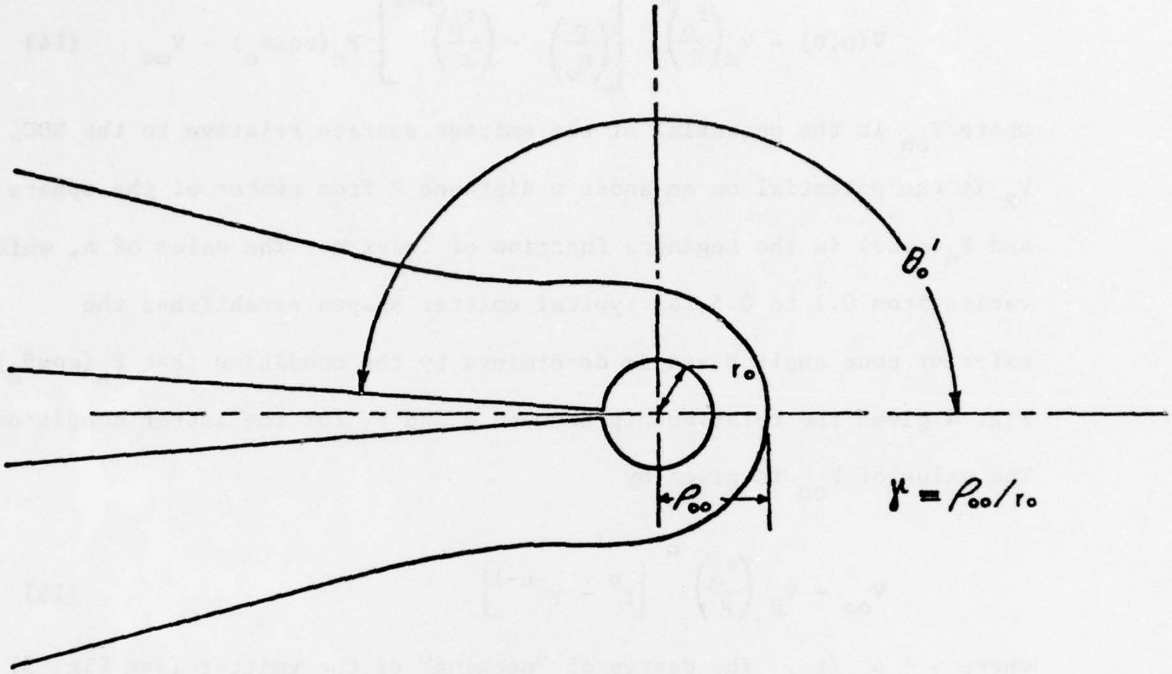

Figure 3. The sphere at the end of the orthogonal cone model depicted in this figure is capable of generating equipotentials which closely approximate those generated at the surface of a typical field emitter (shown in figure as the profile surrounding the model).[10]

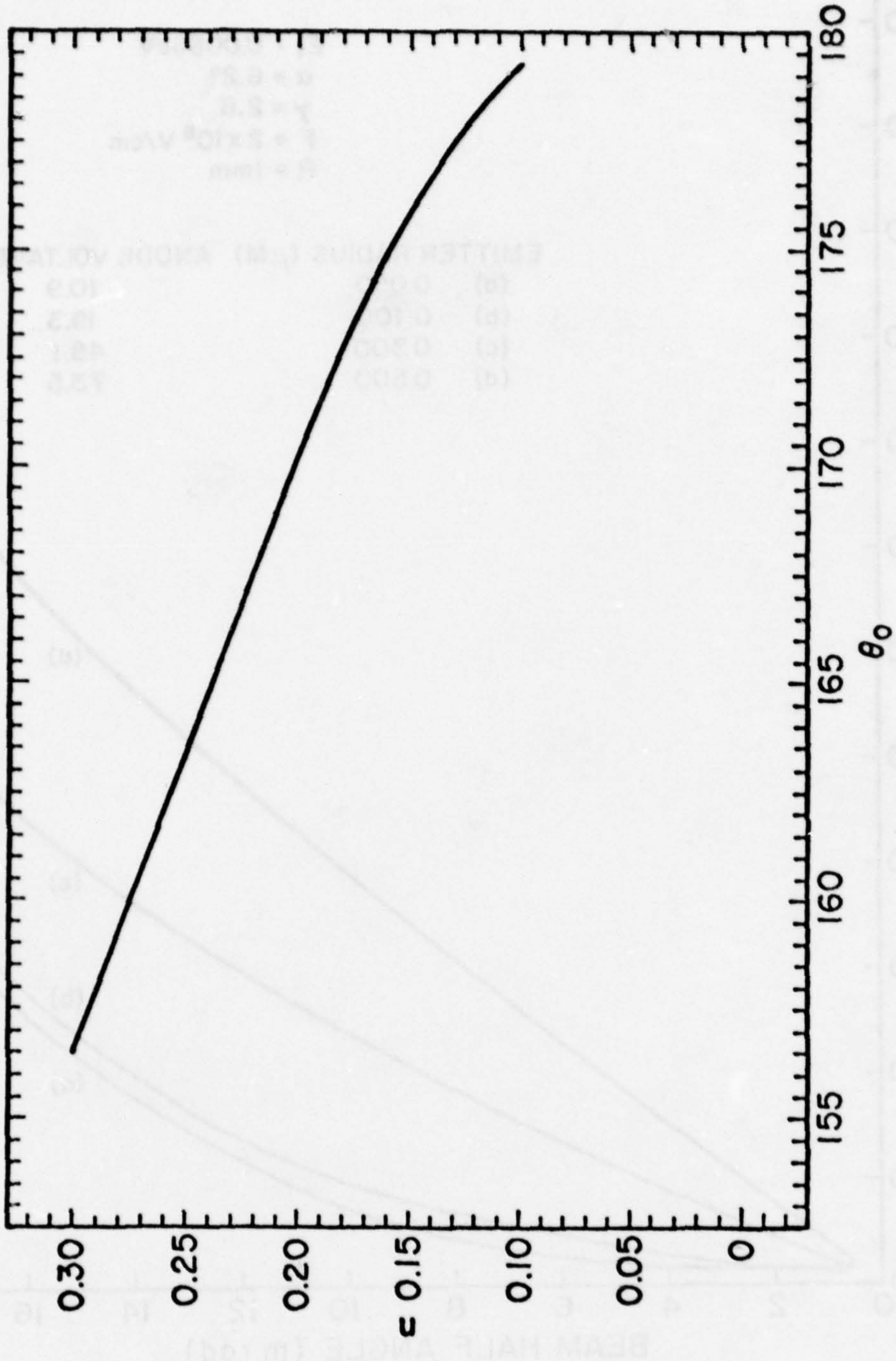

Figure 4. Relationship between n and θ_o for which Pn $(\cos\theta_o) = 0$.

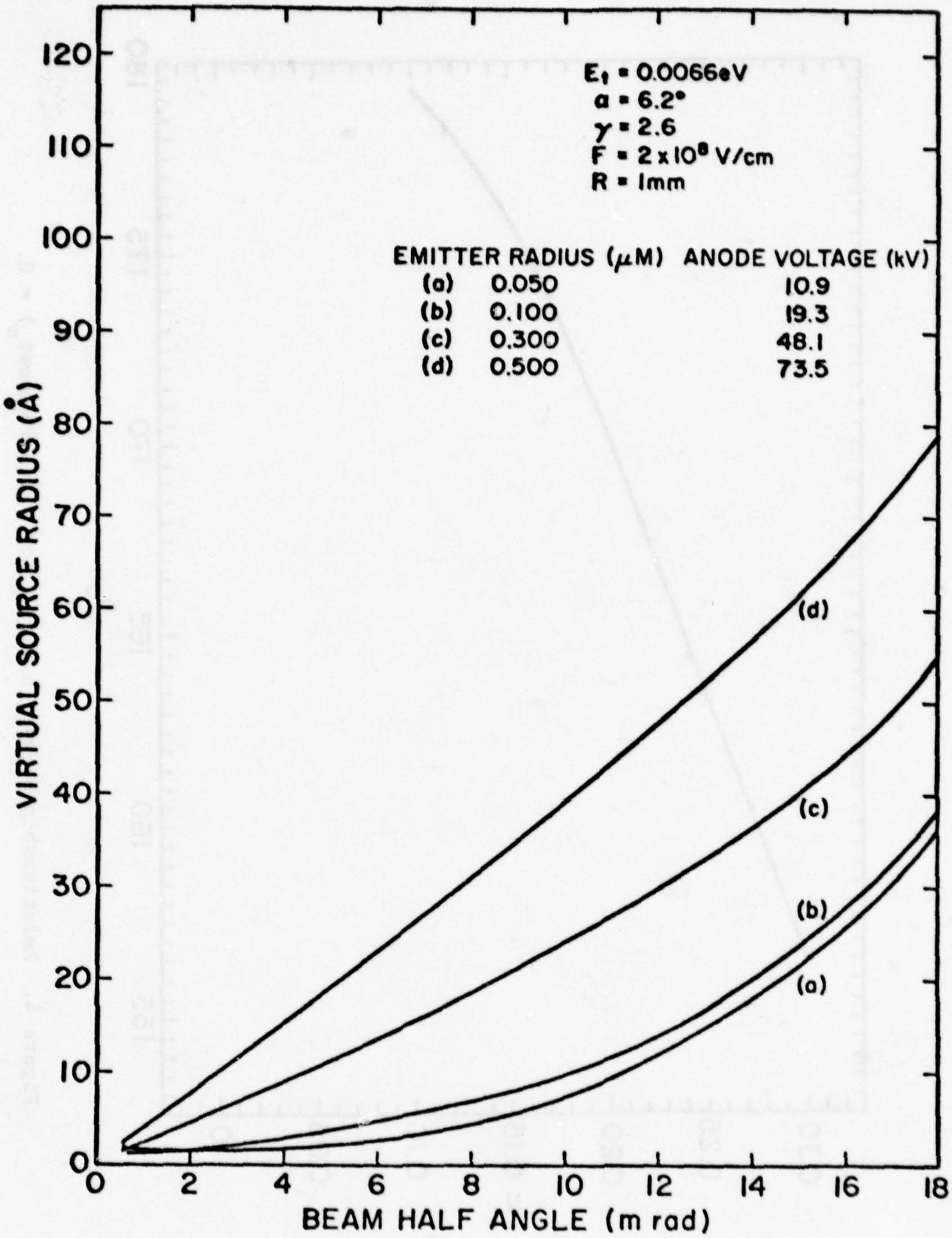

Figure 5. Virtual source size vs beam half angle for a FI source of H^+ ions using SOC model and aberration terms computed by Wiesner.[9] Source temperature assumed to be 77 K.

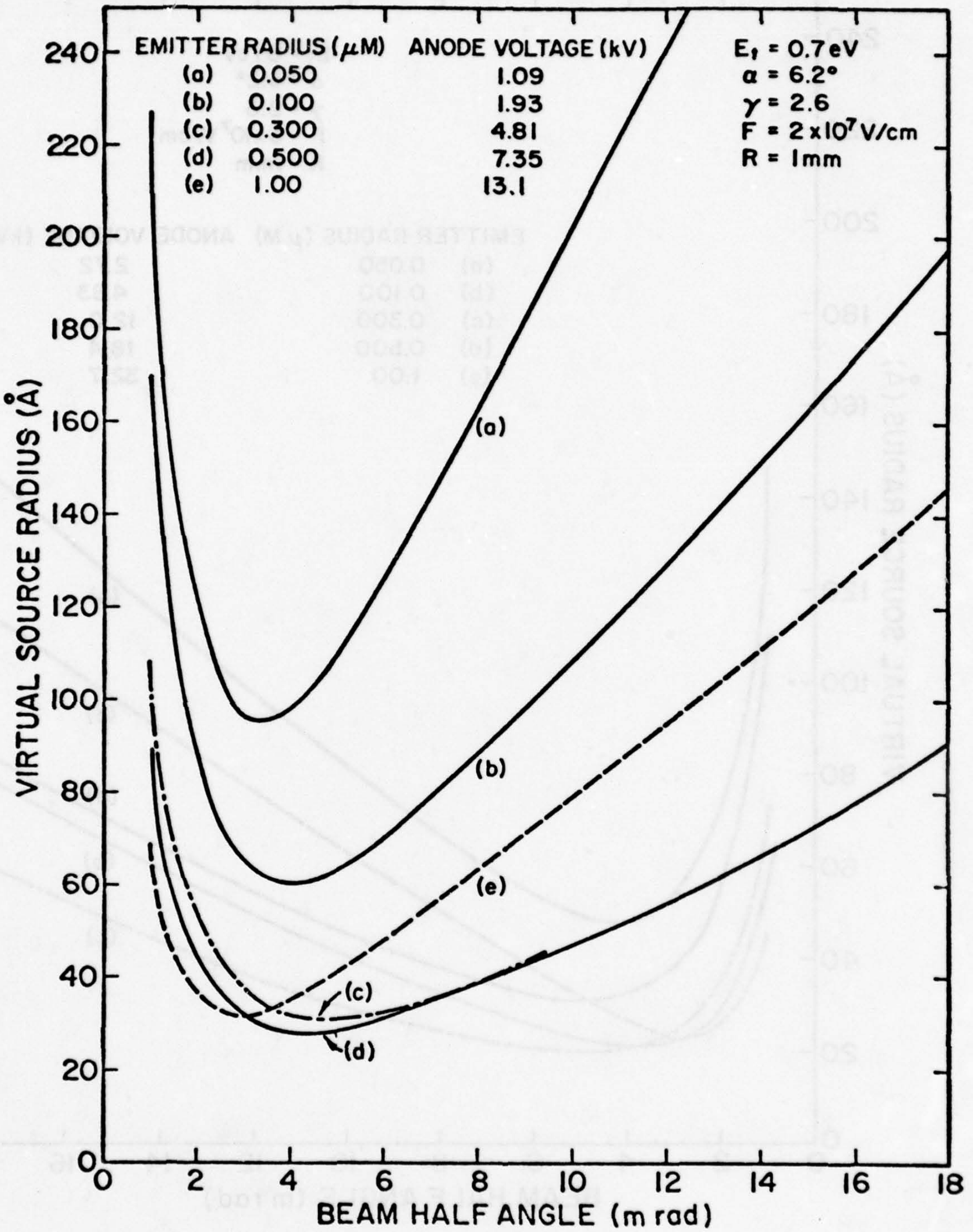

Figure 6. Virtual source size vs beam half angle for FE source at $F = 2 \times 10^7$ V/cm using SOC model and aberration terms computed by Wiesner.[9]

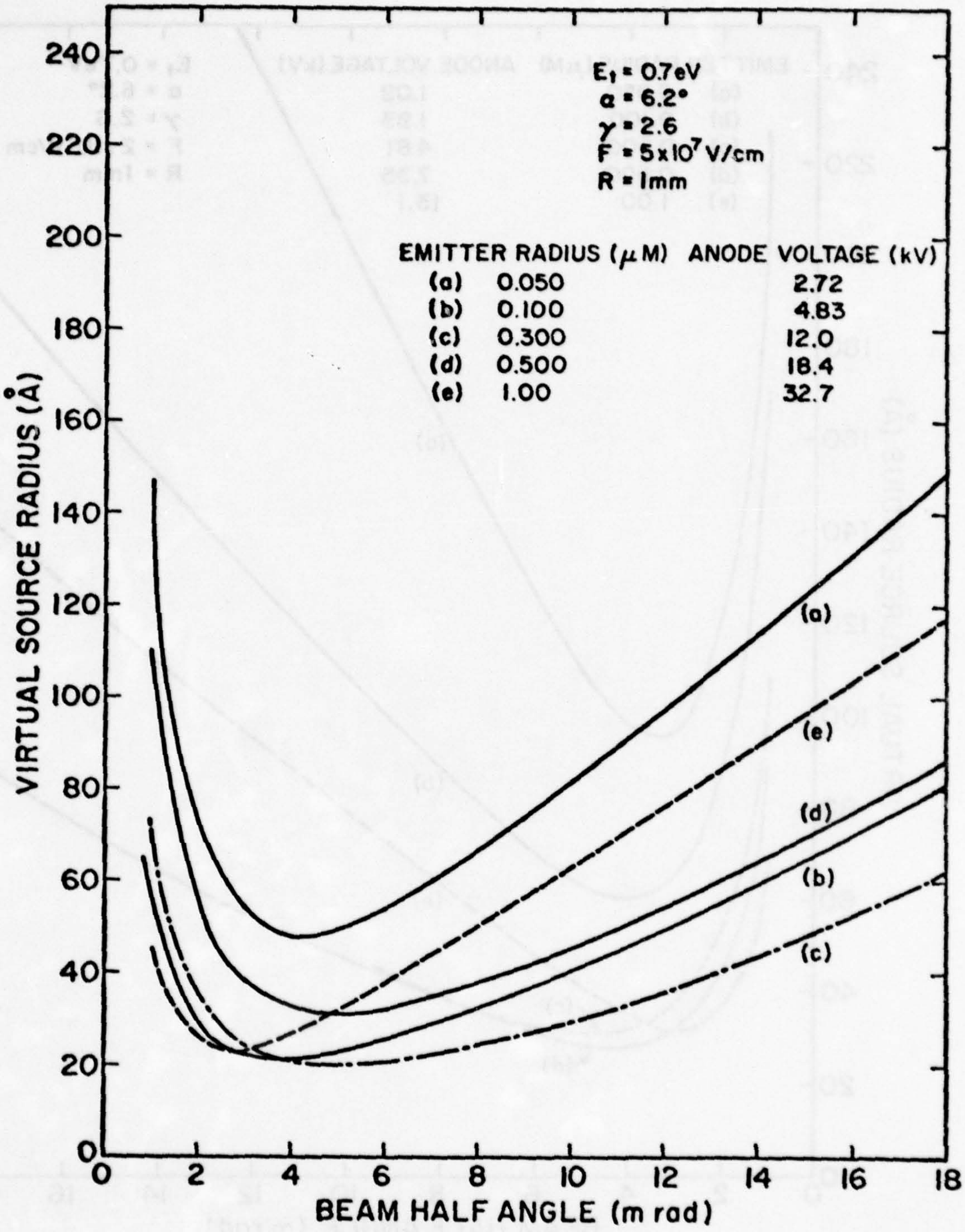

Figure 7. Virtual source size vs beam half angle for FE source at $F = 5 \times 10^7$ V/cm using SOC model and aberration terms computed by Wiesner.[9]

For small angles θ the current that diverges into a solid angle $\pi\theta^2$ from a virtual source ρ_s is given by

$$I = \frac{dI}{d\Omega}\pi\theta^2 \tag{16}$$

or

$$B_1 = \frac{dI/d\Omega}{\pi\rho_s^{\ 2}} \tag{17}$$

The range of values of $dI/d\Omega$ for an operational FE source extend from 1×10^{-4} A/Sr for room temperature operation to 1×10^{-3} A/Sr for thermal field TF operation. If a value of 30 Å is assumed for ρ_s the source brightness can be determined to be in the range 10^8 to 10^9 A/Sr cm^2. In the case of a gas supplied FI source a maximum angular intensity of 1×10^{-6} A/Sr can be obtained.[11] Based on Fig. 5 values of ρ_s a maximum source FI brightness of 10^7 to 10^8 A/Sr cm^2 can be expected.

Table 1 summarizes the emission characteristics for several particle sources. The FE and FI sources are clearly superior when high brightness is required. However, because of the relatively small values of both $dI/d\Omega$ and ρ_s field emission sources are only suitable when small focussed beam spot sizes are required. Generally, the field emission sources are superior to all other sources of ions or electrons when the focussed spot size is less than ~ 5000 Å. In addition, because field emission sources exhibit a smaller energy spread than conventional ones, the spot size limit due to chromatic aberration is greatly reduced.

It is interesting to note from the results shown in Figs. 6 and 7 that the smallest FE virtual source size for the SOC model occurs for emitter radii between 0.3 and .5 μm. This is in contrast to a spherical emitter where the source size is directly proportional to emitter radius.

TABLE 1

TYPICAL CHARACTERISTICS OF VARIOUS ELECTRON SOURCES

Source	Angular Brightness (A/Sr)	Approximate Source Size (μm)	Brightness (A/cm^2 Sr)	Energy Spread (eV)
FE	3×10^{-5}	.003	1×10^{8}	.2
Thermal FE	3×10^{-3}	.003	1×10^{10}	1-2
LaB_6 Schottky Cathode	$\sim 10^{-1}$	1	$\sim 10^{6}$	.2
FI	1×10^{-6}	.001	1×10^{8}	2-5
Duoplasmatron	-	1000	10^{4}	10

The larger source size at small emitter radii for the SOC model is due to an increase in diffraction and chromatic aberration contribution for lower voltage emitters.

By differentiating Eq. (15) the field strength F at the emitter apex can be determined to be

$$\beta = \frac{F}{V_R} = \frac{r_o^{n-1}}{R^n}\left[n\gamma^{n-1} + (1+n)\gamma^{-2-n}\right] \tag{18}$$

The above expression was used to calculate the anode voltages to give the indicated field strengths listed in Figs. 5-7. For values of R = 0.1 to 1 cm an approximate value of β is given by

$$\beta = 0.6/\rho_{oo}^{.87}\ R^{0.13}\ \alpha^{.33}\ (cm^{-1}) \tag{19}$$

where $\alpha = \pi - \theta_o$ is the cone half angle of the emitter. Figs. 8 and 9 show plots of Eq. (18) for typical emitter shapes. The field factor β increases with decreasing ρ_{oo}, R or α. Emitter radii between .05 and 1.0 μm can be obtained by standard fabrication procedures.

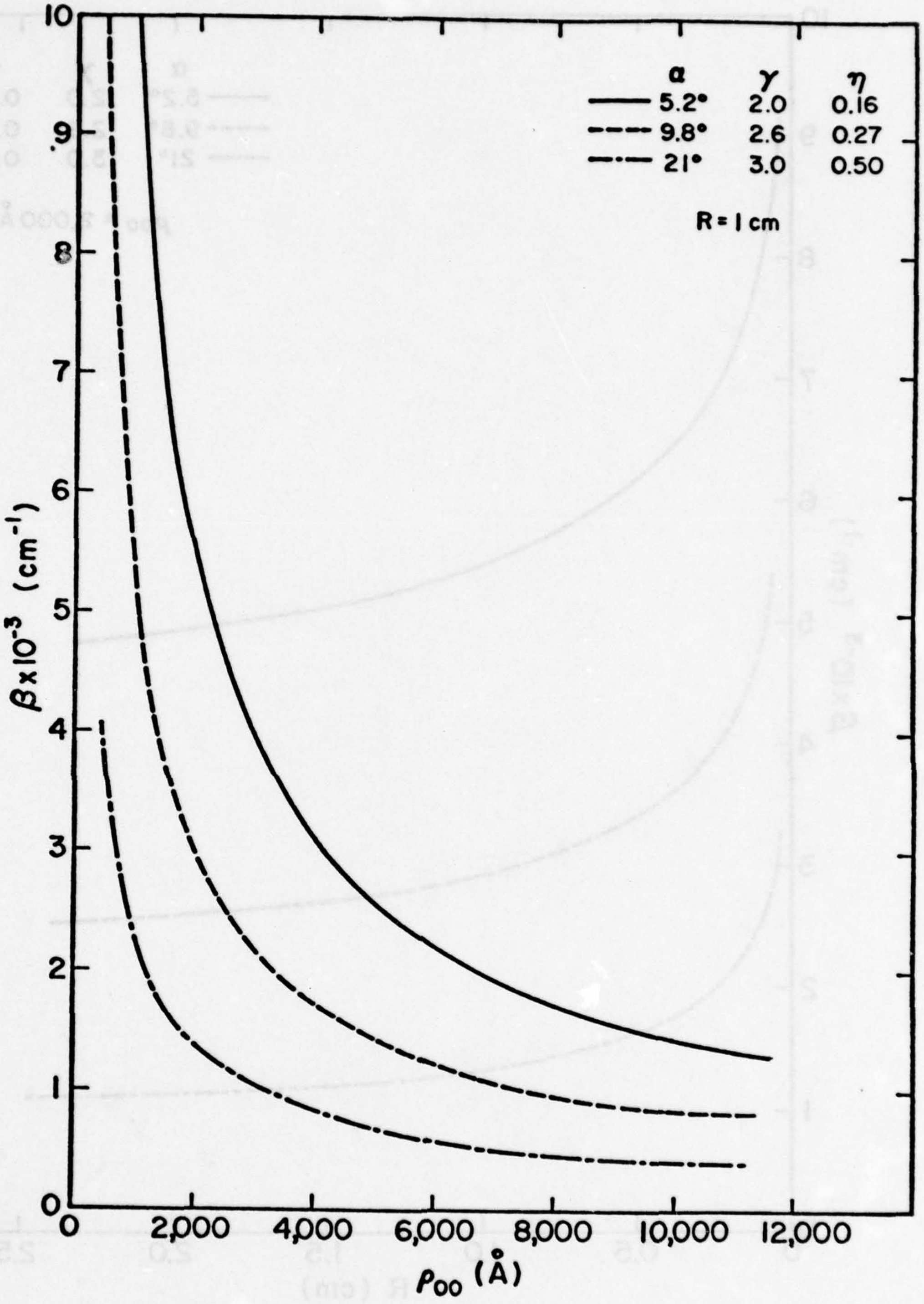

Figure 8. Field factor β vs apex radius ρ_{oo} for a SOC model.

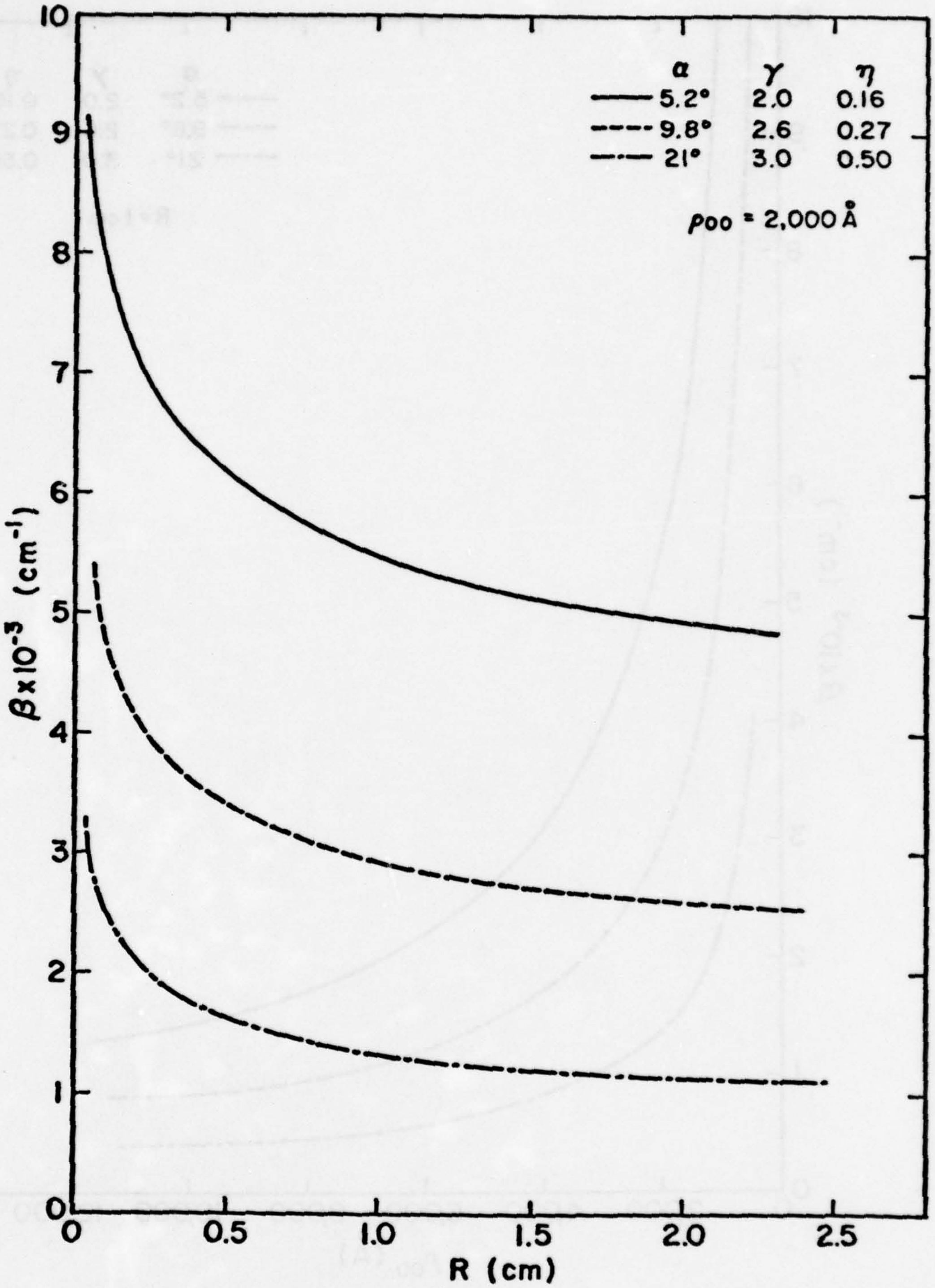

Figure 9. Field factor β vs emitter-to-anode spacing for a SOC model.

SECTION III

EMITTER MATERIALS FABRICATION

The physical properties desirable for an emitter material are 1) high tensile strength to withstand electrostatic stresses, 2) high resistance to sputtering and contamination and 3) high melting point to permit thermal cleaning. Possible materials possessing these properties can be divided into three categories: 1) pure metals, 2) heterogeneous cathodes consisting of a surface layer on a solid substrate, and 3) homogeneous metalloid compounds and alloys.

Of the pure metal materials investigated in the past which satisfy the above requirements, tungsten operated at room temperature or in the thermal-field (TF) mode has proved to be the most suitable material. TF mode operation has worked successfully with (100) oriented tungsten emitters by allowing electrostatic induced geometric change to reshape the emitter to a particular end form that is stable at elevated temperatures.[11,12] The mobility of the surface atoms at high temperature causes cathode sputtering damage to instantly heal thereby maintaining a smooth and clean surface that exhibits stable emission.

The zirconium coated tungsten cathode, also operated in the TF mode, is an example of a heterogeneous cathode that has proved to be a practical emitter.[12,13] Resupply of the Zr sputtered from the emitter apex occurs by surface diffusion from the emitter shank.

A. Tungsten Emitter Fabrication

Two procedures leading to slightly altered emitter shapes have been developed in the past to form emitters from tungsten. Both procedures involve immersing a short length of single crystal tungsten wire spot welded to a .13 mm diameter W heating filament into a solution of

2N NaOH. The dimensions of the single crystal W blank are ~ 2 mm in length (as measured from the point of spot weld) by .13 mm in diameter. Electrochemical formation of the emitter tip can be accomplished by applying a continuous a.c. voltage of 13 V or a d.c. voltage (emitter positive) of 9 to 13 V. The former is called the a.c. self termination technique and the latter the d.c. drop off technique. In the case of the a.c. method the emitter formation continues until the emitter recedes from the solution, thus terminating the process. The d.c. technique is terminated by quickly (within a few μsec.) switching off the etching voltage when the lower portion of the immersed emitter blank separates from the blank due to the etching action.

Fig. 10 shows typical emitter shapes formed by the two processes. Table 2 gives the typical range of emitter cone half angle and radius obtained by the respective procedures. Larger cone angles and emitter radii are formed by the a.c. process.

TABLE 2

GEOMETRICAL CHARACTERISTICS OF W EMITTERS FORMED BY TWO PROCESSES

Process	Emitter Cone Half Angle (Deg)	Emitter Apex Radius (μm)
d.c. self termination	4-6	.02 - .05
a.c. drop off	8-10	.13 - .16

Fig. 11 shows an a.c. processed emitter just after being formed (a) and then after thermal cycling to 1600 K (b). A slight necking of the emitter can be observed in Fig. 11(b) after the thermal processing.

Studies thus far show that emitter shape and radii in the range indicated in Table 2 can be routinely produced by these two processes.

(a) (b)

Figure 10. Photographs of the typical shape of a field emitter formed by the a.c. self termination (a) and d.c. drop off (b) techniques.

(a)

(b)

Figure 11. Emitters formed by a.c. self termination process ($M = 38 \times 10^3$ X); (a) before and (b) after thermal cycling to 1600 K.

Future studies will be aimed at developing procedures to fabricate emitter radii in the range of 0.2 to 1.0 μm.

B. Tungsten/Zirconium Emitter Fabrication

In the past Zr has been deposited on the emitter by in situ evaporation or by depositing an organic solvent slurry of ZrH_2 on the emitter mechanically and thermally diffusing the free Zr to the emitter apex.[14] Both methods have provided long lived cathodes and have certain advantages. The vapor deposited method can be carried out quite reproducibly compared with the mechanical method. On the other hand, the latter technique is relatively quick and simple to perform.

The in situ evaporation technique was abandoned due to difficulty in applying sufficient zirconium and because this method of application also deposits zirconium on the hairpin filament which supports the emitter. When the emitter is operated at high temperatures (TF mode of operation), unwanted thermionic emission then occurs from the hairpin filament. Hence any new technique for applying zirconium preferably should result in depositing it on the emitter shank only.

Two possible methods for doing this were considered: alloying the zirconium with tungsten before preparing emitters or applying the zirconium as ZrH_2 electrophoretically. So far, the latter method has been investigated and a workable procedure for applying the ZrH_2 has been developed.

The sequence of operations employed for depositing the ZrH_2 is shown in Figure 12. A 5 mil blank of 100 oriented W wire is first spot welded to a hairpin supporting and heating loop. Next a regular field emission point is etched by the d.c. drop-off method in 2N NaOH

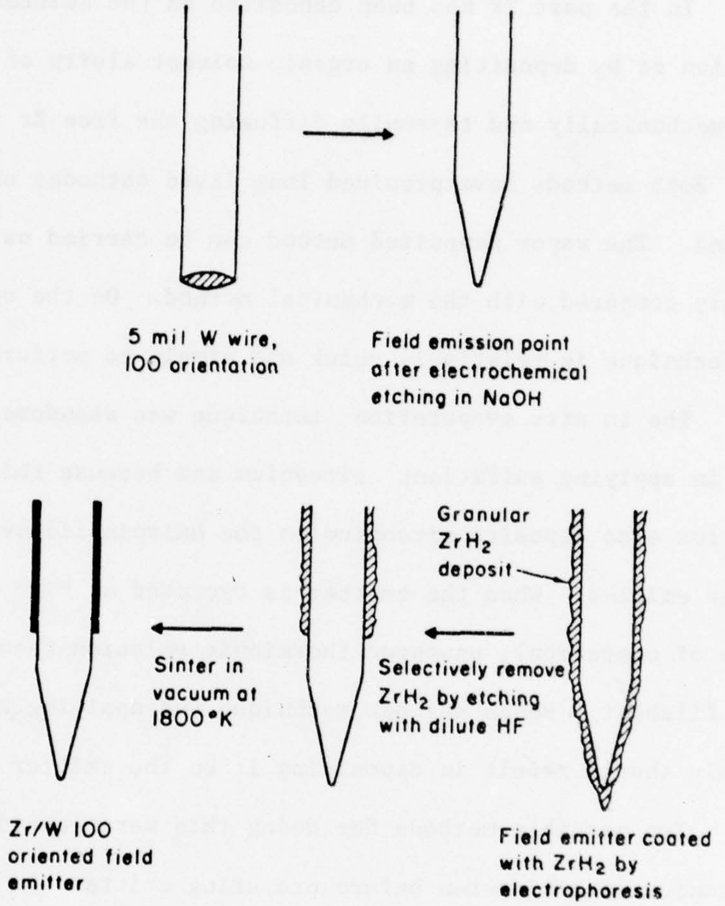

Figure 12. Sequence of operations involved in electrophoretically depositing ZrH_2 on a field emitter.

solution. The next step is the critical one in which the electrophoretical deposition of ZrH_2 is accomplished by making the emitter 45 V negative with respect to a platinum electrode. In the technique developed for this project, a slurry of ZrH_2 powder suspended in a 2:1 mixture (by volume) of methanol and amyl acetate was used as the electrophoresis liquid. About 100 mg of ZrH_2 per 20 ml of solution was used and the powder was thoroughly mixed and dispersed by agitating with an ultrasonic cleaner. When this was completed, the emitter and electrode were inserted and electrophoresis was carried out for 30-100 seconds. In an earlier variant of this technique, a small amount of HCl was added to increase conductivity of the slurry; however the conditions required to deposit the ZrH_2 in a reasonably short time also led to severe corrosion of the emitter. In the present HCl free technique, the current flowing was approximately 100 μA.

When the deposit of ZrH_2 is thick enough, the ZrH_2 directly surrounding the emitter is removed by etching briefly (< 1 sec) in dilute or concentrated HF. This is done because in the next step, when sintering is accomplished by heating in vacuum, the zirconium layer contains sharp protrusions which would possibly lead to an irregular emitter if not removed from the emitter region. After sintering at ~ 1000 C the emitter is ready for high temperature vacuum activation

Although the electrophoretic technique works, it is somewhat difficult to operate because of the difficulty in keeping the ZrH_2 particles suspended: as soon as the ultrasonic agitation is removed, the particles begin settling out. Also the solvent begins to evaporate and this makes it difficult to maintain the slurry level around the emitter - the emitter is only 2-3 mm long, so it only takes a small amount of evaporation to completely uncover the emitter.

Because of the above problems, the electrophoretic approach does not seem to be significantly superior to the previous mechanical deposition technique. We suggest that the remaining, alloying, approach should be investigated for preparing W/Zr emitters.

C. Tantalum Carbide Emitters

Tantalum carbide is an interesting material; its extreme melting point (~ 4000°C) suggests that it would be very resistant to vacuum arc. For this reason we have regarded TaC as a potentially useful emitter material. In this report we discuss our initial experience with emitters of carburized tantalum.

A tantalum emitter was etched using[15] a solution of 48% HF(2) + CH_3COOH(0.5) + conc H_3PO_4(1) + 36N H_2SO_4(1) at 5-10 volts d.c. The resulting emitter was judged adequate from its field emission pattern. Next the tip was carburized with benzonitrile at ~ 5 μ pressure for 60 seconds. Unfortunately the resulting surface did not exhibit any symmetry after carburization. The resulting carbide surface is probably very resistant to diffusion so that local surface excesses will not smooth out easily. Future work with this emitter will involve careful in situ carburization in order to carefully monitor and control the extent of carbon addition. The in situ technique will involve heating the tantalum emitter in the presence of low pressures of methane.

D. Rare Earth Boride Emitter Fabrication

The borides and carbides of certain transition and rare earth metals are believed to be more durable emitter materials than tungsten because of their high tensile strength and resistance to sputtering. Although preliminary studies of the FE characteristics of this class of emitter materials were carried out many years ago by Elinson et al.,[16] successful FE cathodes were not developed primarily because of material difficulties. More recently, a LaB_6 FE emitter has been reported to operate for more than 1000 hrs. at room temperature and at a current level of 1 to 2 mA.[17] Such a high current level is difficult to sustain even for tungsten in TF mode operation.

In recent work in this laboratory a simple and reliable method of fabricating high purity single crystal needles of LaB_6, SmB_6, and CeB_6 has been developed.[18] This has removed one of the major barriers impeding previous investigation of RB_6 (R = rare earth) emitters, i.e. the fabrication of pure and homogeneous single crystal material. The method employed, first performed by P. Lebeau and J. Eiguras,[19] later by Aito, et al.,[20] for LaB_6 is referred to as the "molten flux" method of single crystal growth. The method consists of mixing stoichiometrically the basic elements of the boride compound, e.g. powdered B and metallic rare earth metal, in an inert crucible and heating in an argon atmosphere to ~ 1500°C. After cooling, the solid Al solvent was dissolved with warm HCl leaving needle and plate-like single crystals of the boride compound.

In addition to the molten Al melt method, an arc zone melting technique of fabricating single crystals of LaB_6 described elsewhere has been employed successfully to fabricate single crystals.[21] The advantage of this technique is the ability to seed the growing crystal and thereby orient a particular crystallographic direction along the wire axis. The details of the fabrication procedures and results for LaB_6, CeB_6 and SmB_6 are given below.

1. Single Crystal Fabrication Procedures

The starting materials in our application of Al molten flux method consisted of 60 mesh boron powder, ingot formed aluminum, and metallic chips of the rare earth metal. Table 3 lists typical impurity levels for the starting materials used in the single crystal preparation.

TABLE 3

BULK PURITY SPECIFICATIONS OF THE VARIOUS MATERIALS MEASURED BY OPTICAL EMISSION SPECTROGRAPHIC TECHNIQUES

Material	Impurities (ppm)											
	Si	Mg	Fe	Cu	Al	Ca	Ni	O	C	Ag	Eu	Nd
Aluminum	3	<1	2	1	<1	<1	<1	-	<1	<1	-	-
Lanthanum	300	-	300	-	300	500	300	-	-	-	-	-
Boron	<20	<20	250	<20	<20	<20	<20	100	300	-	-	-
Samarium	<100	-	100	<100	<100	<100	-	-	-	-	500	300
LaB_6*	100	100	<10	<10	-	100	<10	-	-	100	-	-

*single crystals prepared

The single crystal growths were performed in 30 ml alumina boats placed in a resistively heated silicon carbide globar horizontal tube furnace. The boron was placed in four 4.8 mm diameter holes bored in the aluminum ingot and the rare earth was placed on the top center of the ingot. Before each run the growth chamber was evacuated and backfilled to one atmosphere pressure with high purity argon. The heating rate was from room temperature to 1500°C over a period of 6 hours and maintained at 1500°C for 8 hours. Cooling from 1500°C to 800°C took place at the conductive cooling rate of the furnace over a period of 1.5 hours; further cooling to room temperature occurred conductively over a 2 hour period.

After dissolving the Al solvent with HCl large single crystal platelets (approximately 2 mm square by 0.1 mm and some 1 × 7 × 0.1 mm) formed. Cubic shapes also 1 to 2 mm on a side were also observed. In addition, needle shapes 6 to 8 mm long and 0.1 to 0.2 mm square cross section were produced. A typical selection of these crystal shapes are shown in Fig. 13. Similar results were obtained with CeB_6.

Zone melted crystals were obtained by the arc melting technique described by Verhoeven, et al.[21] A regular e-beam zone melting apparatus was modified to accomplish this using a 1 mm diameter hot pressed (90% of theoretical density) rod of polycrystalline LaB_6. Various crystallographic orientations of ~ 1 mm diameter single crystal rod could be produced by use of seeding techniques.

2.1 Single Crystal Evaluation

Optical emission spectrographic analysis of the molten Al flux grown LaB_6 single crystals indicated, according to the Table summary, that crystal purity was superior to the starting materials. Subsequent Auger spectroscopy surface analysis of the crystals after flashing at ~ 1600 K showed only La and B. Apparently even the Al solvent is not appreciably incorporated into the surface of growing crystals of LaB_6, or if it is, it is removed subsequently by flash heating of the LaB_6 crystal.

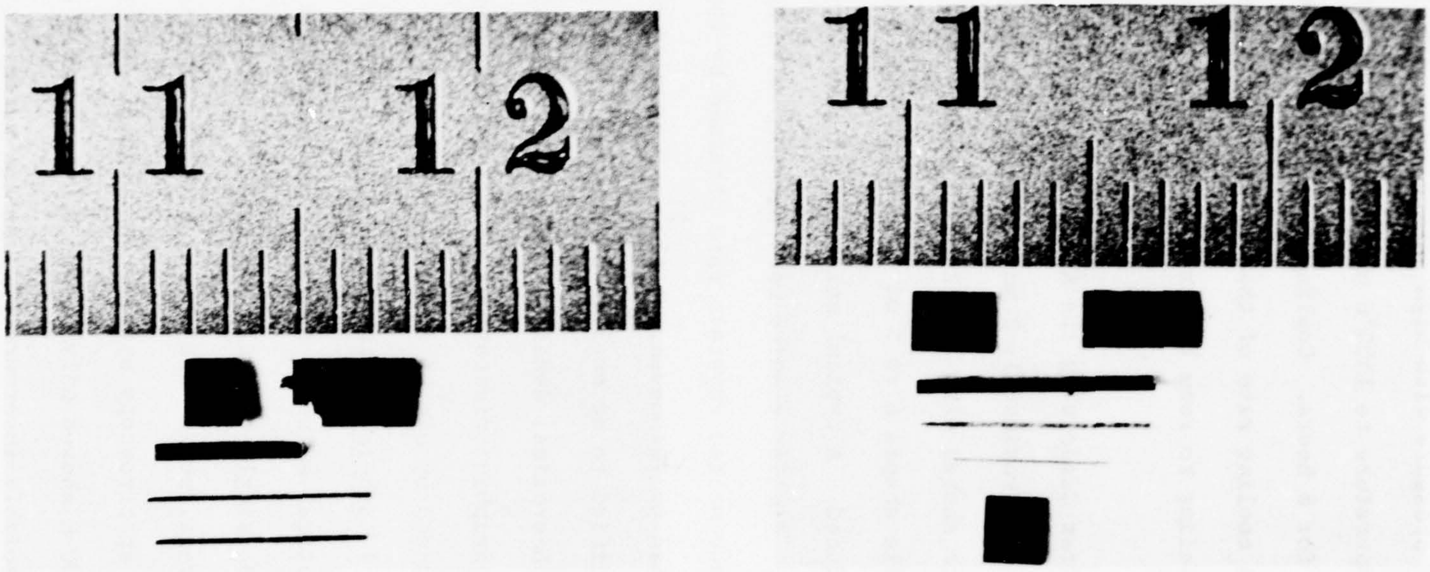

SmB_6 Size

LaB_6 Size

Figure 13. Typical shapes and sizes of the LaB_6 and SmB_6 single crystals produced by the liquid aluminum flux technique.

X-ray diffraction pictures of the platelet surface shown in Fig. 14 indicate a (100) direction perpendicular to the platelet face. X-ray diffraction of the longitudinal faces of the needle structures gave (100) and (110) faces. Thus the needle axis, which is the growth direction, is probably a (110) direction although subsequent field emitters fabricated from the needles showed both (110) and (100) orientations. The sharpness of the x-ray diffraction spots indicate relatively defect free single crystal specimens.

From powder x-ray diffraction patterns a lattice constant for the LaB_6 crystals of 4.156 Å was obtained; this is in excellent agreement with the literature value of 4.157 Å.[22] Similar x-ray examination of the prepared SmB_6 crystals gave a lattice constant of 4.132 Å also in good agreement with the literature value of 4.129 Å.[22]

The defect structure and possible impurity of lanthanum hexaboride has been studied by transmission electron microscopy on a Hitachi HU 11-B-3. Effective thinning processes, to prepare the LaB_6 specimens for examination in the microscope, have been developed. In the following, sample preparation will be discussed firstly, with examples of micrographs and diffraction patterns following.

2.2 Sample Preparation for Electron Microscopy

The specimens of LaB_6 under investigation were thin crystal platelets with the broad surfaces having an area of between 1- and 2 mm^2. A Fischione twin-jet electropolisher was used to thin the crystals. Two solutions have been tested in the unit: a 6 percent solution of perchloric acid in methanol, and a 2.25 percent solution of sodium hypochlorite in methanol. Because of the difficulties of handling the

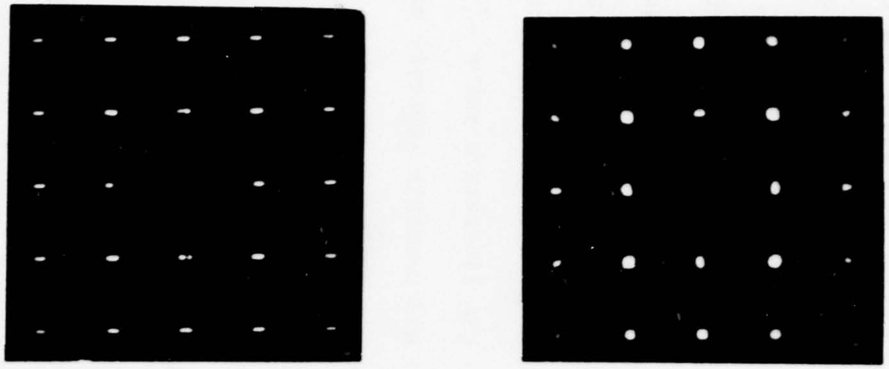
(a) (b)

Figure 14. X-ray diffraction patterns of (a) the longitudinal face of a LaB_6 needle shape crystal and (b) the face of a LaB_6 single crystal platelet.

perchloric acid solution in the electropolisher, more time has been spent working with the other solution.

Given a particular solution to use in the Fischione unit, there are two other parameters to control, namely temperature and applied voltage. In most cases, lowering the temperature improves the quality of the thinned region of the sample. This is true for LaB_6 and sodium hypochlorite. The lowest temperature obtained thus far was 8°C using an ice water bath.

As voltage was increased, three general types of sample erosion occur. At low voltages, the sample was etched, while at higher voltages the sample became pitted. Between these two extremes lie voltages where the sample was properly thinned, with fairly large areas thin enough for transmission electron microscopy.

A series of four voltages were applied to different crystals, in the range from one to ten volts d.c. These crystals were subsequently examined with a Siemans metallograph. The best specimens were found to be those electropolished at 6.5 volts. After thinning, the crystals were mounted on copper washers with silver paint.

2.3 Micrographs and Electron Diffraction Patterns

Only the samples prepared using low voltages have been examined in the Hitachi electron microscope. Very few suitable regions were available in these crystals. In the following examples, the technique of selected area diffraction was used. For each diffraction pattern, only the area shown in the corresponding micrograph contributed to the spots in it. These patterns are still under investigation, but there are a few features that can be pointed out.

In the first pair (Figures 15a and 15b), the diffraction pattern is made up of at least two superposed [100] patterns, and probably three. The micrograph, although of poor quality, does show the presence of a grain boundary on the left hand side. By changing the projector lens pole piece in the microscope, Figures 16a and 16b were obtained from a different area of the same specimen. Note the presence of streaks in this pattern, indicating the presence of a precipitate in the LaB_6 matrix. There also appears to be a different type of pattern (non - [100]) superposed on the LaB_6[100] pattern. Figures 17a and 17b, also from the same sample show a combination of the above two features.

Figures 18, 19, and 20 were taken from a different crystal. The diffraction pattern correlating to Figure 18 was not exposed properly and is unavailable, however this micrograph has some interesting features which merit its inclusion. Note the small rectangular area left cf center, from which emanated a number of dark bands. This may be a microcrystal embedded in the LaB_6 matrix causing a strain field to be set up in its vicinity. The dark blotchy areas on the right half and in the upper left corner may be bits of the silver paint.

Figures 19a and 19b are only approximately related due to a misalignment at the time of exposure. In this diffraction pattern and the next, there appears to be a different relationship between the LaB_6[100] pattern and the superposed pattern than in Figures 15a, 16a, and 17a. The other pattern in this figure is also a [100] pattern. In the micrograph there again appear to be strain fields at the lower right, and also a ring near the center.

Figure 15(a). Electron diffraction pattern of LaB_6 crystal prepared by molten aluminum flux technique.

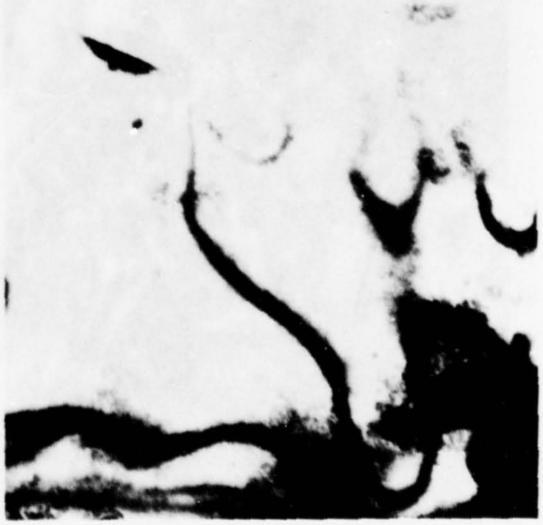

Figure 15(b). Transmission electron micrograph of LaB_6 crystal used in Figure 15(a). Magnification 48,000.

Figure 16(a). Electron diffraction pattern of LaB_6. Same specimen as in Figure 15, but different area.

Figure 16(b). Transmission electron microscope pattern of LaB_6 crystal used in Figure 16(a). Magnification 50,000.

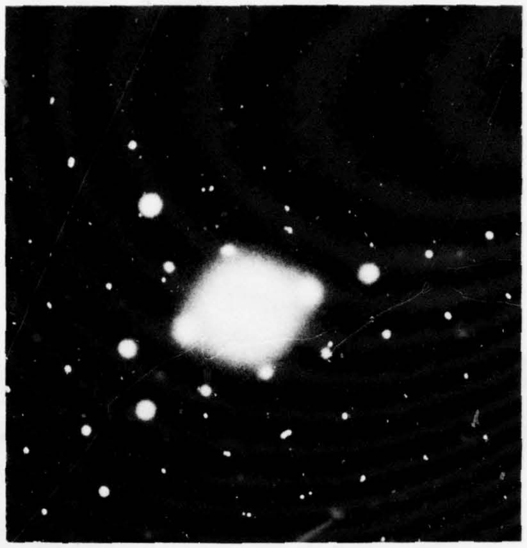

Figure 17(a). Electron diffraction pattern of LaB_6. Same specimen as in Figures 15 and 16 but different area.

Figure 17(b). Transmission electron microscope pattern of LaB_6 crystal used in Figure 17a. Magnification 48,000.

Figure 18. Transmission electron micrograph from a new crystal of LaB_6. Magnification 30,000.

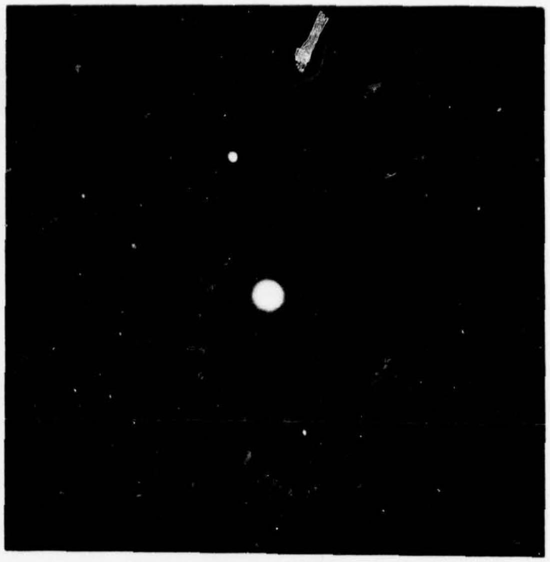

Figure 19(a). Electron diffraction pattern of the LaB_6 crystal of Figure 18.

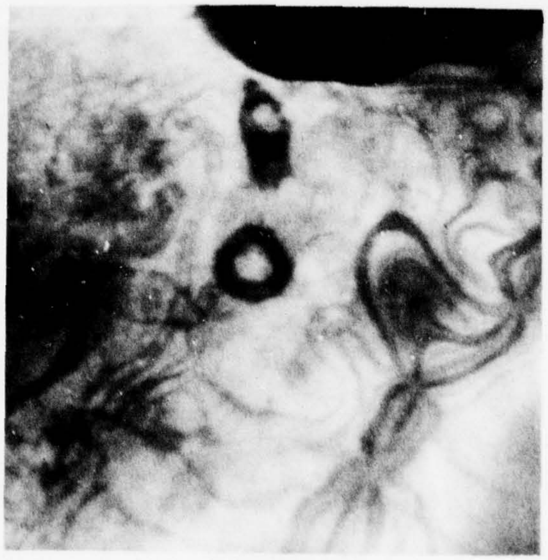

Figure 19(b). Transmission electron micrograph of the LaB_6 crystal used for Figure 19(a). Magnification 42,000.

Figure 20(a). Electron diffraction pattern of the LaB_6 crystal of Figures 18 and 19.

Figure 20(b). Transmission electron micrograph of the LaB_6 crystal used for Figure 20(a). Magnification 37,000.

Figure 20a shows the super-lattice as in 19a, and also a few spots indicate the presence of a grain boundary, although its presence is not clear in the micrograph.

These pictures, although preliminary, do show that some of the crystals are not single crystals, and that an inclusion or a precipitate, possibly aluminum, is present.

In summary, we conclude that the liquid metal flux technique of forming small single crystals of LaB_6, CeB_6 and SmB_6 is successful. It is our expectation that several other rare earth hexaboride compounds which exhibit congruently melting hexaborides, such as PrB_6 and NdB_6 will form single crystals by this technique.

3. Emitter Fabrication

Emitters were quickly and conveniently prepared by mounting a rectangular or cylindrical shaped single crystal blank on a flat rhenium ribbon (0.001" × 0.010") and fixed to it by means of a spot-welded rhenium strap of the same thickness and width (see Fig. 21). In addition, a binder consisting of an aqueous slurry of $MoSi_2$ was inserted between the emitter and rhenium support strap. Subsequent heating in vacuum at ~ 1800 K allowed the binder to sinter and form a durable mechanical and thermal bond between the emitter crystal and rhenium ribbon. The emitter points were obtained by electrochemical etching in a 50% methanol/NaOCl solution at 1.5 V. The power requirements to resistively heat the emitter shown in Fig. 14 to ~ 1800 K are less than 3 watts.

Highly magnified photomicrographs of a LaB_6 emitter are shown in Fig. 22 for three rotational orientations of the emitter. The gross diameter of the emitter end form is about 1000 Å; however, close

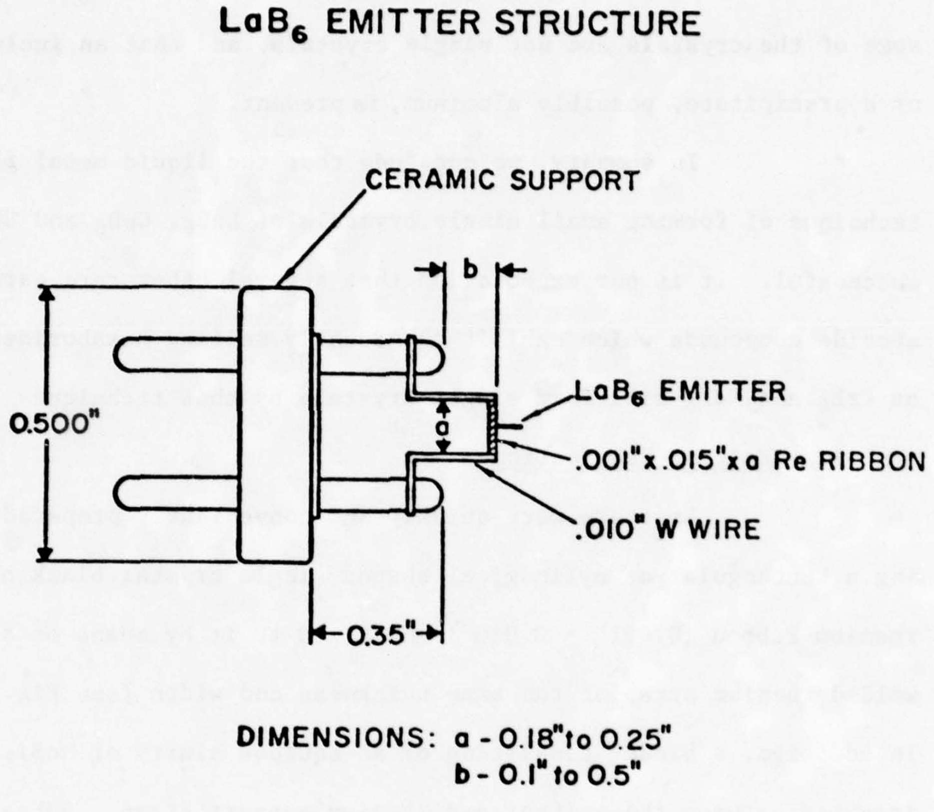

Figure 21. Diagram of emitter and resistively heatable filament support structure used for single crystal material of LaB_6.

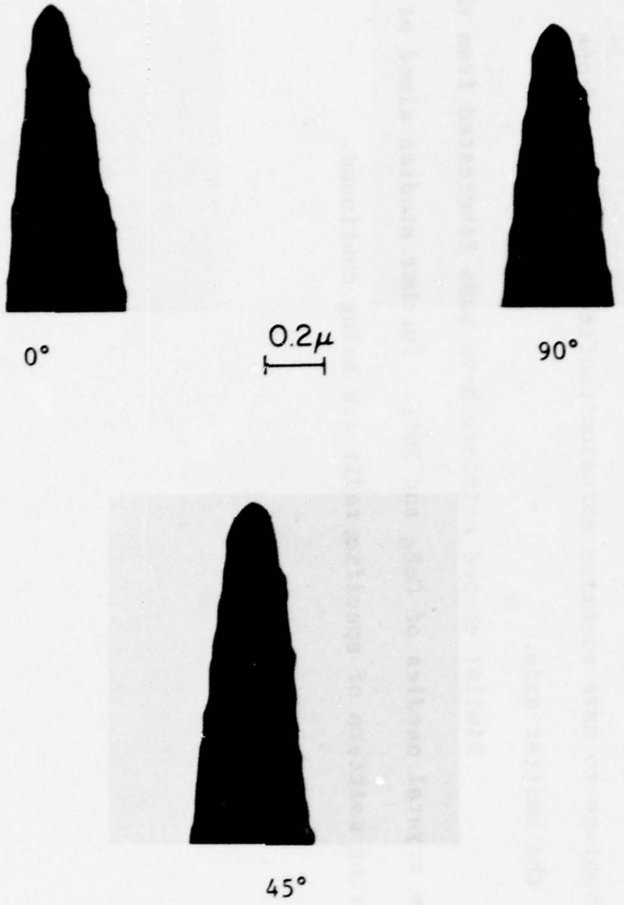

Figure 22. Micrograph profiles of an LaB_6 field emitter which has been operated in a TF mode.

inspection of the photomicrographs reveals that the emitter has a built-up end form with a diameter at the apex of only 100 Å. The built-up feature is due to the application of the d.c. field while heating in vacuum. Field induced migration of the substrate occurs which causes preferential development of certain planes. This effect is a well known phenomenon[23] and has been used to advantage in the development of practical field emission cathodes[12,13] for which it is an advantage to have electron emission confined to a narrow cone about the emitter axis.

Similar shaped emitters have been fabricated from the single crystal needles of CeB_6 and SmB_6. Further studies aimed at preparing emitters of specific radii are being continued.

SECTION IV

ELECTRON EMISSION STUDIES

A. Rare Earth Hexaboride Emitters

Preliminary studies of the field emission characteristics of LaB_6 single crystals have been carried out. Difficulties have been encountered in obtaining reproducible and coherent patterns. In many cases emission seemed to be occurring from randomly spaced emission points on the emitter surface.

Fig. 23 shows the pulsed emission pattern from an LaB_6 emitter after several temperature cycles above 1800 K. These patterns were obtained from the same emitter as shown in Fig. 22. The overlapping circles of emission can only be explained in terms of small (atomic sized) protrusions on the emitter surface which preferentially emit due to local field enhancement. The overlapping circles of emission were observed to change position with temperature cycling.

The aforementioned results were usually observed with low voltage ($V < 1000$ volts) emitters. It was speculated that the erratic behavior of the previous emitters were due to stoichiometry variations at the emitter surface due either to a bulk stoichiometry differing from $\frac{La}{B} = \frac{1}{6}$ or to a preferential evaporation of lanthanum or boron. To avoid this possibility subsequent emitter blanks were maintained at high temperatures for several hours prior to forming the tip.

Fig. 24 is a sequence of d.c. FEM patterns obtained from a higher voltage LaB_6 emitter. Photos (a) and (b) were taken during the thermal cleaning sequence. From Auger spectroscopy studies it was determined that heating the LaB_6 crystals to 1700 K resulted in a clean

(a) (b)

Figure 23. Pulsed field electron patterns obtained from the Figure 15 emitter. Photo (a) was obtained after initial thermal cleaning; photo (b) was obtained after prolonged thermal cycling and operating in the TF mode.

(a) V = 1800 V (d.c.)   (b) V = 4900 V (d.c.)

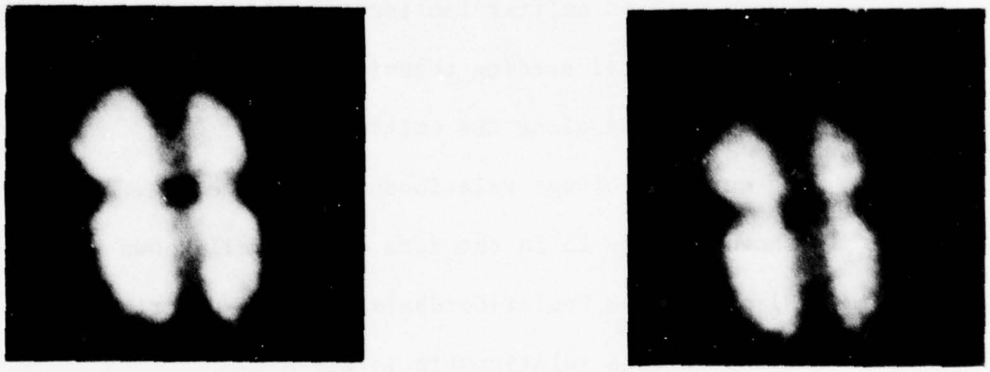

(c) V = 8 kV (Pulse)   (d) V = 8 kV (Pulse)

Figure 24. Field electron microscope patterns of an LaB$_6$ emitter; (a) and (b) were during the early stages of thermal cleaning and taken with a d.c. applied voltage; patterns (c) and (d) were taken during the latter stages of thermal cleaning using a pulse viewing voltage. The (110) plane is the central plane.

surface. An interesting observation in the Fig. 24 photos is the reversal in emission distribution between (b) and (c). Photos (c) and (d), which are believed to be clean surfaces, show a definite two-fold symmetry characteristic of a (110) orientation along the emitter axis. It is also clear from the latter photos that the (110) plane (in the center of the pattern) is a high work function. From the pattern symmetry it can be concluded that the (100) planes, located on the top and bottom of photo (c), and the (111) planes, located on the right and left side of the (110) plane, are also high work function planes.

As an electron optical source it is desirable to have the lowest low work function plane along the emitter axis. It appears the lowest work function region occurs in the center of the triangle formed by the (110), (111) and (100) directions.

Future work on emitter fabrication will be aimed at developing zone refining and crystal seeding techniques in order to obtain specified crystal directions along the emitter axis.

The current-voltage relationship from the Fig. 22 LaB_6 FE emitter is shown in Fig. 25 in the form of the well known Fowler-Nordheim (FN) plot. The Fowler-Nordheim equation describing the field electron current-voltage relationship is given by

$$J = \frac{1.54 \times 10^{-6} F^2}{t(y) \quad \phi} \exp\,(-6.83 \times 10^7 \phi^{3/2} v(y)/F)(A/cm^2) \qquad (20)$$

if F is in V/cm and ϕ in eV. The correction terms t(y) and v(y), which are due to the image potential, are tabulated[24] slowly varying functions of the auxiliary variable $y = (e^3F)^{1/2}/\phi$. If a value of $\phi = 2.4$ eV is assumed, a value of $\beta = 1.5 \times 10^4$ cm^{-1} was obtained from the linear portion of the Fig. 25 plot. The apparent deviation of the I(V) data from

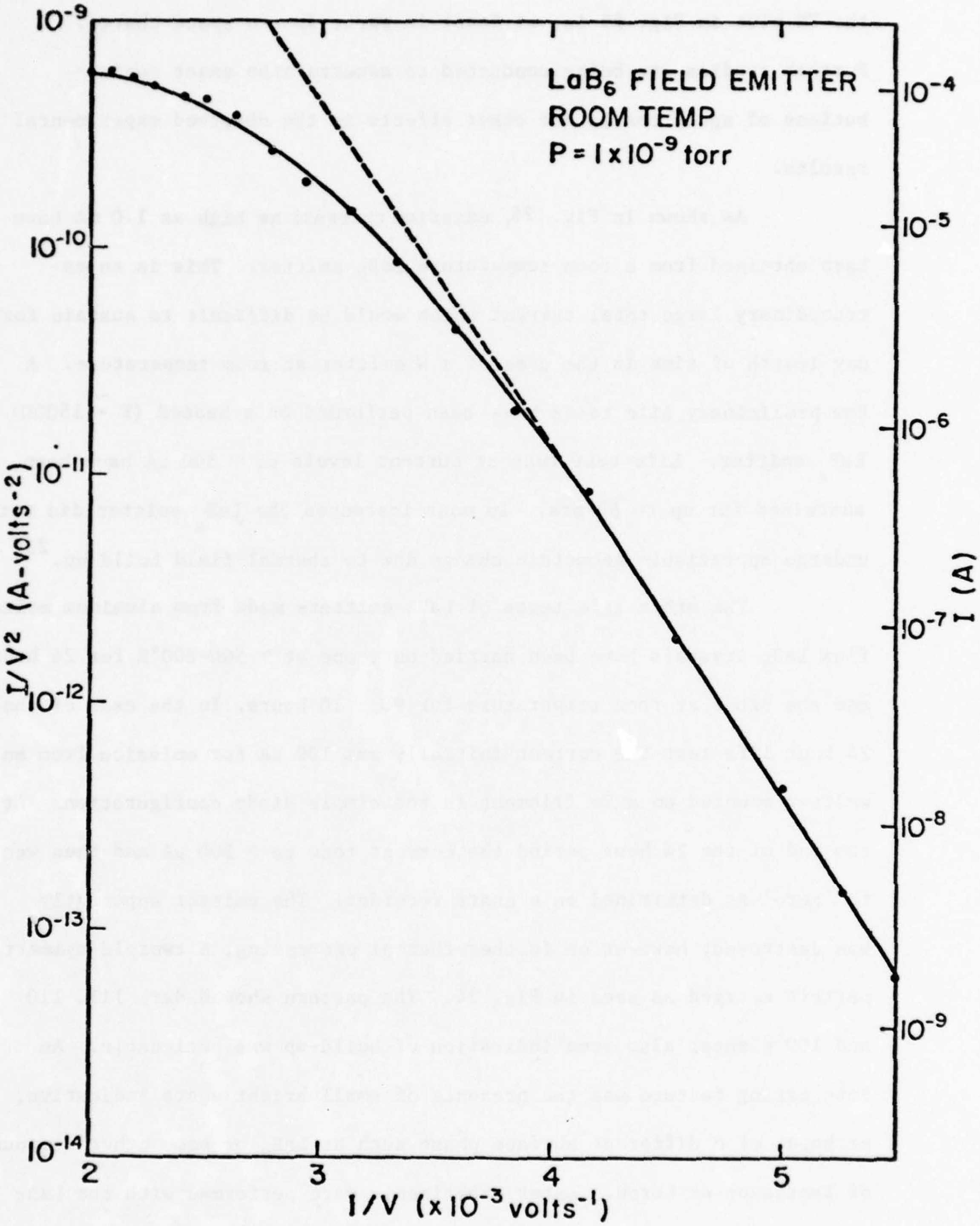

Figure 25. A room temperature FN plot of the I(V) data taken for a LaB_6 emitter.

the FN plot in Fig. 25 is, at least in part, due to space charge. Further studies are being conducted to ascertainthe exact contributions of space charge and other effects in the observed experimental results.

As shown in Fig. 26, emission currents as high as 1.0 mA have been obtained from a room temperature LaB_6 emitter. This is an extraordinary large total current which would be difficult to sustain for any length of time in the case of a W emitter at room temperature. A few preliminary life tests have been performed on a heated ($T \cong 1500K$) LaB_6 emitter. Life test runs at current levels of ~ 300 μA have been sustained for up to 60 hrs. In most instances the LaB_6 emitter did not undergo appreciable geometric change due to thermal-field build up.[23]

The other life tests of LaB_6 emitters made from aluminum molten flux LaB_6 crystals have been carried out, one at ~ 500-800°K for 24 hours and the other at room temperature for 90 ± 10 hours. In the case of the 24 hour life test the current initially was 100 μA for emission from an emitter mounted on a Re filament in the simple diode configuration. At the end of the 24 hour period the current rose to > 200 μA and then went to 'zero' as determined on a chart recorder. The emitter apparently was destroyed; however on further thermal processing, a twofold symmetric pattern emerged as seen in Fig. 24. The pattern showed dark 111, 110 and 100 planes; also some indication of build-up was noticeable. An interesting feature was the presence of small bright spots indicative, perhaps, of a different surface phase such as LaB_4 or some other compound of lanthanum or boron. Later experiments were performed with the LaB_6 emitter operating in the TF mode at ~ 1500°K; waves of low work function material were observed spreading over the emitter. At this point, the emitter failed.

In the case of the room temperature life test, the probe current was also monitored during the run which lasted 90 ± 10 hours before emitter failure; the uncertainty in life arises because the emitter failed at an undetermined time during a weekend run. The probe current through a 0.08 millisteradians aperture was 400 nA in a background pressure of 5×10^{-9} torr; total current was approximately 60 μA. Probe and total emission current Fowler Nordheim plots are shown in Figs. 26 and 27. Note that the total emission current reached a maximum of 0.6 mA at 900 volts, a remarkably high value for room temperature operation.

A marked curvature is apparent in the upper end of the Fowler Nordheim plot both for probe and total current. Undoubtedly this is due to space charge effects at the emitter which become significant at the high emitter current densities occurring at the upper end of the Fowler Nordheim plots. Assuming that the average field over the emitter apex is given by $F = V/5r$ and that only 70% of the hemispherical emitter end contributes to the emission then the current density is $J \sim 6 \times 10^6$ A/cm^2 at an emission current of 0.6 mA. Close inspection of the total current Fowler Nordheim curve indicates the possibility of a break in the plot at ~ 300 V. Whether this is a coincidence or a real effect remains to be elucidated.

Some preliminary experiments with zone melted LaB_6 have been performed. The single crystal was mounted in a holder with provisions for both indirect (hot filament nearby) and direct heating by electron

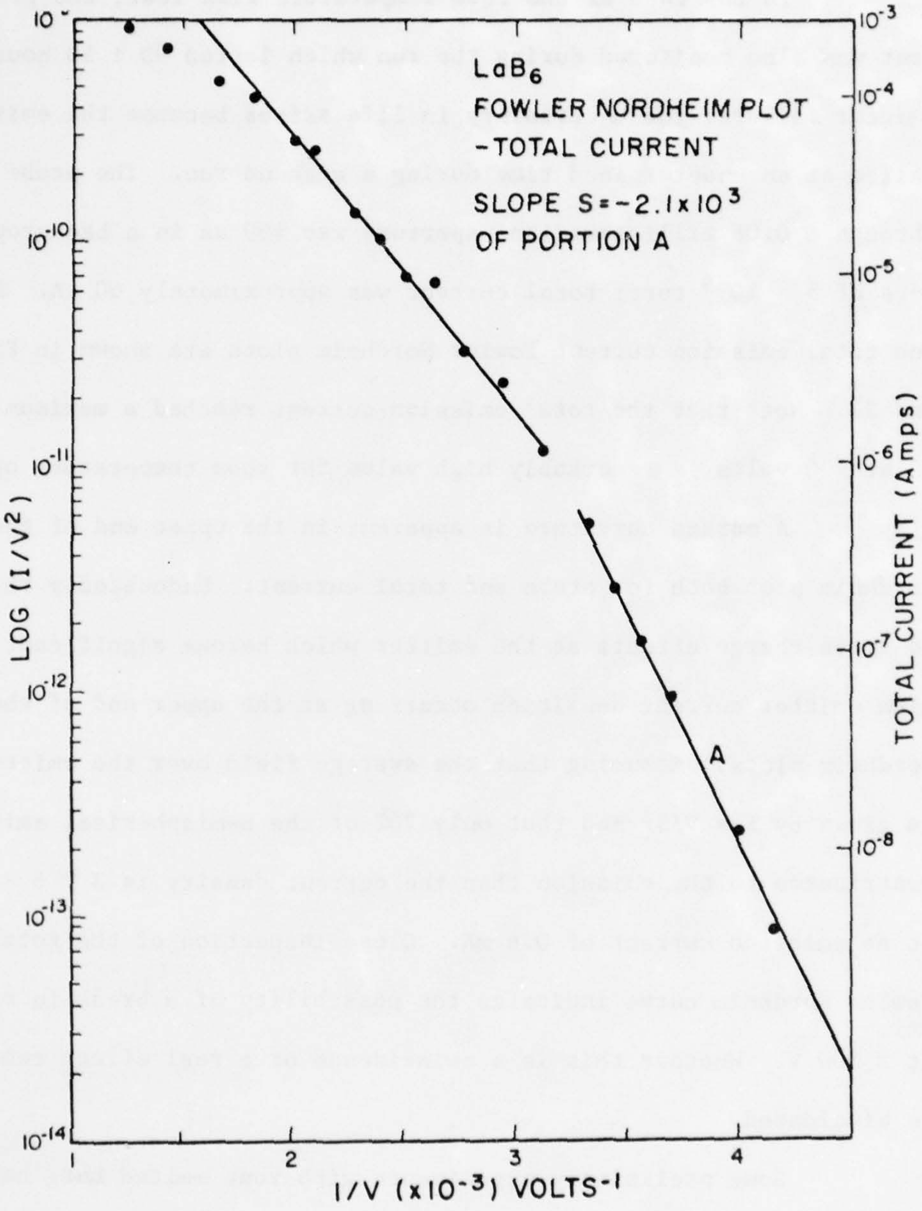

Figure 26. Fowler Nordheim plot for the total current from a LaB_6 emitter.

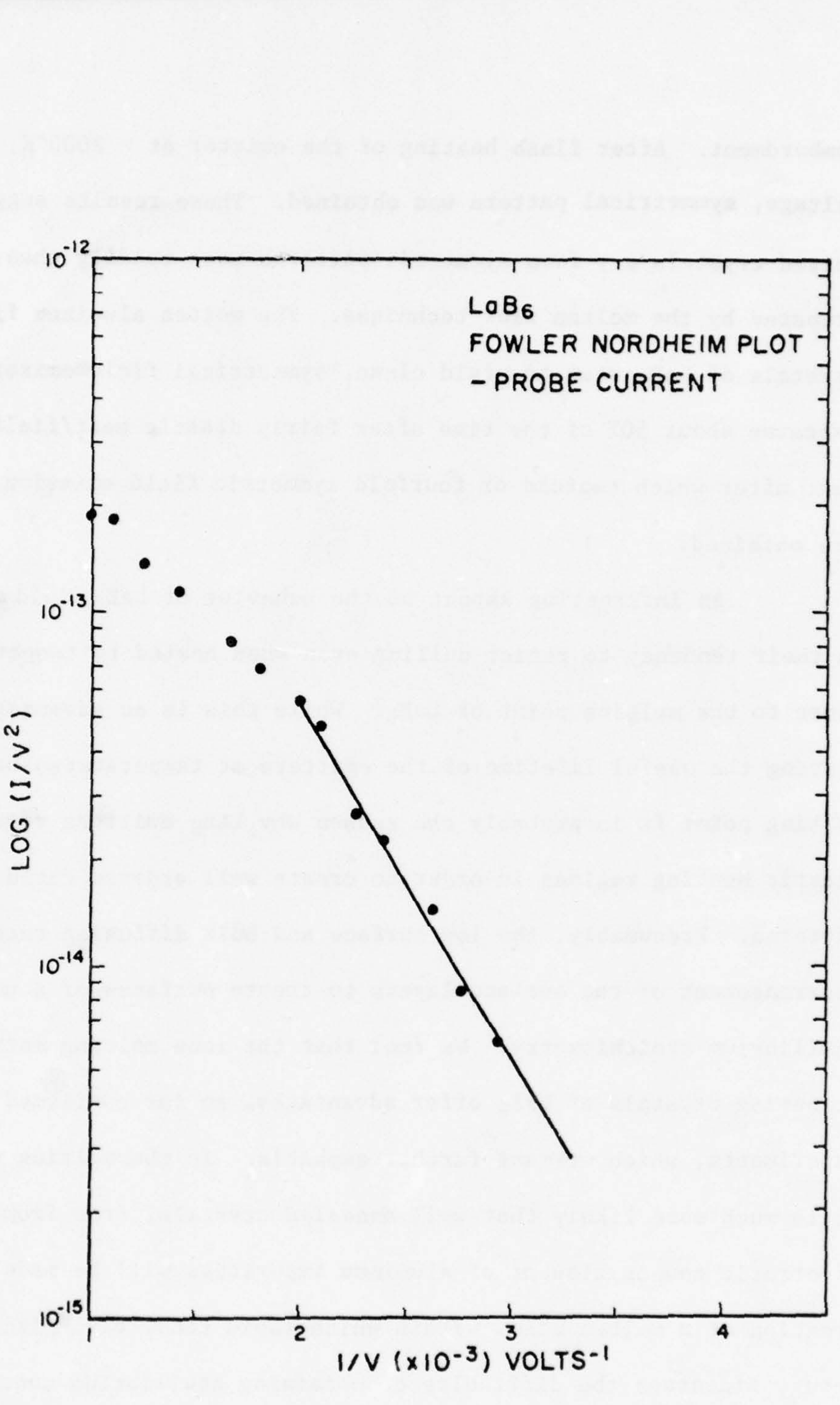

Figure 27. Fowler Nordheim plot of probe current from a LaB_6 emitter through a .08 msr aperture.

bombardment. After flash heating of the emitter at > 2000°K, a low voltage, symmetrical pattern was obtained. These results suggest that melted crystals may form symmetric patterns more readily than those prepared by the molten flux technique. The molten aluminum flux crystals of LaB_6 seem to yield clean, symmetrical field emission patterms about 50% of the time after fairly drastic heat/field treatment after which twofold or fourfold symmetric field emission patterns are obtained.

An interesting aspect of the behavior of LaB_6 field emitters is their tendency to resist dulling even when heated to temperatures close to the melting point of LaB_6. While this is an advantage in preserving the useful lifetime of the emitters at temperatures below the melting point it is probably the reason why LaB_6 emitters require drastic heating regimes in order to create well ordered field emission patterns. Presumably, the low surface and bulk diffusion rates retard rearrangement of the surface layers to create surfaces of a uniform equilibrium stoichiometry. We feel that the zone melting method of preparing crystals of LaB_6 offer advantages, so far confirmed by two experiments, which warrant further emphasis. In the melting process, it is much more likely that well annealed crystals, free from regions of erratic composition or of aluminum impurities will be made. The creation of a molten zone, within which rapid convective mixing can occur, sidesteps the difficulty of obtaining equilibrium concentrations of lanthanum and boron in the molten flux prepared LaB_6 crystals.

We also examined two samarium hexaboride emitters, the first of which yielded a well ordered pattern with fourfold symmetry. This emitter was very sensitive to bombardment by gas emanating from the screen as a result of electron impact desorption. Failure of the emitter occurred soon after the beginning of experiments while the emitter was being operated in the TF mode. Another SmB_6 emitter behaved in a similar manner with an initially unstructured pattern giving way finally to a fourfold symmetric pattern after being subjected to heating in the presence of a high field emission field. The final emitter voltage for viewing field emission patterns was ~ 6 kV. Although field desorption at elevated temperatures was attempted in an effort to clean the emitter, no ordered pattern emerged even though the tip was dulled somewhat by the field desorption process.

The very high currents attainable with LaB_6 emitters at room temperature is sufficient motivation to continue this work with LaB_6.

B. Tantalum

The field emission properties of clean tantalum have been studied as a prelude to a study of the emission properties of tantalum carbide; tantalum is of interest on its own as a potential field electron emission material because of its refractory properties and because of the fact that it is adjacent in the periodic table to the much studied tungsten.

The field build-up[25] properties of tantalum are a source of interest because both tungsten and molybdenum - close neighbors of tantalum in the periodic table- exhibit interesting build-up phenomenon. In particular the build-up[12] of (100) oriented tungsten emitters provides a very important practical high brightness TF electron source.

A preliminary investigation of the build up behavior of a (111) oriented Ta emitter showed that a clean emitter provided a field built up end form with strong emission from the central (111) plane. Carbon contamination or a partial presence of O_2 of $P \cong 1 \times 10^{-8}$ torr caused the (100) planes to become strongly emitting during field build up in the temperature range 1300-1600 K. Since TF emission from a (111) built-up Ta(111) emitter appears to be a promising emitter prospect, further investigation of its emission characteristics will be carried out.

C. Iridium

Build-up studies were also performed on a slightly contaminated (100) oriented iridium emitter. The ratio of built-up radius to thermally annealed radius was found to be 0.543 as determined by the slopes of the Fowler Nordheim plots. The buildup seems to occur on the (110) plane and seems to be accompanied by the development of (100) and (111) facets. Photographs of the thermally annealed and built-up field emission patterns are shown in Fig. 28. The ring around the (100) plane is due to slight contamination of the emitter. An examination of the kinetics of the build up phenomenon was carried out by measuring growth of the field emission current as a function of temperature at a constant voltage. An Arrhenius plot of the build-up is shown in Fig. 29. Also shown in Fig. 30 for comparison is an earlier unpublished study of the field build-up kinetics for tungsten.

It is worthwhile to note that the field increases during build-up since the radius of the built-up emitter is approximately 50% less than at the beginning. Linear Arrhenius plots of the build up time vs 1/T

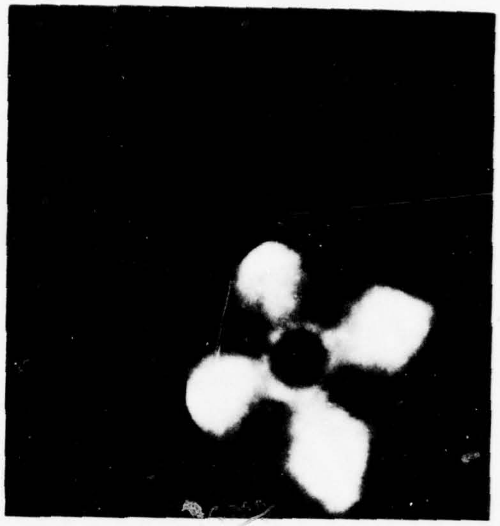

Figure 28(a)

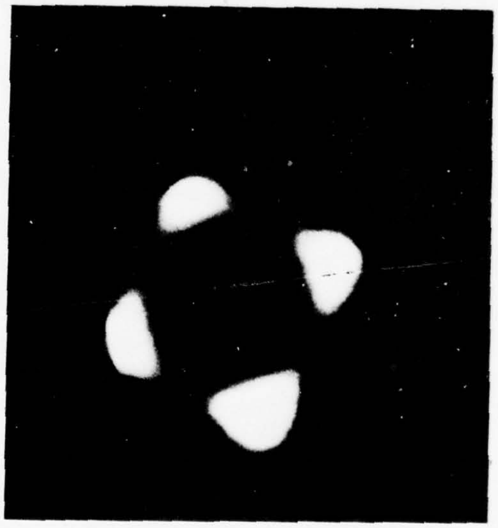

Figure 28(b)

Field emission patterns of a thermally annealed (Figure a) **and built-up** (Figure b) iridium field emitter.

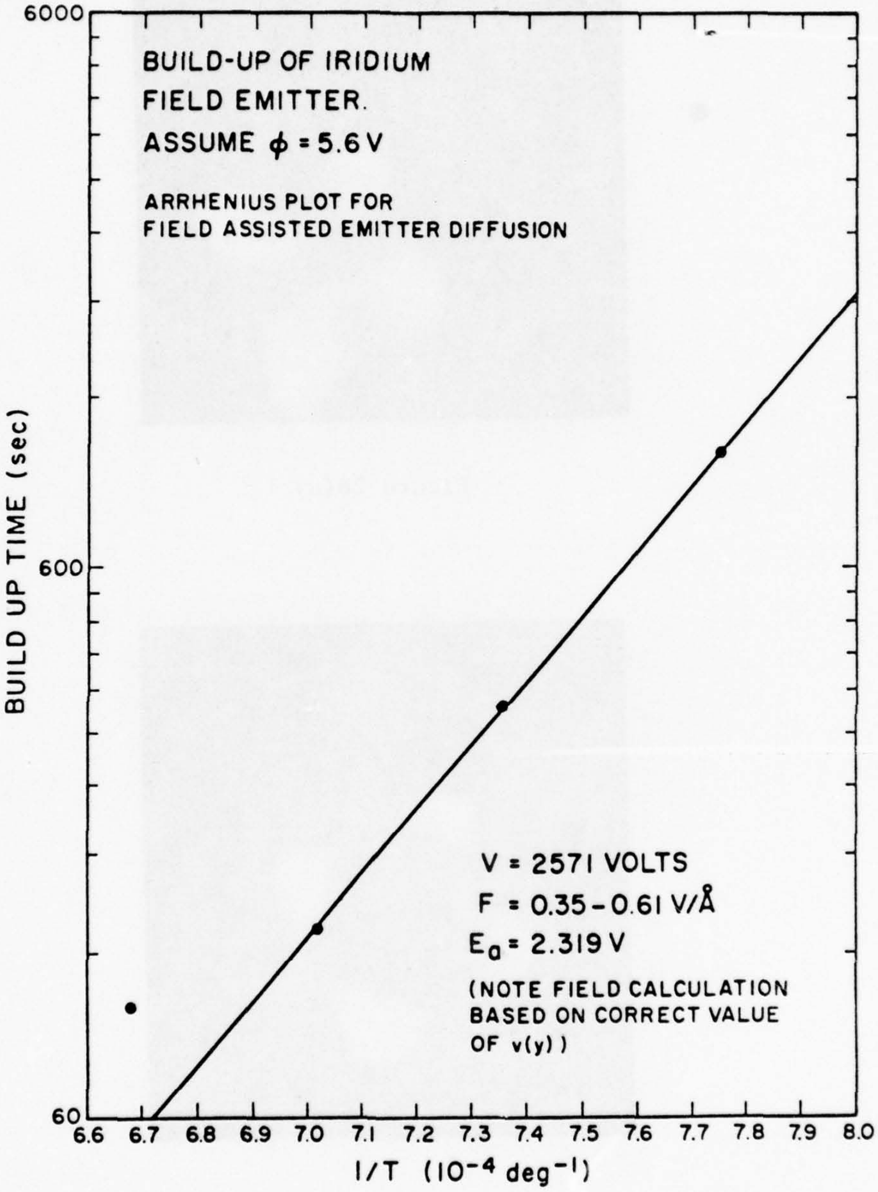

Figure 29. Arrhenius plot for field assisted surface diffusion of iridium.

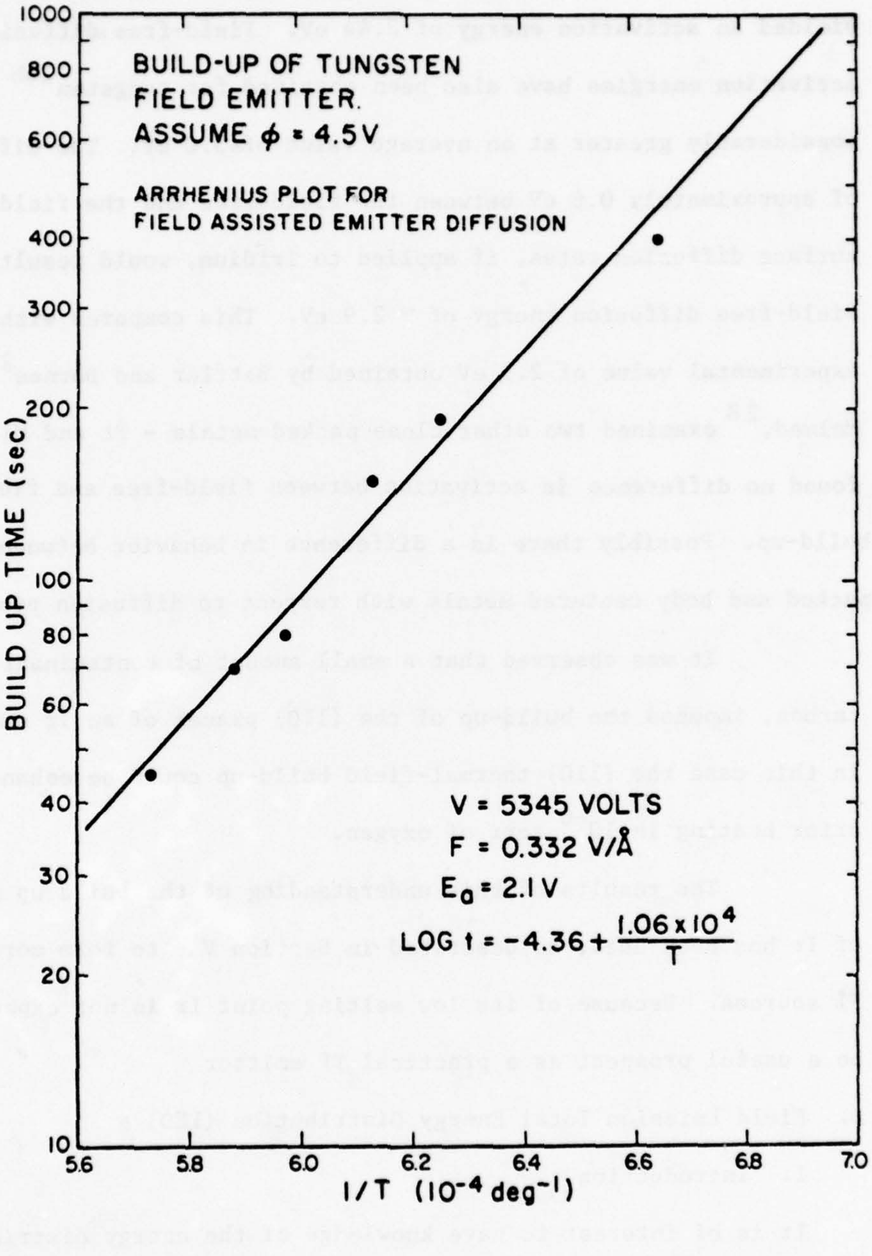

Figure 30. Arrhenius plot for field assisted surface diffusion of tungsten.

for iridium gave an activation energy of 2.3 eV. An earlier investigation of the field build-up of tungsten by Bettler and Charbonnier[26a] yielded an activation energy of 2.44 eV. Field-free diffusion activation energies have also been obtained for tungsten[26b] and are considerably greater at an average value of 3.0 eV. The difference of approximately 0.6 eV between the field-free and the field assisted surface diffusion rates, if applied to iridium, would result in a field-free diffusion energy of ~ 2.9 eV. This compares with an experimental value of 2.3 eV obtained by Bettler and Barnes[27]. Melmed,[28] examined two other close packed metals - Pt and Ni and found no difference in activation between field-free and field assisted build-up. Possibly there is a difference in behavior between the close packed and body centered metals with respect to diffusion properties.

It was observed that a small amount of contaminant, possibly carbon, impeded the build-up of the (110) planes of an Ir emitter. In this case the (110) thermal-field build-up could be enhanced by prior heating in 10^{-6} torr of oxygen.

The results of this understanding of the build up process of Ir has been used, as described in Section V, to form more effective FI sources. Because of its low melting point Ir is not expected to be a useful prospect as a practical TF emitter

D. Field Emission Total Energy Distribution (TED)

1. Introduction

It is of interest to have knowledge of the energy distribution of field emitted electrons because of the limiting effect this has on focussed spot size. For example, in a cylindrically symmetric lens spherical and chromatic aberrations produce an image consisting of circles of radius r'_s and r'_c slightly ahead of the gaussian image plane, where

$$r'_s = 1/4 \; MC_s\alpha^3 \qquad (21)$$

$$r_c = 1/2 \; MC_c \; (\Delta E/E)\alpha \qquad (22)$$

and M is magnification of the lens, C_s is the spherical aberration coefficient referred to the object space, C_c is the chromatic aberration coefficient and α is the angle of the ray leaving the object which passes through the aperature; ΔE is the energy spread of the electron beam of energy E. Combining r'_s and r'_c in quadrature we have, the spot radius r:

$$r = (M\alpha/2)\left[C_c^{\,2}(\Delta E/E)^2 + C_s^{\,2}\;\alpha^4/4\right].^{1/2} \qquad (23)$$

Clearly we need to know $\Delta E/E$ if we wish to estimate spot size; ΔE may be obtained by determining the full half width maximum (FHWM) of the TED and in this section we report measured and calculated values of ΔE for emitters at temperatures in the range 77-2000°K for two promising TF emitters.

The TED for field emitted electrons, in the free electron approximation, is given by [29]

$$j(\epsilon) = \left[(4\pi me)/h^3\right] f(\epsilon) \int_0^{\epsilon + E_F} D(W)\cdot dW \qquad (24)$$

where m and e are the mass and charge respectively of an electron in the metal, h is Plank's constant; ϵ is the total electron energy, measured relative to the Fermi level which is above the bottom of the metal conduction band by an amount E_F. $f(\epsilon)$ is the Fermi function $f(\epsilon) = \left[1 + \exp(\epsilon/kT)\right]^{-1}$ where k is the Boltzmann constant and T is absolute temperature; W is the total energy associated with electron perpendicular to the surface:

$$W = [p(x)^2/2m] + V(x) \qquad (25)$$

where p(x) is the electron momentum normal to the surface, and V(x) is the effective electron potential energy. The function D(W) is the probability that an electron incident on the barrier will emerge from the metal and is obtained by solution of the Schrödinger equation:

$$\frac{d^2\psi}{dx^2} + \frac{2m}{\hbar^2}[W - V(x)]\psi = 0 \qquad (26)$$

From the WKB approximation D(W) is obtained:

$$D(W) = [1 + \exp(A(W))]^{-1} \qquad (27)$$

where A(W) is given by:

$$A(W) = (4/3)(2m/\hbar^2)^{1/2} \cdot (E_F + \phi - W)^{3/2} \cdot v(y)/(eF)$$

$$= 0.6829 \cdot (E_F + \phi - W)^{3/2} \cdot v(y)/F \qquad (28)$$

where F is given in V/Å and E_F, ϕ, W are measured in volts; y is given by

$$y = (e^3F)^{1/2}/(E_F + \phi - W)$$

$$= 3.79\, F^{1/2}/(E_F + \phi - W) \qquad (29)$$

Murphy and Good[30] have derived expressions for v(y):

$$v(y) = (y/2)^{1/2}\,\{2E(k1) - (y + 1)K(k1)\} \quad y > 1 \qquad (30)$$

$$v(y) = (1 + y)^{1/2}\,\{E(k2) - yK(k2)\} \quad y < 1 \qquad (31)$$

and $k1 = (y - 1/2y)^{1/2}$; $k2 = \{(1 - y)/(1 + y)\}^{1/2}$

E and K are the standard elliptic functions:

$$E(k) = \int_{o}^{\pi/2} (1 - k^2 \sin^2\theta)\cdot d\theta; \; K(k) = \int_{o}^{\pi/2} (1 - k^2 \sin^2\theta)^{-1/2}\cdot d\theta \qquad (32)$$

In the work presented here, the integral in Eq. 24, was intergrated numerically using the well known Simpson's rule which involves evaluation at equally spaced intervals h of the function to be integrated:

$$I = \int_{a}^{b} f(x) \simeq S(N) = f(a) + 4 \sum_{m=1}^{2^{N-2}} f[a + (2m - 1)h]$$

$$+ 2 \sum_{m=1}^{2^{N-2}-1} f[a + 2mh] + f(b) \qquad (33)$$

where h is given by

$$h = (b - a)/2^N$$

The summation is usually repeated at increasing values of the integer N beginning at N = 1 until two successive values of S(N) differ less than a specified amount - in this case by part in 10^6. A more economical method of obtaining accurate estimates of I may be obtained by using the Romberg extrapolation, a technique which greatly limits the necessary number of subdivisions of h required. Thus an improvement S(N,J) in the estimate of I may be obtained by using the extrapolation formula:

$$S(N,J) = \frac{4^{j-1} S(N + 1, J - 1) - S(N,J - 1)}{4^{j-1} - 1} \qquad (34)$$

which creates an array of improved estimates of I which converge to the correct value of I as N and J increase.

2. Calculated Values of Full Width Half Maxima

In order to evaluate the FWHM, it was first necessary to locate the peak in the TED function, Eq. (24) and then to search out for the abscissa values corresponding to the half maximum ordinates. This was performed as a function of field for two work functions - $\phi = 2.5$ eV, $\phi = 4.5$ eV and for a range of temperatures 78°K - 2000°K; the results are shown in Figs. 31(a) and (b).

A remarkable feature of all these curves is the sharp maximum in the curve which occurs at fields in the range 0.1 - 0.4 V/Å. The 4.5 eV work function curves show the most pronounced maxima which increase with temperature, reaching a maximum of $\sim$ 2 eV at a temperature of 1500°K and a field of 0.25 V/Å. At higher fields than that corresponding to the maximum, the FWHM declines from $\sim$ 2 eV at $F \simeq 0.25$ V/Å to a value of $\sim$ 0.7 eV at fields in the range 0.5 - 0.7 V/A. At higher fields the FWHM slowly increases. The minimum occurring beyond the maxima show a steady increase with temperature from $\sim$ 0.27 eV at 600°K to $\sim$ 0.75 eV at 1800°K, hence the minima is approximately proportional to T. The field shift of the maxima and minima with temperature is also of interest; both maxima and minima decrease to lower fields as temperature decreases, also the maximum rapidly diminishes as temperature declines below 300°K; at this temperature, the position of the maximum has shifted to less than 0.1 V/Å. Clearly for temperatures below 300°K, the maxima

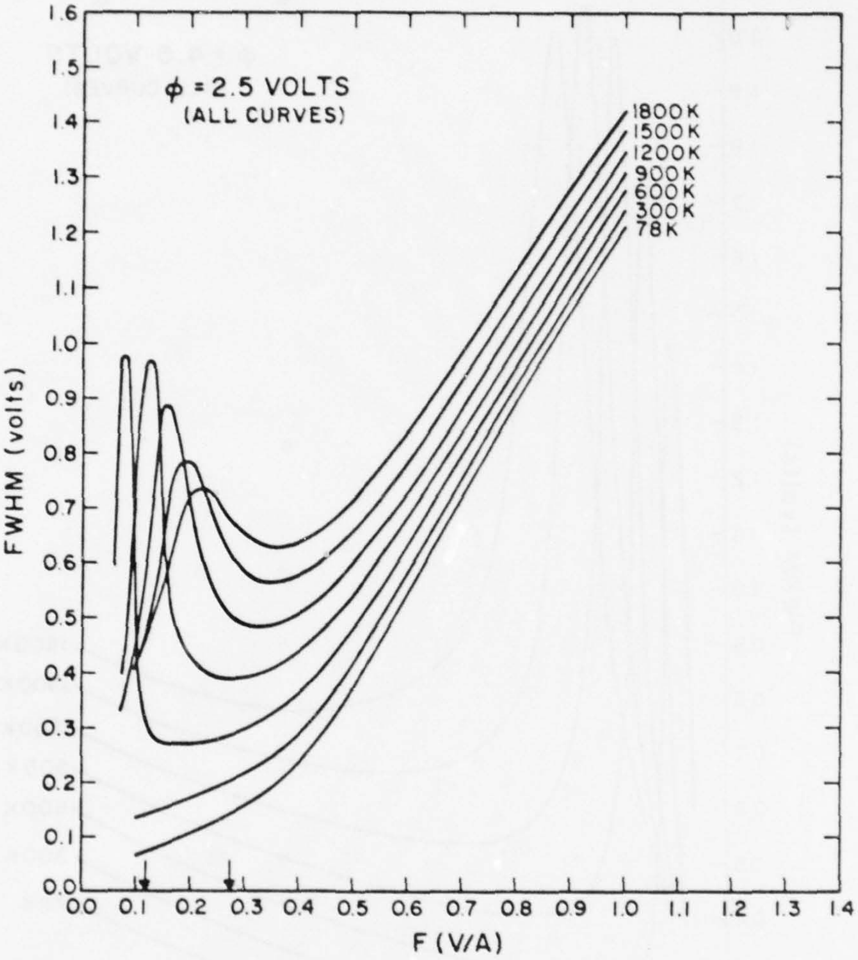

Figure 31(a). Plot of the full-width at half maximum (FWHM) for the energy distribution of field emitted electrons as a function of electric field F at various temperatures; $\phi = 2.5$ V.

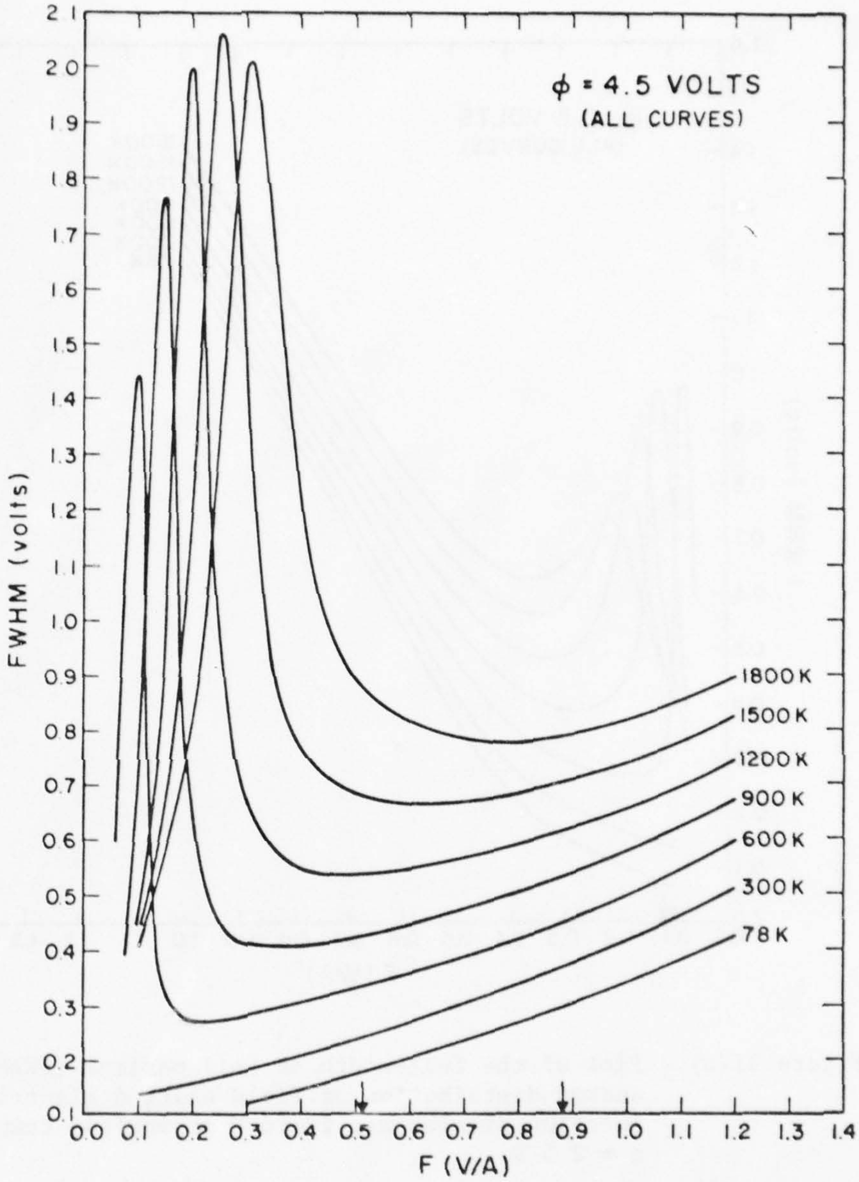

Figure 31(b). Plot of FWHM for the energy distribution of field emitted electrons as a function of electric field F at various temperatures; ϕ = 4.5 V.

will lie at fields corresponding to experimentally inaccessible current densities.

The 2.5 eV work function curves show markedly lower FWHM values except at fields above 0.5 V/Å where they increase rapidly with field and at low fields (< 0.1 V/Å) where they appear to converge with the high work function values. For example, the 1800°K maximum for the $\phi = 2.5$ eV curve is only ~ 0.7 eV compared to more than 2.0 eV for the 4.5 eV work function curve.

The reason for the existence of the peak in the FWHM curve is that at low fields the electron emission is dominated by the thermionic component which is emitted over the work barrier, while at high fields the emission contains a large amount of electrons tunnelling close to where the electron density is highest i.e., just above the Fermi level. At intermediate fields, the contribution from both the thermionic emission and field emission is presumably comparable with a correspondingly greater energy spread since a portion of the electron emission is coming from just above the Fermi level and another similar portion is coming from the top of the work function barrier.

3. Experimental Values of FWHM

Experimental values of the FWHM have been obtained at several temperatures for two kinds of emitter: a (100)W built up emitter having a work function of 4.5 eV and a zirconiated (100)W Zr/W(100) emitter having a 2.6 eV work function. Both of these emitters are now developed to the extent that they are suitable as a practical source for microprobe systems.

Early FWHM results obtained from a Van Oostrom energy analyzer were considerably greater than the calculated values at high fields/currents. It was hypothesized that the discrepancy was caused by space charge effects occurring in the Van Oostrom analyzer where the electron beam is prefocussed at a "crossover" point prior to being collected. However, FWHM results from a spherical retarding potential analyzer, which does not use a crossover, were also anomalously broad, thus eliminating analyzer artifacts as a source for the unexpected broadening. These results, from a built-up (100)W emitter, are shown in Fig. 32 along with the theoretical values which appear as nearly horizontal lines. Clearly the experimental values agree fairly well with the theoretical values at fields below ~ 0.73 V/Å but greatly exceed them at higher fields. For the Zr/W(100) data, Fig. 33 , the experimental and theoretical curves converge at lower fields, while at higher fields the experimental curves show considerable anomalous broadening as in the case of the (100)W data. For example, at the highest fields studied, the experimental FWHM values are approximately 3 volts, compared with theoretical values of 0.7 - 0.8 volts.

For practical TF cathodes, a more important question is how the FWHM values vary with probe current and whether at a given probe current FWHM values can be lowered by changing the operating temperature of the emitter. Fig . 34 contains a plot of FWHM versus the current per unit solid angle subtended by the probe hole at the emitter for (100)W built-up and Zr/W(100). A remarkable feature of the plot is that all of the different temperature data fit on one curve and the

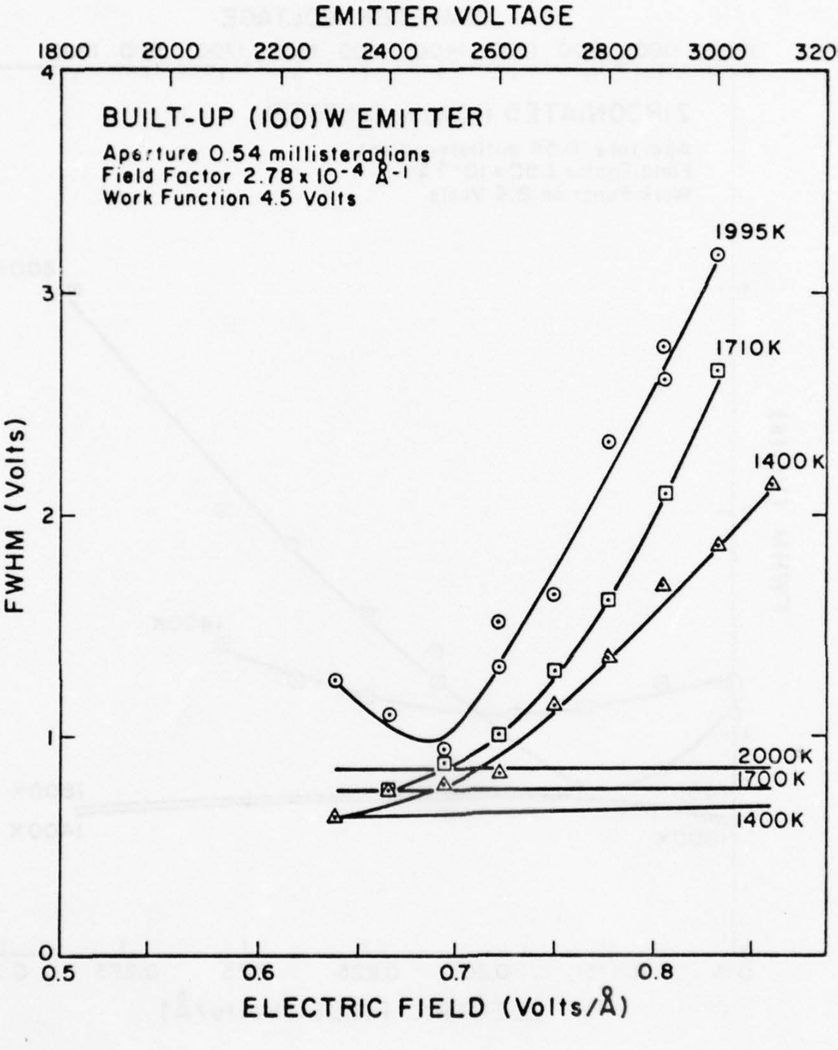

Figure 32. Plot of experimental (data points) and theoretical (lower curves) values of FWHM vs electric field for the built-up W(100) emitter.

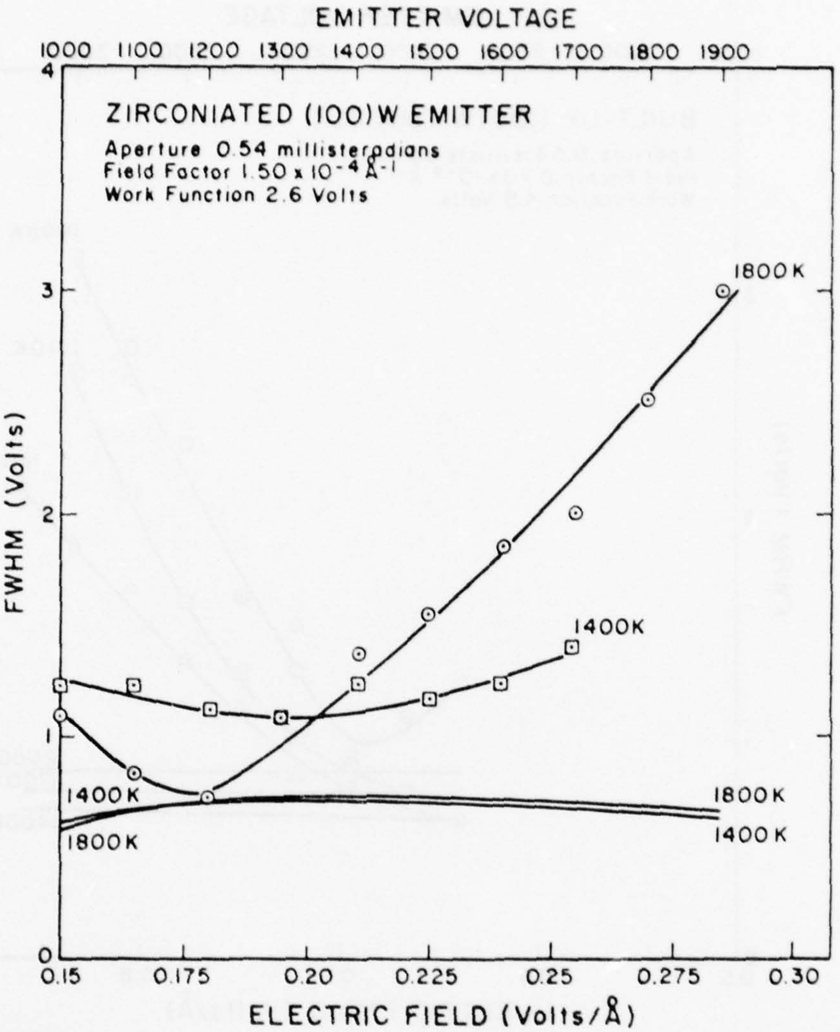

Figure 33. Plot of experimental (data points) and theoretical (lower curves) values of FWHM vs electric field for the zirconium W(100) emitter.

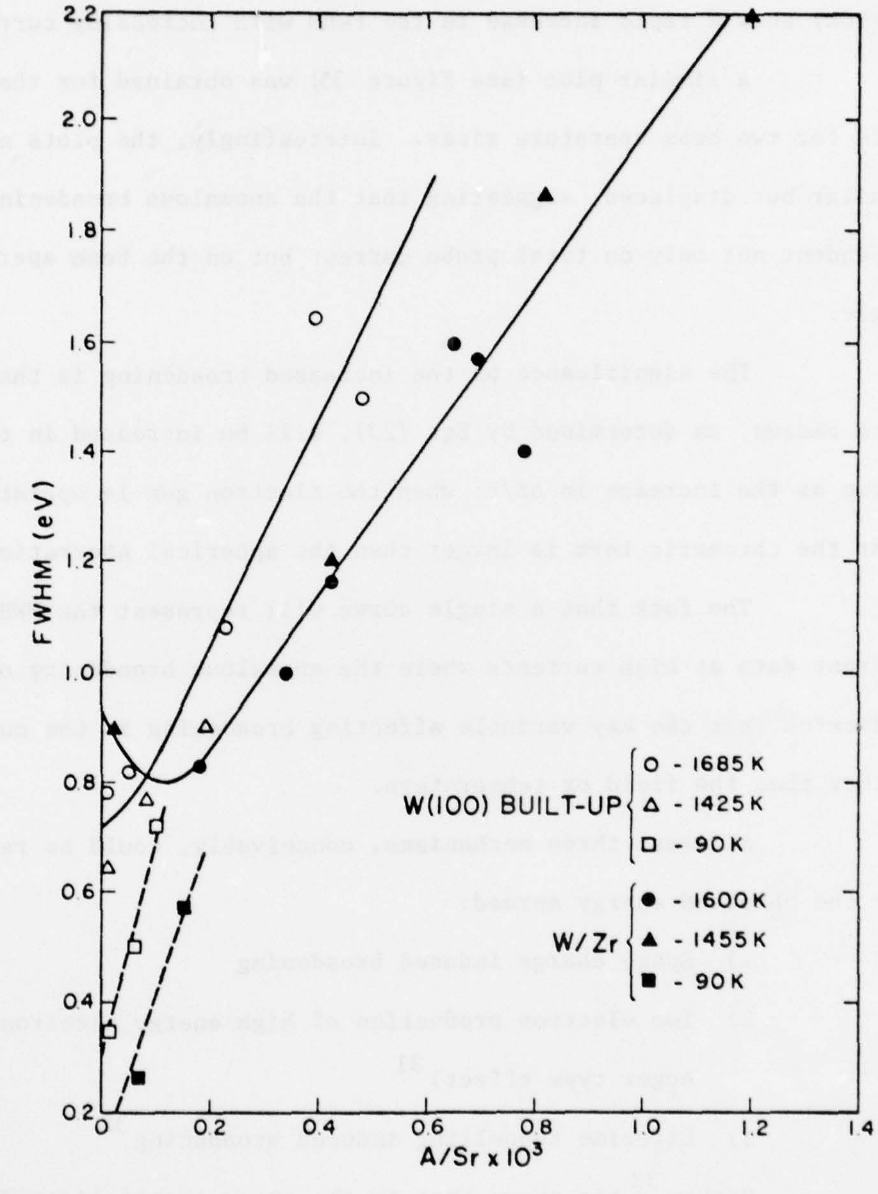

Figure 34. Full width half maximum values of the total energy distribution versus angular intensity from a W(100) built-up and W/Zr emitters operating in the TF mode. Aperture half angle is 6.5 mrad. Emitter apex radii are ~ 2000 Å (before build up).

plot is very nearly a straight line. Even the low temperature (T=90K) show a rapid increase in the FWHM with increasing current.

A similar plot (see Figure 35) was obtained for the Zr/W(100) data for two beam aperature sizes. Interestingly, the plots are very similar but displaced, suggesting that the anomalous broadening is dependent not only on total probe current but on the beam aperture angle.

The significance of the increased broadening is that spot size radius, as determined by Eq. (23), will be increased in the same ratio as the increase in $\Delta E/E$, when the electron gun is operated so that the chromatic term is larger than the spherical aberration term.

The fact that a single curve will represent the FWHM versus current data at high currents where the anomalous broadening occurs, indicates that the key variable affecting broadening is the current rather than the field or temperature.

At least three mechanisms, conceivably, could be responsible for the observed energy spread:

1) Space charge induced broadening
2) Two electron production of high energy electrons (an Auger type effect)[31]
3) Lifetime tunnelling induced broadening[32]

Hasker[33] has shown that in the space-charge-limited beam current regime, changes can occur in the position of the peaks of thermionic total energy distributions and that the peak shift is accompanied by an increase in FWHM. Both effects are caused by velocity

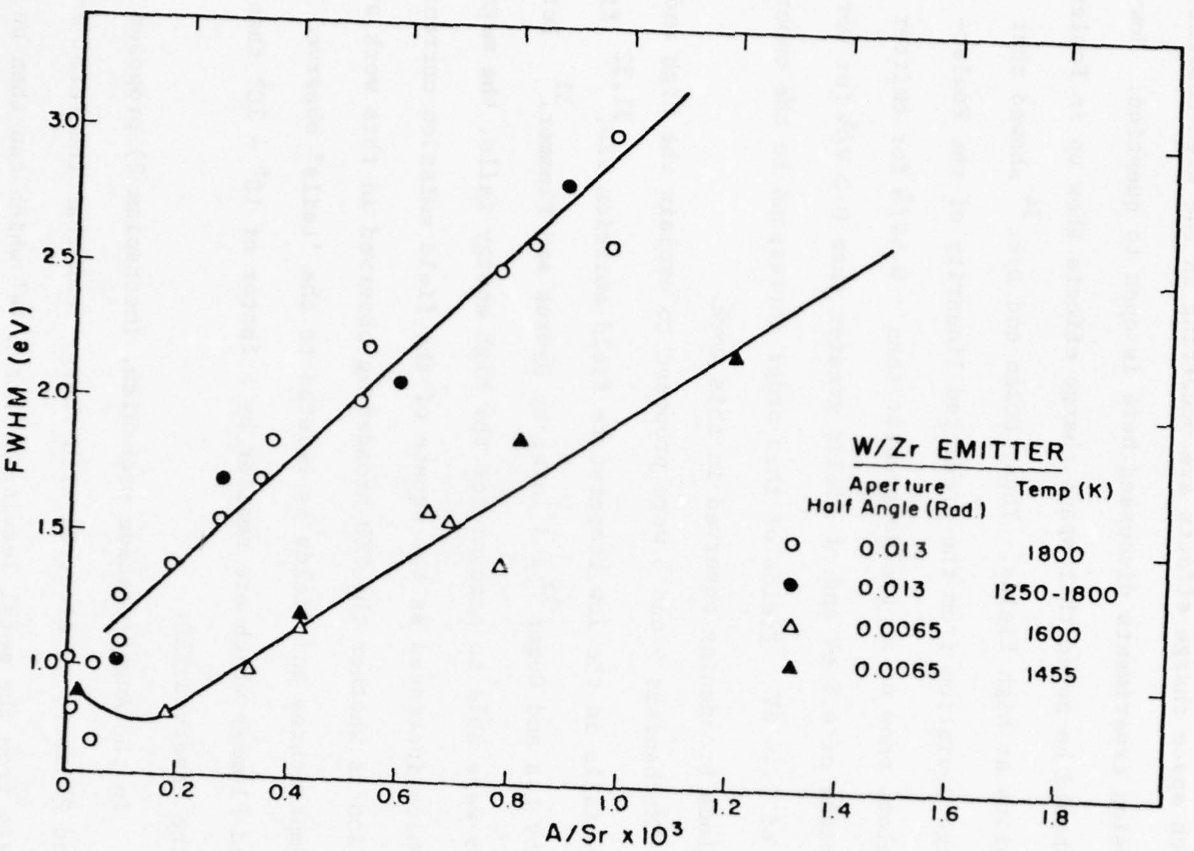

Figure 35. Full width half maximum (FWHM) values of the total energy distribution versus angular intensity from a W/Zr field emitter operating in the TF mode. Emitter apex radius ~ 2000 Å.

selection in the space charge potential field in front of the cathode. Whether such space charge effects are occurring in the high-current field emission experiments discussed here is open to question. However, it should be noted that space charge effects show up in Fowler-Nordheim plots at high fields. Thus, Dolan and Dyke[34] showed that space-charge deviation from the predicted linearity of the Fowler-Nordheim plots show up at fields greater than ~ 0.6 V/Å for emitter work functions of 4.5 eV and at fields greater than 0.2 V/Å for work functions of 2.44 eV. Fields of this order correspond to the onset of the anomalous broadening observed in this work.

Mechanisms 2 and 3 were proposed to explain the high and low energy tails in the low temperature field emission TED,[31,32] first observed by Lea and Gomer[35] and later by Gadzuk and Plummer.[31] Both mechanisms were able to account for the high energy tails, the magnitude of which increased as the square of the field emission current. The question is whether the TED broadening observed in this work at higher temperatures and fields is related to the 'tails' observed by Gadzuk and Plummer which are smaller by a factor of 10^5 - 10^6 than the peak of the observed TED.

In the Auger/cascade mechanism, (mechanism 2) proposed by Gadzuk and Plummer, an electron with energy less than the Fermi energy, E_F, tunnels from the metal leaving a 'hot hole' which can then be scattered by the electron gas, producing a secondary hole and an electron. This scattered electron can then tunnel out of the metal with considerably enhanced tunnelling probability and be observed in the high-energy tail. The contribution to the high energy portion of the TED provided by the scattered electrons is given by:

$$j_c' = a \frac{J_o^{\,2}}{d^3} \frac{E_F\left(E_F + \epsilon\right)}{\epsilon^2} \left\{ \frac{d^2}{\epsilon^2} + \frac{14}{9}\frac{d}{\epsilon} - \exp^{\,\epsilon/d} \left[E_4\left(\frac{\epsilon}{d}\right) + \frac{5}{9} E_3\left(\frac{\epsilon}{d}\right) \right] \right\} \qquad (35)$$

where $d \simeq F/(1.03\ \phi^{1/2})$, $a = 3h^3/(10\pi me)$, and J_o is the total field emission current density; ϵ is the energy above the Fermi level and E_3, E_4 are the n^{th} order exponential integrals given by:

$$E_n(z) = \int_1^{\infty} \frac{e^{-zt}}{t^n} \,.\, dt; \; n = 0, 1, 2, \ldots..$$

$$\text{and } E_{n+1} = 1/n \left(e^{-Z} - Z\, E_n\right)$$

Clearly the magnitude of j_c will increase very rapidly with F, since this appears in J_o exponentially. According to the experimental data of Gadzuk and Plummer, obtained at fields of ~ 0.33 V/Å from a (100) oriented W emitter of work function 4.5 eV, the high energy tail is 10^{-5} - 10^{-6} as large as the Fermi peak at 1 eV above the Fermi level. By casting Eq. (35) in the form $j\ /(J_o/d)$ which expresses the amplitude of the high energy tail as a fraction of the TED Fermi peak, it is calculated that the fraction increases by 4.3×10^4 as the field is increased from 0.33 V/A to 1.0 V/Å so that the high energy tail is now 0.12 times as large as the TED Fermi peak. This increase is not quite large enough to account for the broadening actually observed; however the model (model 3 above) of Gadzuk and Lucas[31] in which broadening of the energy of the tunnelling electrons is due to the finite time for electron tunnelling, predicts that the ratio of high energy tail to Fermi peak is ~ 7×10^5 greater at 1 V/Å than at 0.33 V/Å. This is sufficient to make the high energy tail comparable with the Fermi peak in the TED so that this mechanism could account for the observed broadening.

SECTION V

GAS PHASE FIELD ION STUDIES

A. Introduction

It has long been known that it is possible to resolve the atomic lattices of crystals with a field ion (FI) microscope.[15] One implication of this fact is that the virtual source size of a FI emitter, as shown in Fig. 5, must be of the order of a few Angstroms and therefore the emitter will be an extremely bright source of ions. For the aperture angles one is limited to by the electrostatic lenses used in microprobes, the virtual source size $\rho \approx 10$Å.

To make use of this potential high brightness it would be necessary to image the source onto a target with a resolution $\approx \rho$. This is extremely difficult given the inherent qualities of the electrostatic lenses one must use with ion beams. However, it turns out that even when the resolution is ~ 10^3 Å the FI source provides more beam current than other ion sources which may produce much more total current (see Table).

In the following summary of our FI source work we describe the properties of the source and the results of its application in an ion microprobe.

B. FI Gun Development

Experiments were performed with a glass FI gun designed so the field emitter and source gas could be cooled with LN_2 to 77K. The ion beam impinged on a phosphor screen where the current could be measured as well as the light intensity. The field emitter was operated at potentials usually between 10 kV and 20 kV and was surrounded by a Mo cathode cap with a 0.5 mm aperture through which the beam exited and through which the source was differentially pumped (see Fig. 40).

Iridium (Ir) field emitters were used with radii ~ 1000 Å. Ir was chosen because of its resistance to field induced chemical etch by residual gases, especially water. Work done earlier in this laboratory has shown the superiority of Ir to tungsten (W) in this regard (see Figs. 36 and 37).

C. Ion Microprobe Design

An ion microprobe was built on top of a commercial pumping station. The optical system consists of two electrostatic lenses, aperture, stigmator and beam deflectors.

The lenses are arranged as a doublet as shown in Fig. 38. The objective collimates the beam forming an image at $Z \simeq \infty$ of diameter $d = 2\, r_1$,

$$r_1 = M\left(\rho^2 + \left(1/4\ C_{s_1}\alpha^3\right)^2 + \left(1/2\ C_{c_1}\frac{\Delta V}{V}\alpha\right)^2\right)^{1/2}. \tag{37}$$

M is the magnification, C_{s_1} and C_{c_2} the spherical and chromatic aberration coefficients, respectively of the first lens. ρ is the virtual source size, α the angular divergence determined by the aperture, V the accelerating voltage and ΔV the energy spread of the beam in eV. The projector lens focusses the collimated beam on

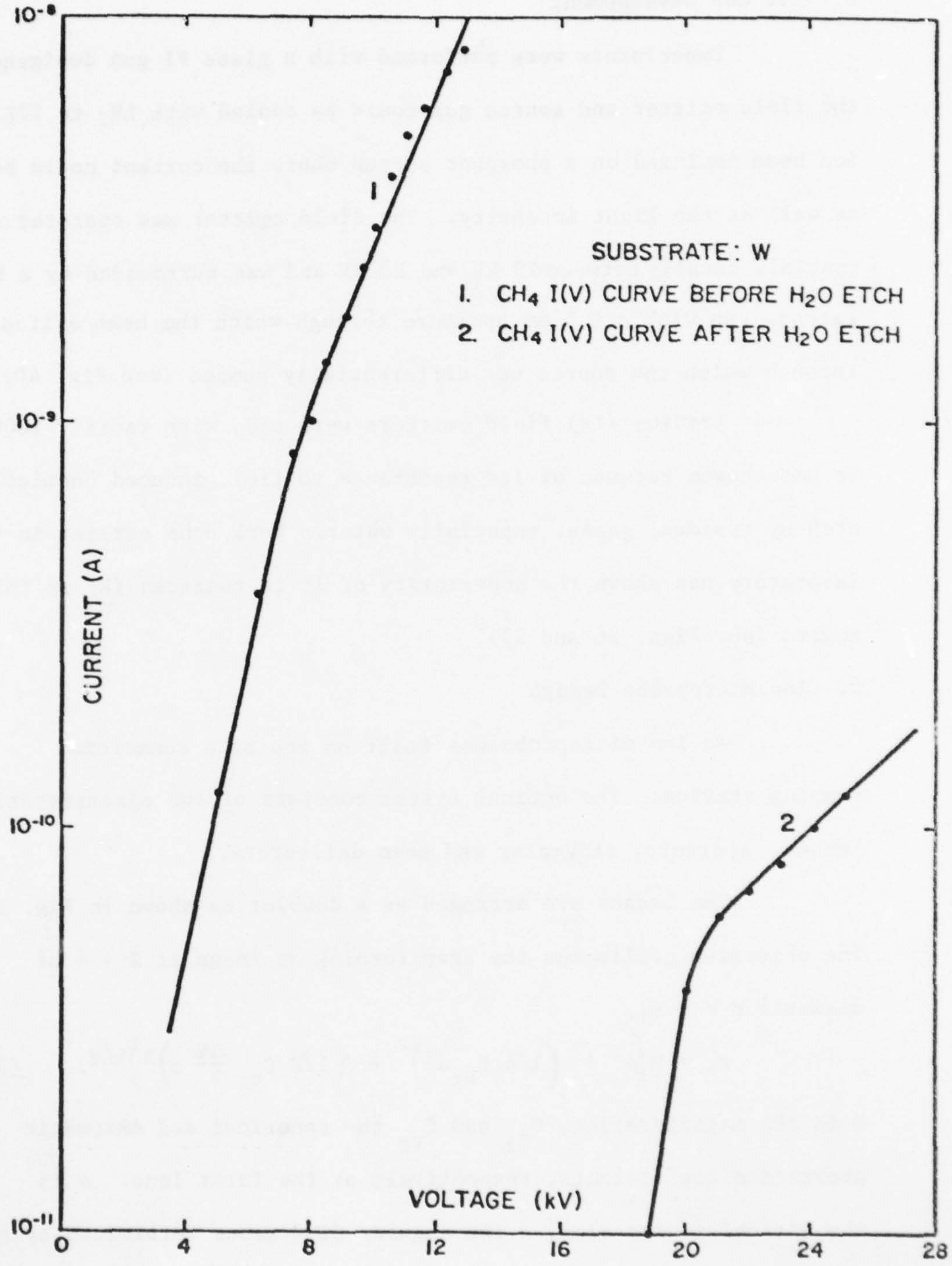

Figure 36. FI current vs voltage from a W emitter before and after 0.3-h exposure to H_2O at a pressure $P_{H_2O} = 10^{-4}$ torr.

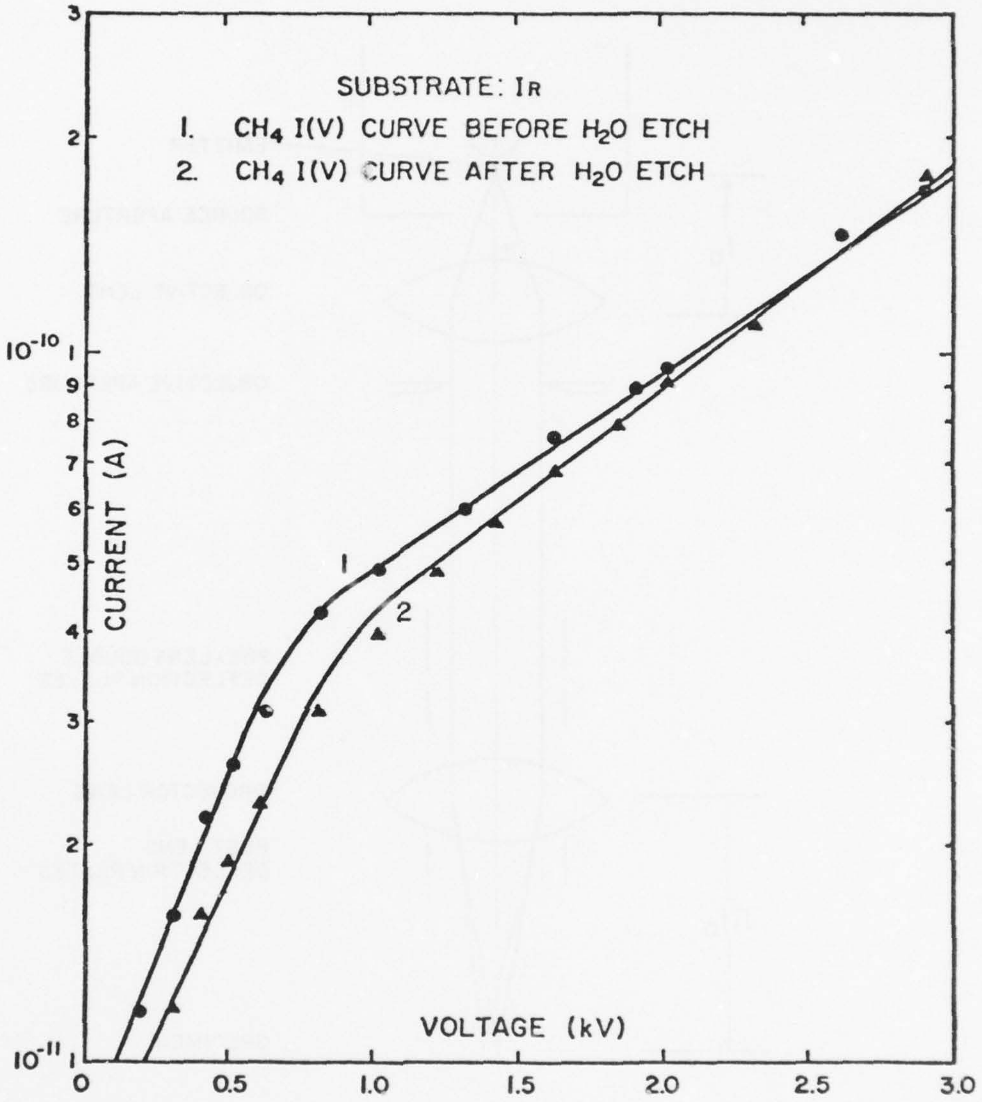

Figure 37. FI current vs voltage for an Ir emitter before and after 0.3-h exposure to H_2O at a pressure $P_{H_2O} = 10^{-4}$ torr.

AD-A072 541   OREGON GRADUATE CENTER BEAVERTON   F/G 14/2
FIELD ELECTRON AND ION SOURCE RESEARCH FOR HIGH DENSITY INFORMA--ETC(U)
NOV 78   L W SWANSON   F33615-76-C-1327

UNCLASSIFIED   AFAL -TR-78-174   NL

2 OF 2
AD
A072541

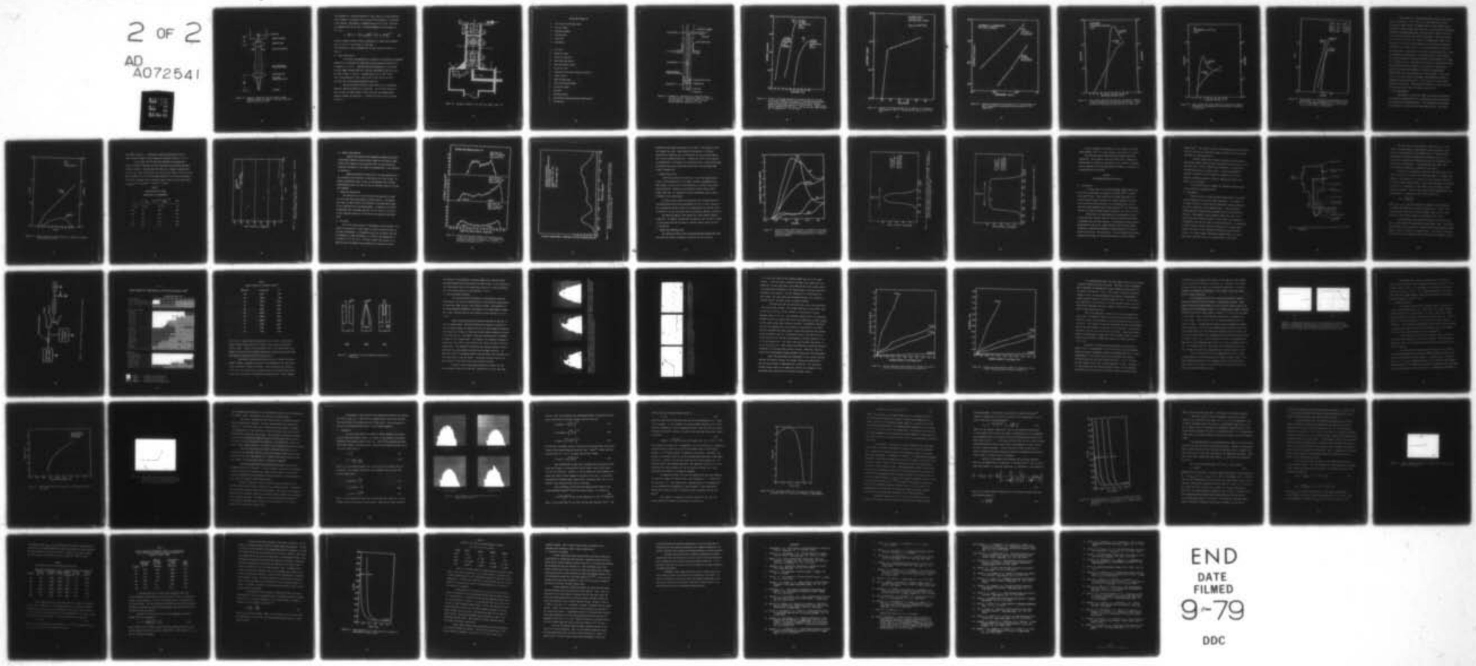

END
DATE
FILMED
9-79
DDC

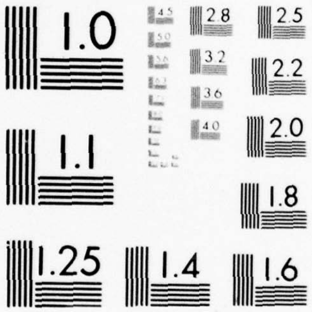

MICROCOPY RESOLUTION TEST CHART
NATIONAL BUREAU OF STANDARDS-1963-A

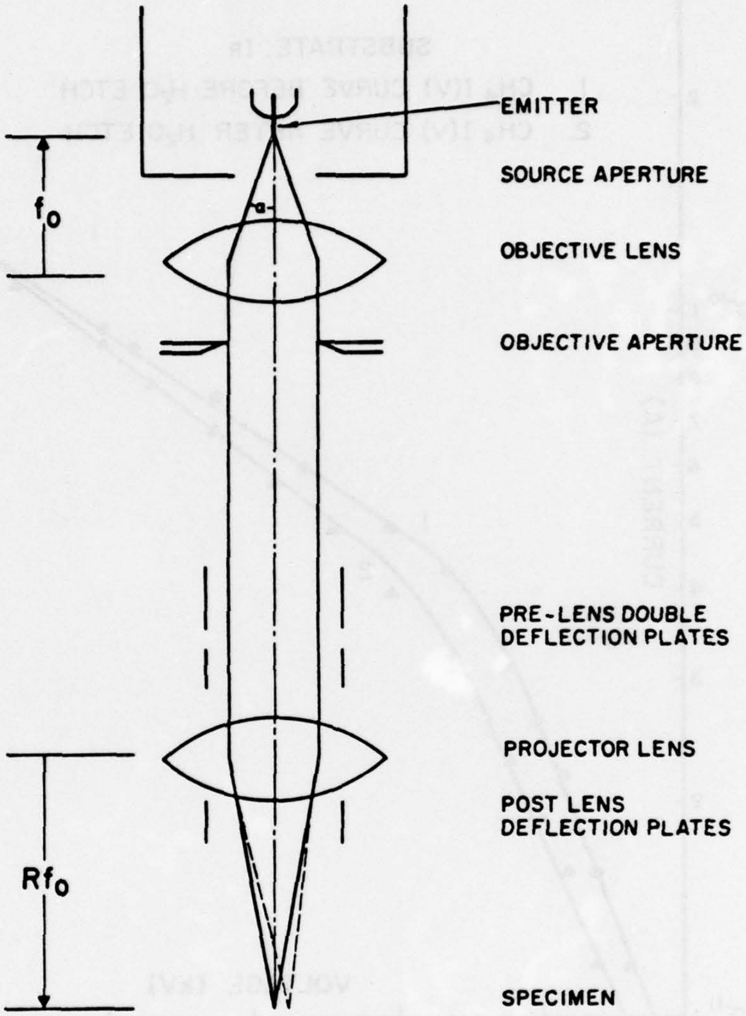

Figure 38. Schematic diagram of the SIM optical system (beam deflectors not shown). Only one deflection system is used at a time.

the specimen at a working distance of $\approx Rf_o$, where f_o is the objective focal length $\approx$ 5-7 mm and R is the ratio of the projector to objective focal lengths. The amount of demagnification is $M' = R/M$. The overall magnification is $R = MM'$. The beam diameter on the specimen is $d_2 = 2\ r_2$,

$$r_2 = \left\{(M' r_1)^2 + \left[1/4\ C_{s_2} \left(\frac{\alpha}{R}\right)^3\right]^2 + \left[1/2\ C_{s_2} \frac{\Delta V}{V} \frac{\alpha}{R}\right]^2\right\}^{1/2} . \qquad (38)$$

With our present lenses we have a predicted $d_2 \approx 6300$ Å with hydrogen ($\Delta V \approx 4$ eV) at $V = 12$ kV and $\alpha = .012$ rad.
The microprobe is shown schematically in Fig. 39 and the source in Fig. 40.

D. Source Sensitivity

Ion current was measured as a function of H_2 pressure and emitter temperature to determine the important source parameter sensitivity S, in amperes Sr^{-1} $torr^{-1}$. Sensitivities were referenced at 3 kV above the Best Image Voltage (BIV) or 3 kV above the break in the I-V curve as shown in Figs. 41 and 42. Sensitivities of $\approx 7 \times 10^{-7}$ A Sr^{-1} $torr^{-1}$ were measured at 294 K and 5×10^{-5} A Sr^{-1} $torr^{-1}$ at 77 K (see Fig. 43), with polycrystalline Ir emitters.

The ion microprobe has been tested with H_2, Ar, Xe and CH_4 (methane) with polycrystalline Ir emitters. An I-V curve for H_2 is shown in Fig. 44, where probe current refers to the focussed beam accepted through the aperature. A similar I-V curve for Ar is shown in Fig. 45.

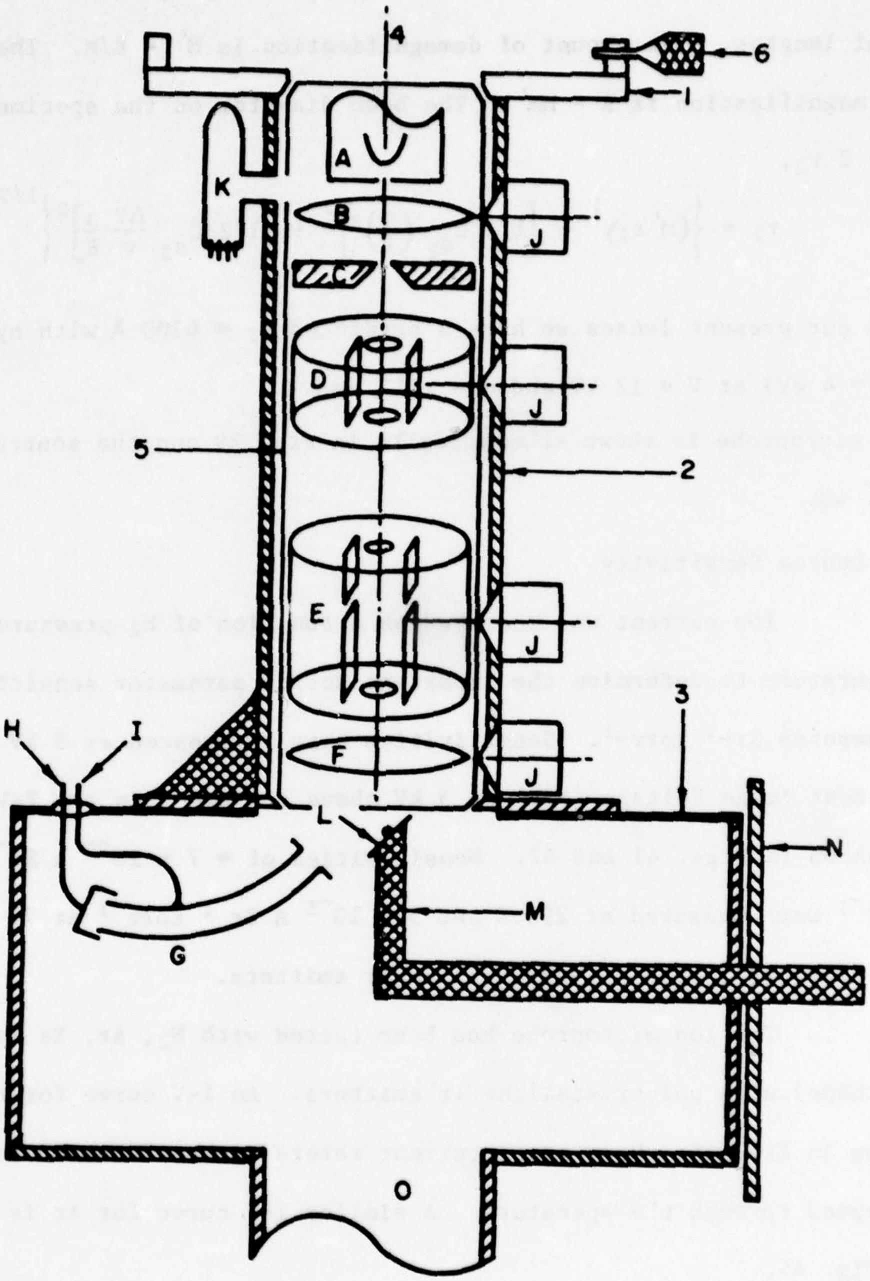

Figure 39. Schematic diagram of the SIM (see legend, page 83).

LEGEND FOR FIGURE 39

1. Ion source traversing stage
2. Vacuum column
3. Specimen chamber
4. Optical axis
5. Lens tube
6. Micrometer

A. FI source

B. Objective lens

C. Objective aperture

D. Beam steering plates

E. Beam deflection plates

F. Projector lens

G. Channeltron secondary electron detector

H. Signal output

I. High voltage input

J. Electrical feedthroughs

K. Ionization Gauge

L. Specimen

M. Specimen holder

N. Vacuum door holding specimen manipulators

O. Vacuum port

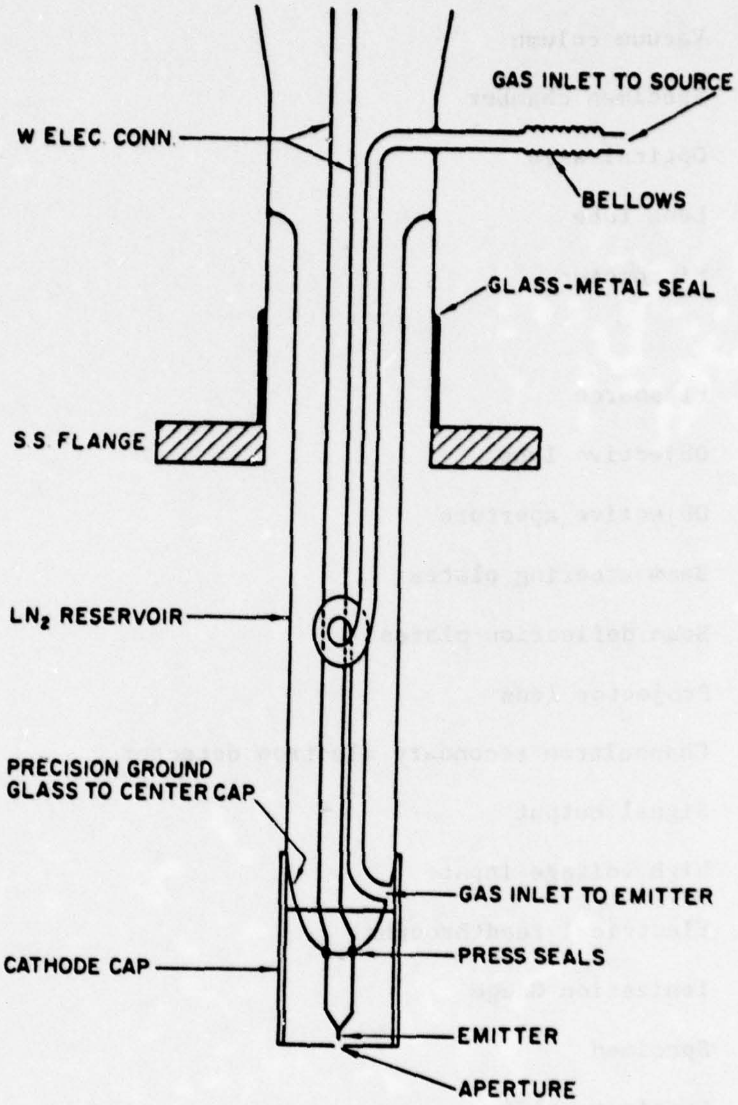

Figure 40. Diagram of a differentially pumped FI source. Filling the inner dewar with liquid N_2 cools the gas and emitter. Aperture size is 0.5 mm, emitter-aperture spacing 0.5-1.5 mm.

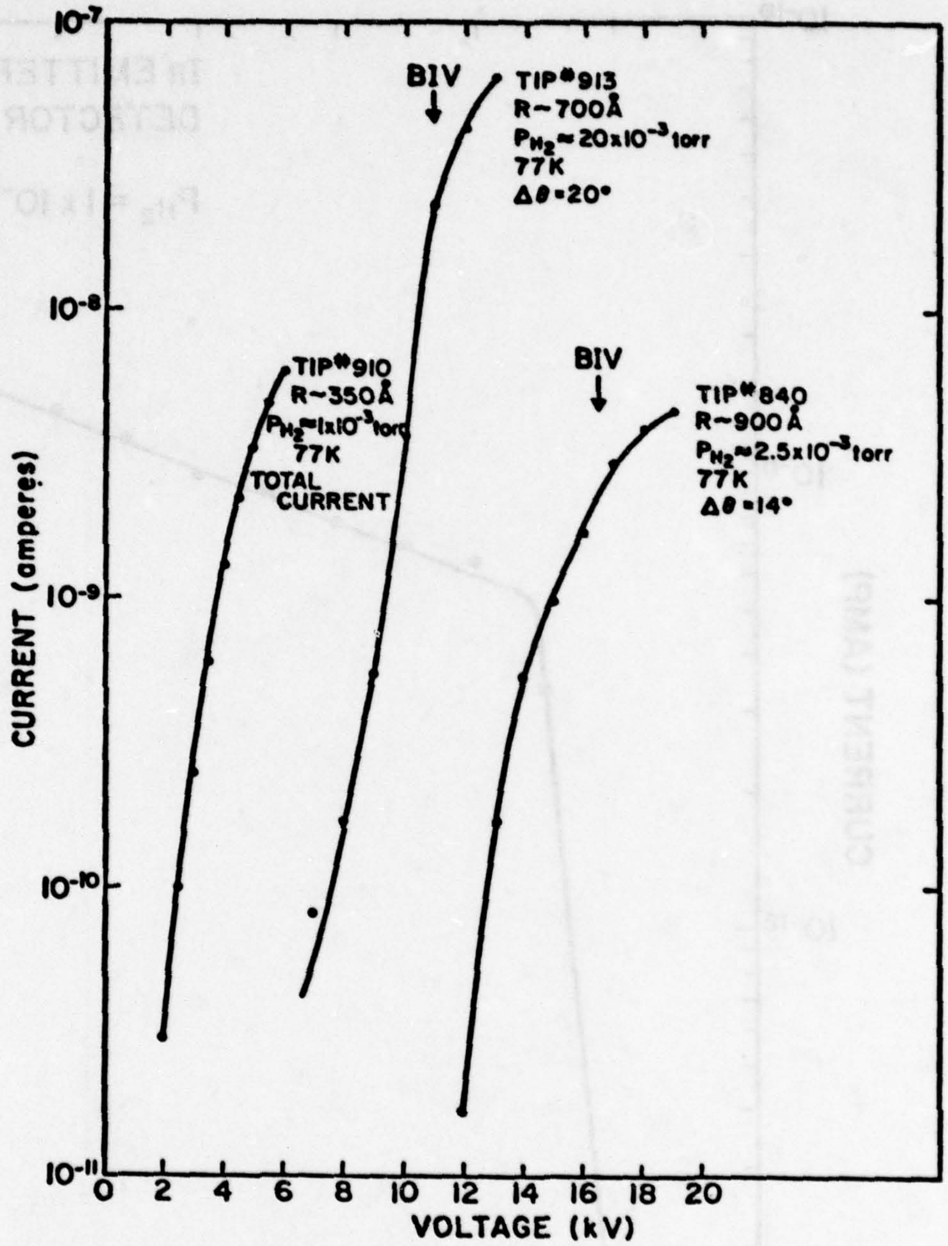

Figure 41. Current vs voltage measured for three emitters of varying radii and at various H_2 pressures in the high vacuum system. Current from emitters 840 and 913 was extracted through apertures with solid angles of 0.19 and 0.38 sr, respectively. Emitter temperatures were 77 K. BIV is the best image voltage and corresponds to ~ 2 x 10^8 V/cm.

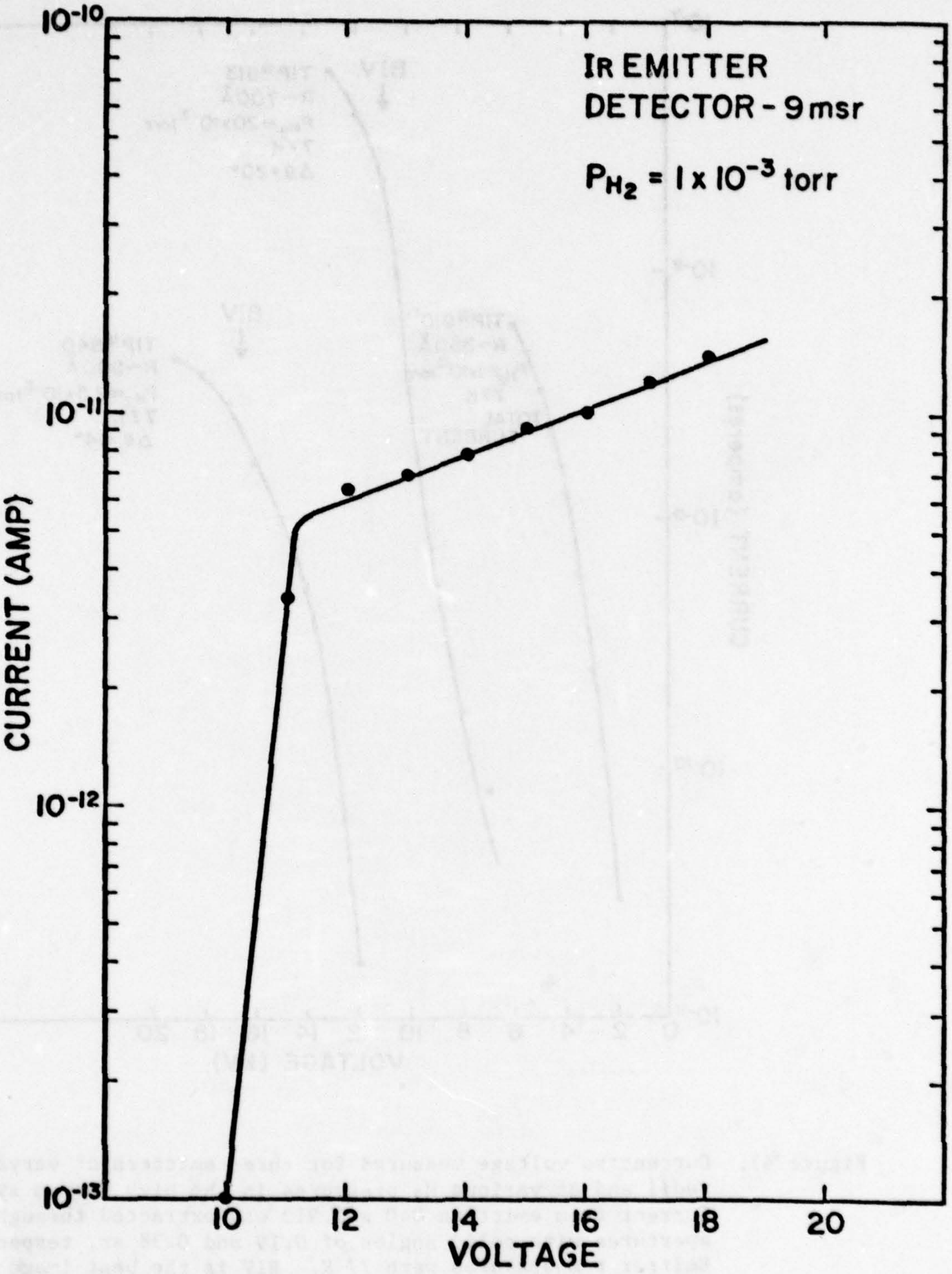

Figure 42. Current vs voltage measured for an emitter in the optical bench system at 294 K. The sensitivity was 1 x 10^{-6} A sr^{-1} $torr^{-1}$.

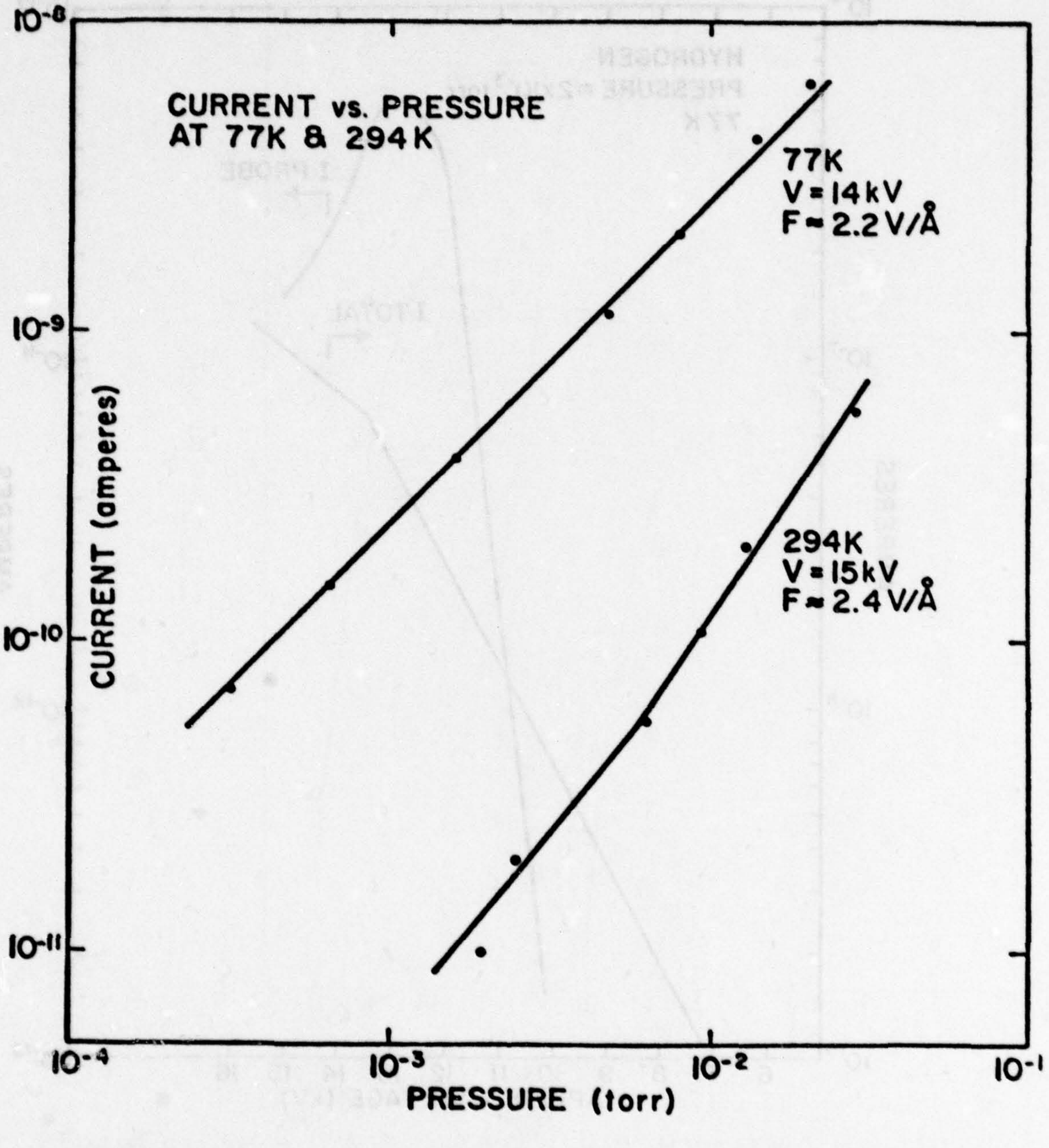

Figure 43. Current vs pressure for an emitter at 77 K and another at 294 K, showing the increased current available at low temperature.

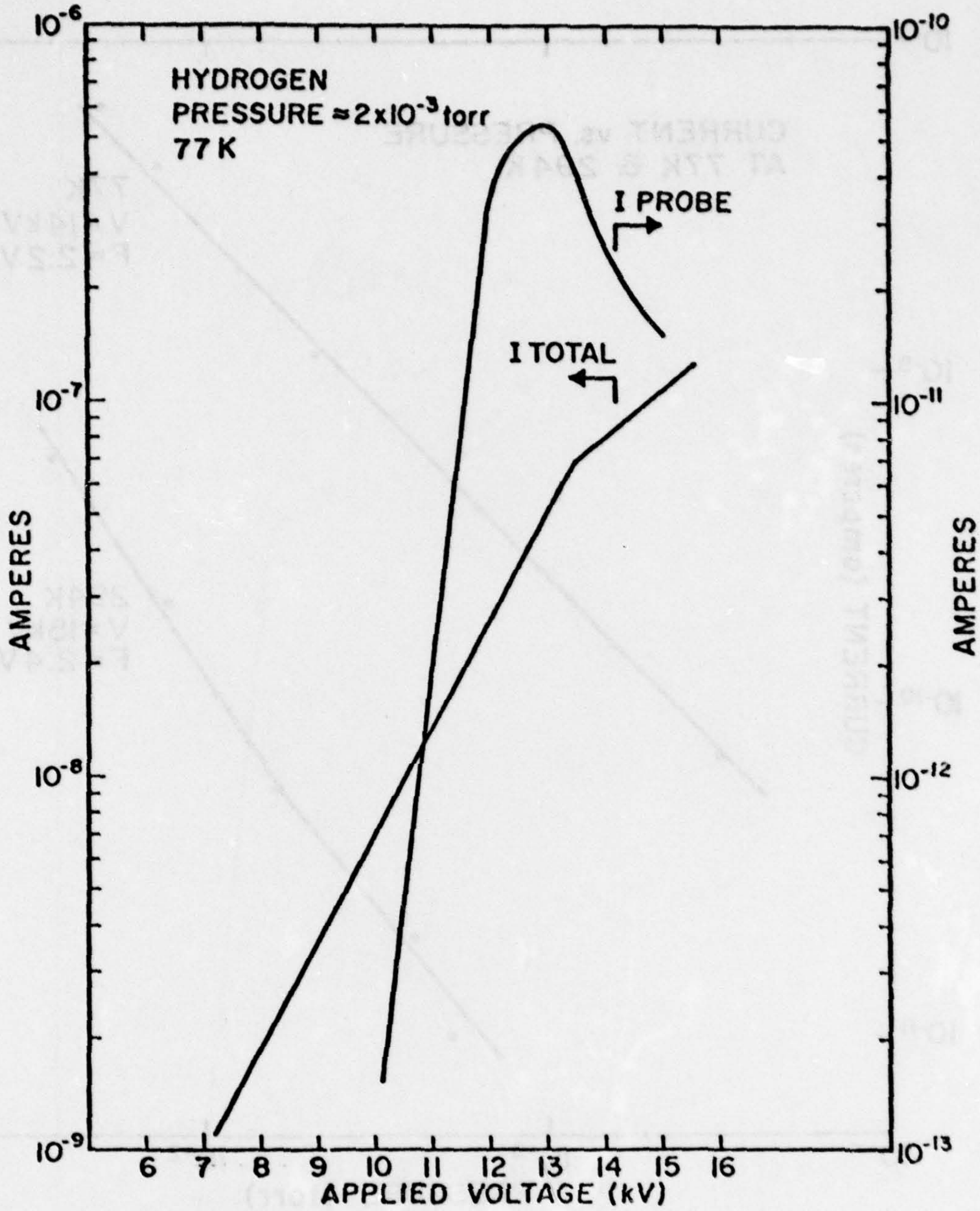

Figure 44. Probe current and total current as a function of emitter voltage as measured in the SIM near the specimen. Angle subtended by the objective aperture was α = 0.012 rad.

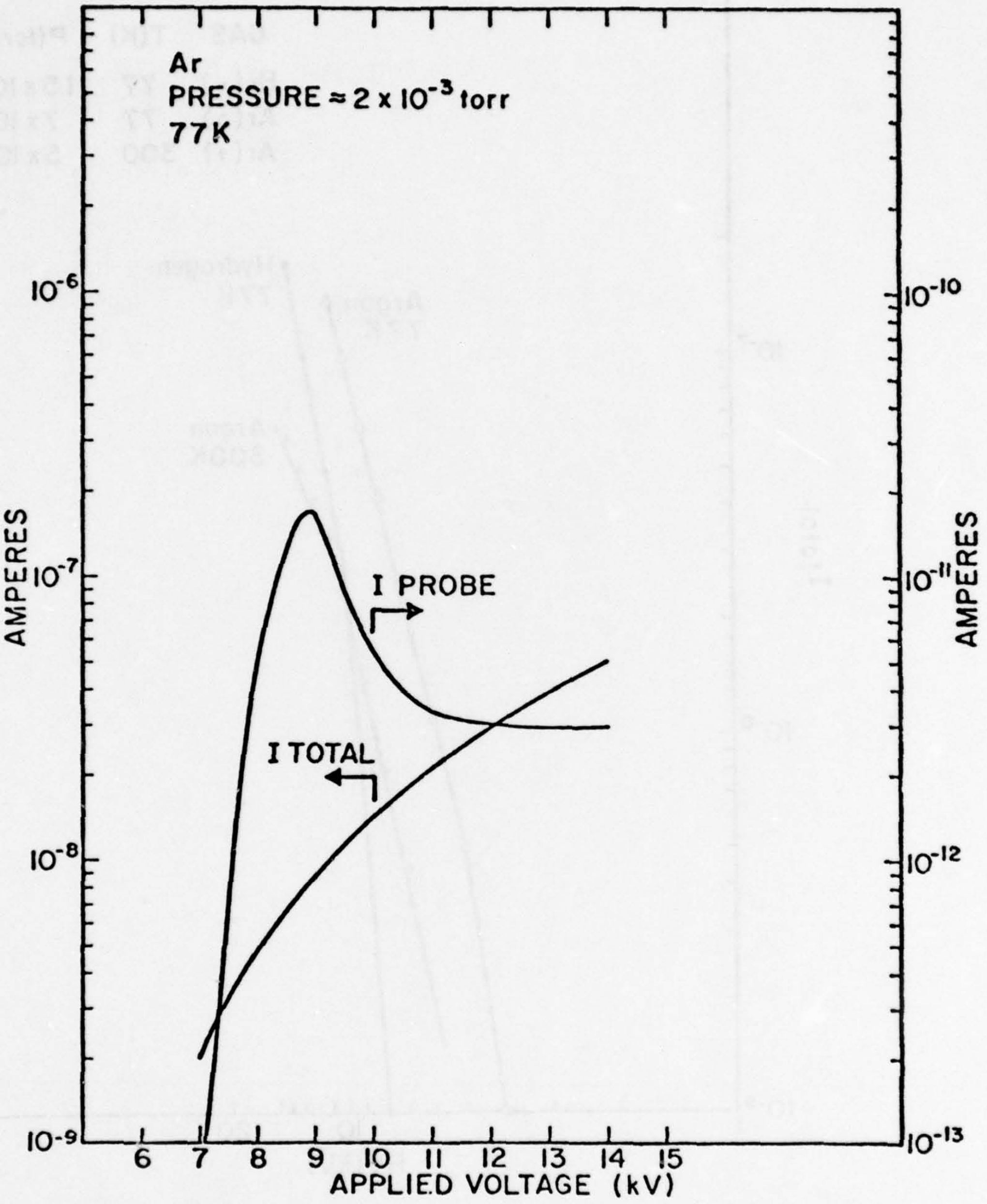

Figure 45. Probe current and total current as a function of emitter voltage for Ar as measured in the SIM near the specimen, $\alpha = 0.012$ rad.

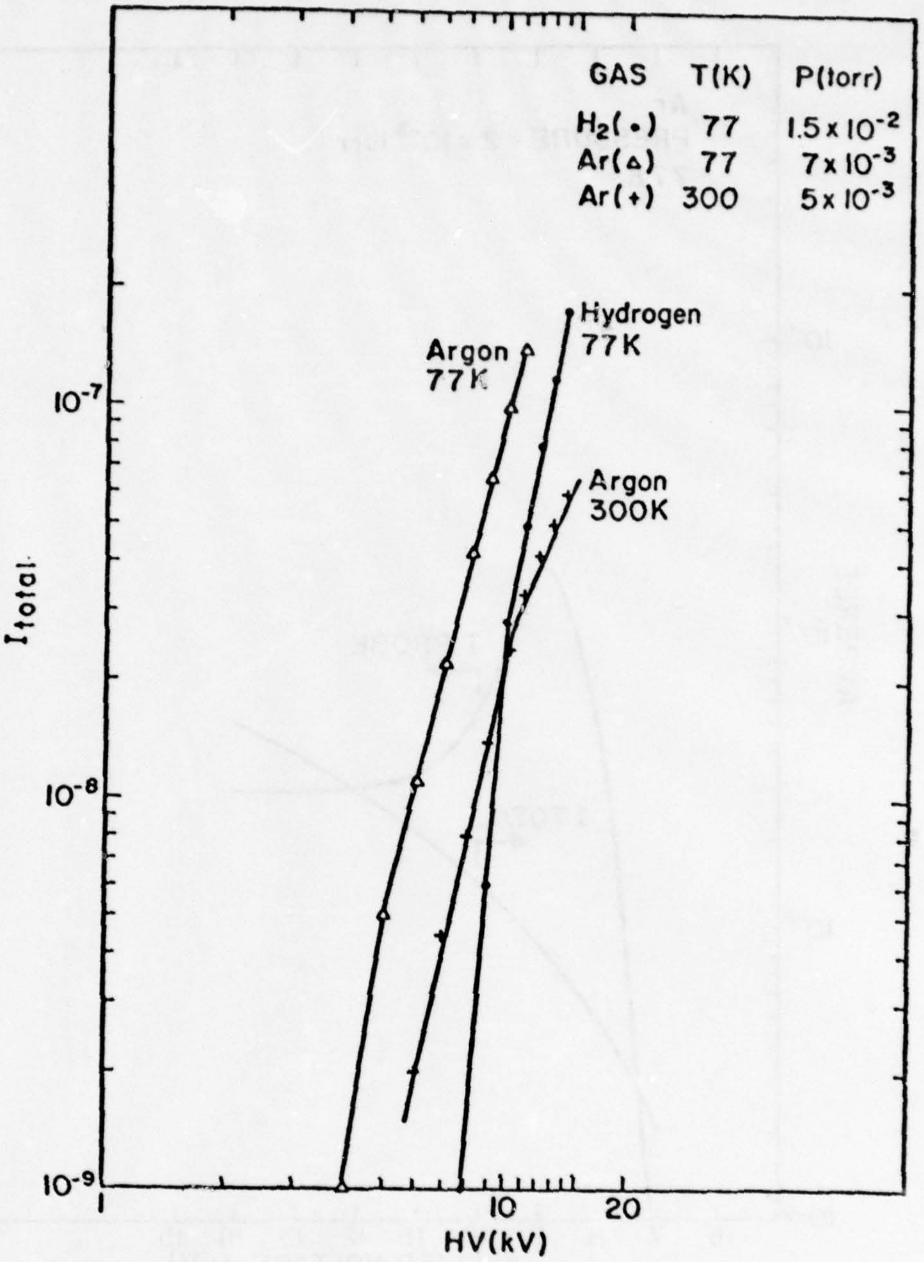

Figure 46. Total current vs voltage with the same emitter for H_2 and Ar gases. Note the shift in the I-V curve for Ar at 77 K. Ionization potentials are I_p = 15.7 eV and 15.6 eV for Ar and H_2, respectively.

Total current vs. voltage measurements with the same emitter and at a pressure of $\sim 10^{-2}$ torr at 77 K were made with Ar and H_2. The results, shown in Fig. 46 suggests that Ar forms liquid films on the emitter surface under these conditions. Since Ar and H_2 have almost identical ionization potentials, one would expect similar I-V curves if the ionization takes place from the gas phase. That the break in the I-V curve for Ar at 77 K occurs at a substantially lower voltage than for H_2 or for Ar at 294 K means that the ionization probability is greater at 77 K than at 294 K. Since the ionization probability is proportional to the product of the barrier penetration factor, which is independent of temperature, and the dwell time of the atoms near the ionization region, the dwell time must be much greater ($\sim 10^8$ times) at 77 K than at 294 K. This would be the case if a liquid film formed. Film formation can occur because at the emitter tip the pressure is greater than the source pressure by a factor of approximately $\exp(\alpha F^2/2kT)$ due to the polarization of the gas atoms. In the case of Ar, at the fields used, the pressure and temperature should be somewhat below the triple point. In the case of Xe, solid layers should form at the tip. This seems to be borne out by the low probe current seen with Xe (Fig. 47) with the tip at 77 K.

E. Noise Measurements

The signal to noise ratio (S/N) of the source was measured by attaching a photomultiplier to the phosphor screen and analyzing its output with a spectrum analyzer. The photomultiplier subtended a solid angle of ≈ 9 msr and the source was at 294 K. The results

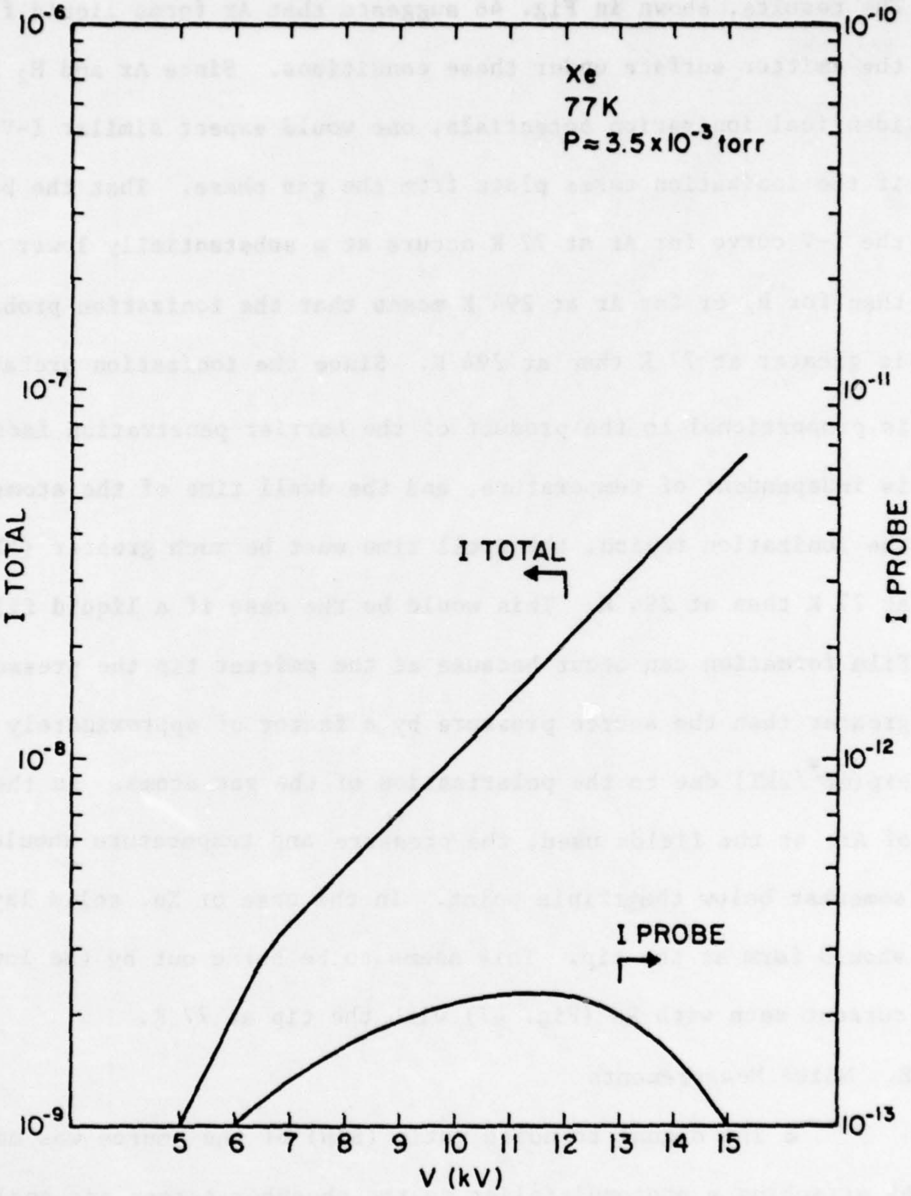

Figure 47. Total current and probe current as a function of emitter voltage for Xe at 77 K.

are shown in Table 4. The spectral densities measured with the beam on and the beam off were essentially identical above $f = 15$ Hz.

In the SIM, the S/N ratio was measured by allowing the beam to strike the specimen and then analyzing the amplified secondary electron current. The analysis was done with a computer program with a $\Delta f = 2$ Hz. The S/N was found to be ≈ 40 in the range $1 \text{ Hz} < f > 11 \text{ Hz}$, with the source at 77 K and the beam limited by a 0.15 msr solid angle. The noise to signal ratio is shown in Fig. 48 where on the scale shown, $(\langle I^2_{SHOT}\rangle)^{1/2} = (2eI\Delta f)^{1/2} \approx 0.06$ ($\Delta f = 10$ Hz).

TABLE 4

NOISE DATA FOR FI BEAM

TAKEN WITH 10 HZ BANDWIDTH

f	$I - I_{BG}$	$\langle \Delta I^2\rangle^{1/2} - \langle \Delta I^2_{BG}\rangle^{1/2}$	S/N
1 Hz	21 μA	0.5 μA	42
10	21	0.2	105
60	21	0.2	105
1	11	0.5	22
10	10	0.1	100
60	10	0.1	100

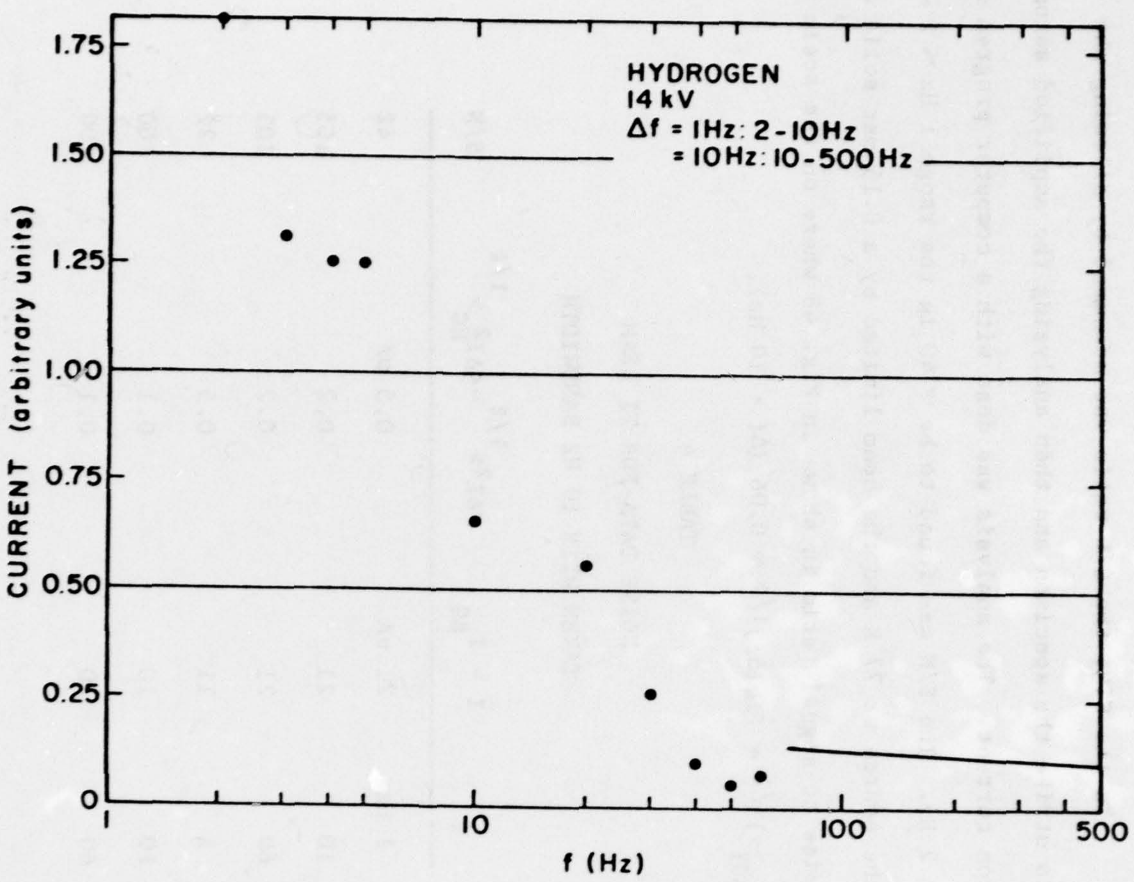

Figure 48. Noise to signal ratio of the FI current vs frequency. Solid line represents average of many data points.

F. Angular Distributions

Angular distributions were measured by using a four-plate electrostatic deflection system which caused the ion beam to sweep across a slit aperture which subtended 30 mr in the direction of deflection and 300 mr in the direction perpendicular to the direction of deflection.

Angular distributions shown in Fig. 49 were measured with two different polycrystalline Ir emitters at 294 K with H_2 gas. An angular distribution shown in Fig. 50 was measured with a movable photomultiplier which was swept across the phosphor screen of the gun test assembly.

G. Resolution Measurement

The resolution of the ion microprobe was measured in order to verify that the system worked as theory predicts. Micrographs were taken of small objects (field emitters) and measurements made on the negatives with a microdensitometer. A resolution of 6700 Å was measured with a hydrogen beam ($\Delta V \approx 4$ eV), which is very close to the predicted resolution of 6300 Å with the system as described above.

H. Life Tests

Due to the limited supply of experimental vacuum stations, life tests on a statistically large number of field ion emitters have not yet been accomplished. A preliminary test of an Ir emitter was made by running it at 100% overvoltage (≈ 4 V/Å) at room temperature in a vacuum of $\approx 3 \times 10^{-6}$ torr. This was a severe test because it is expected that the primary failure modes will be chemical etch and

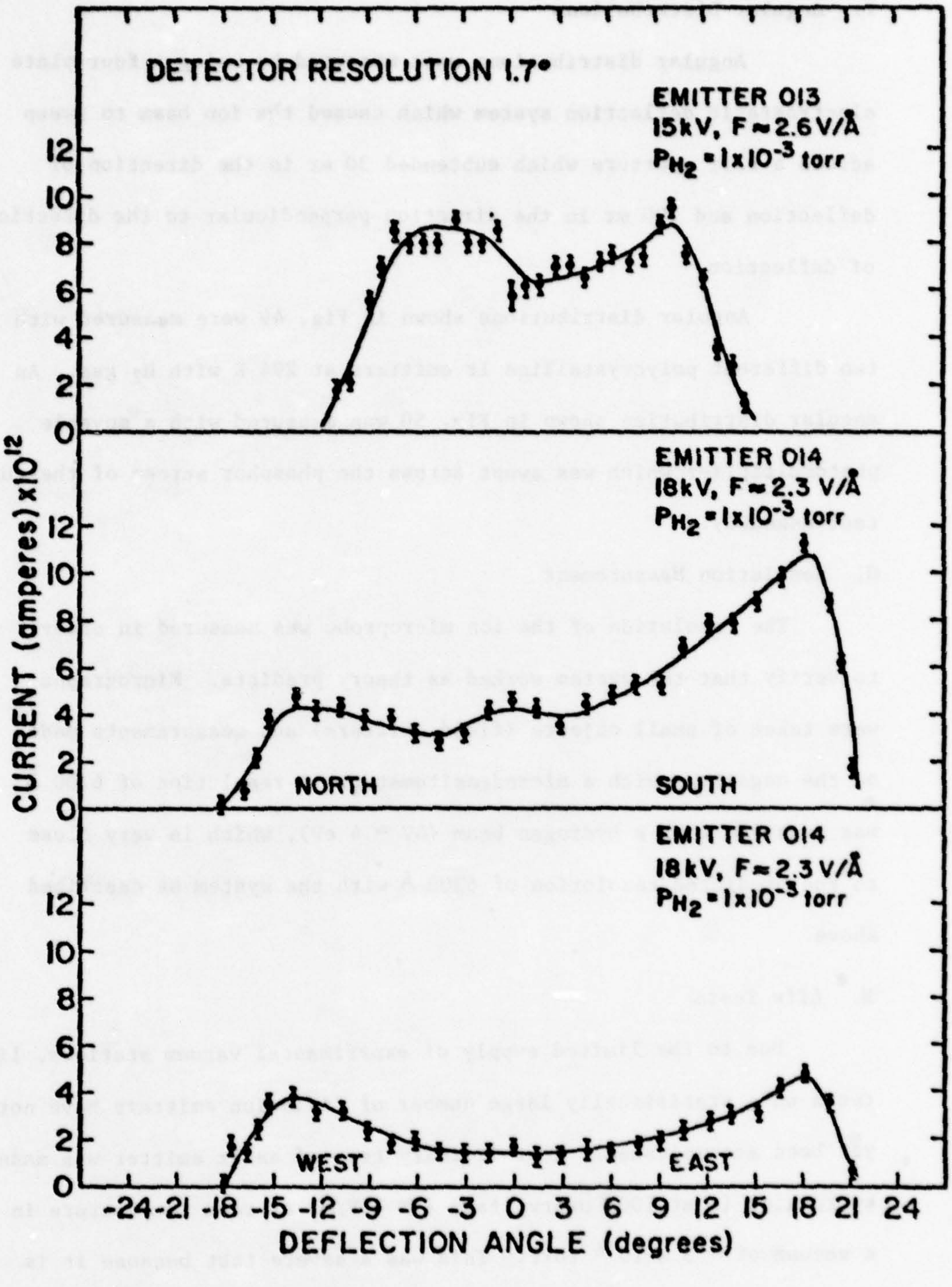

Figure 49. Angular distributions measured in the optical bench at 300 K for emitters 013 and 014. Note symmetry for orthogonal directions of emitter 014. Detector resolution was 30 mrad (1.7°).

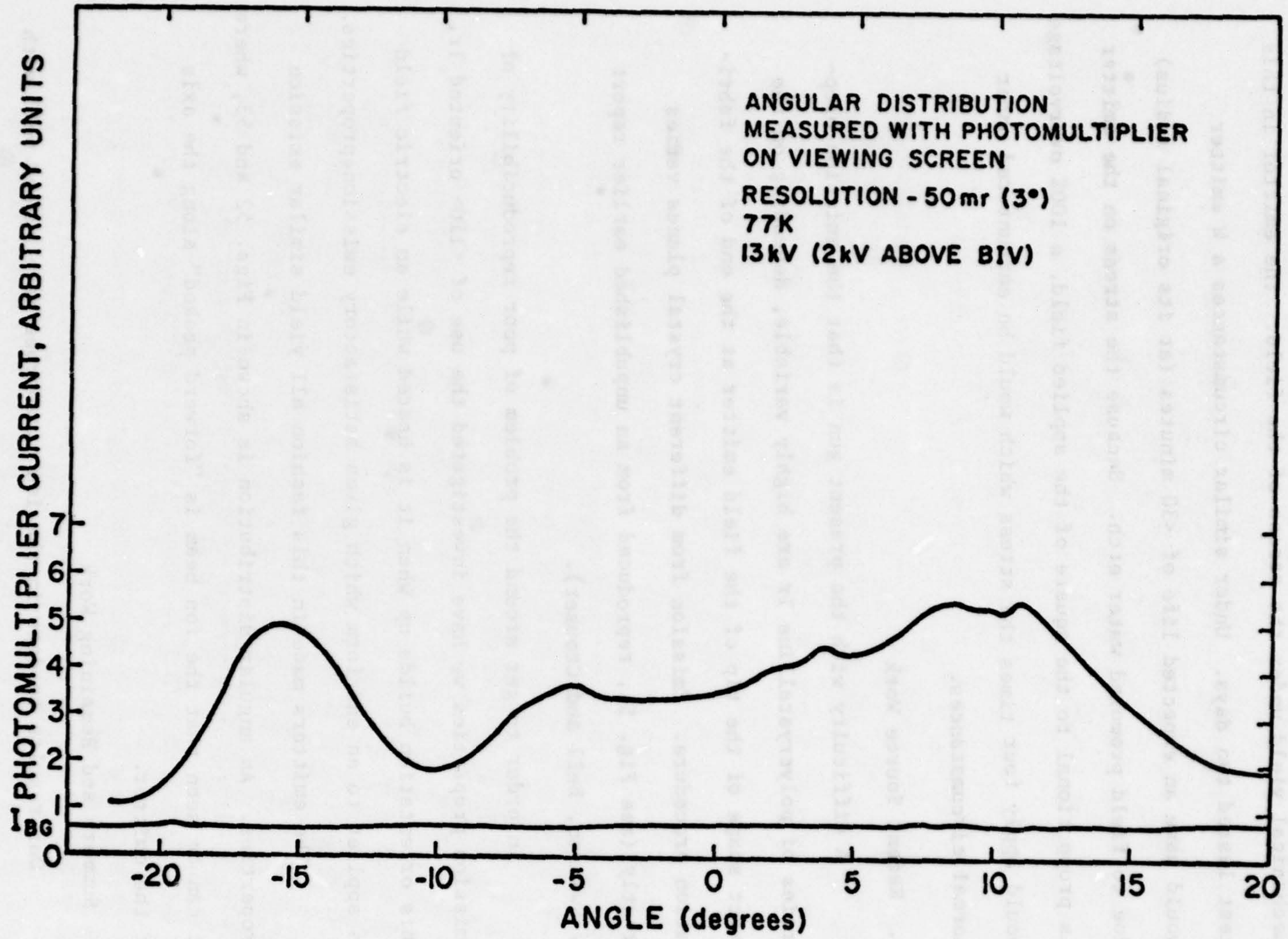

Figure 50. Angular distribution measured in a high vacuum system with a photomultiplier apertured to accept 3°, as seen from the emitter. I_{BG} is the photomultiplier reading with the emitter voltage off.

mechanical yield under the stress of the field. The emitter in this test lasted two days. Under similar circumstances a W emitter would have an expected life of <30 minutes (at its original radius) due to field promoted water etch. Because the stress on the emitter is proportional to the square of the applied field, a 100% overvoltage would apply four times the stress which would be encountered under normal circumstances.

I. Recent Source Work

A difficulty with the present gun is that the emission properties of polycrystalline Ir are highly variable, depending on the exact shape of the tip of the field emitter at the end of the fabrication procedure. Emission from different crystal planes varies greatly (see Fig. 51, reproduced from an unpublished earlier report by Swanson, Bell and Crouser).

In order to get around the problem of poor reproducibility of emission properties we have investigated the use of <110> oriented Ir. This orientation builds up when it is heated while an electric field is applied to an end form which gives satisfactory emission properties. The emitters made in this fashion all yield similar emission properties. An angular distribution is shown in Figs. 52 and 53, where it can be seen that the ion beam is "forward peaked" along the axis of the emitter.

J. Summary and Remaining Work

Our results to date in the ion microprobe have agreed well with our predictions based on measured properties of the FI source.

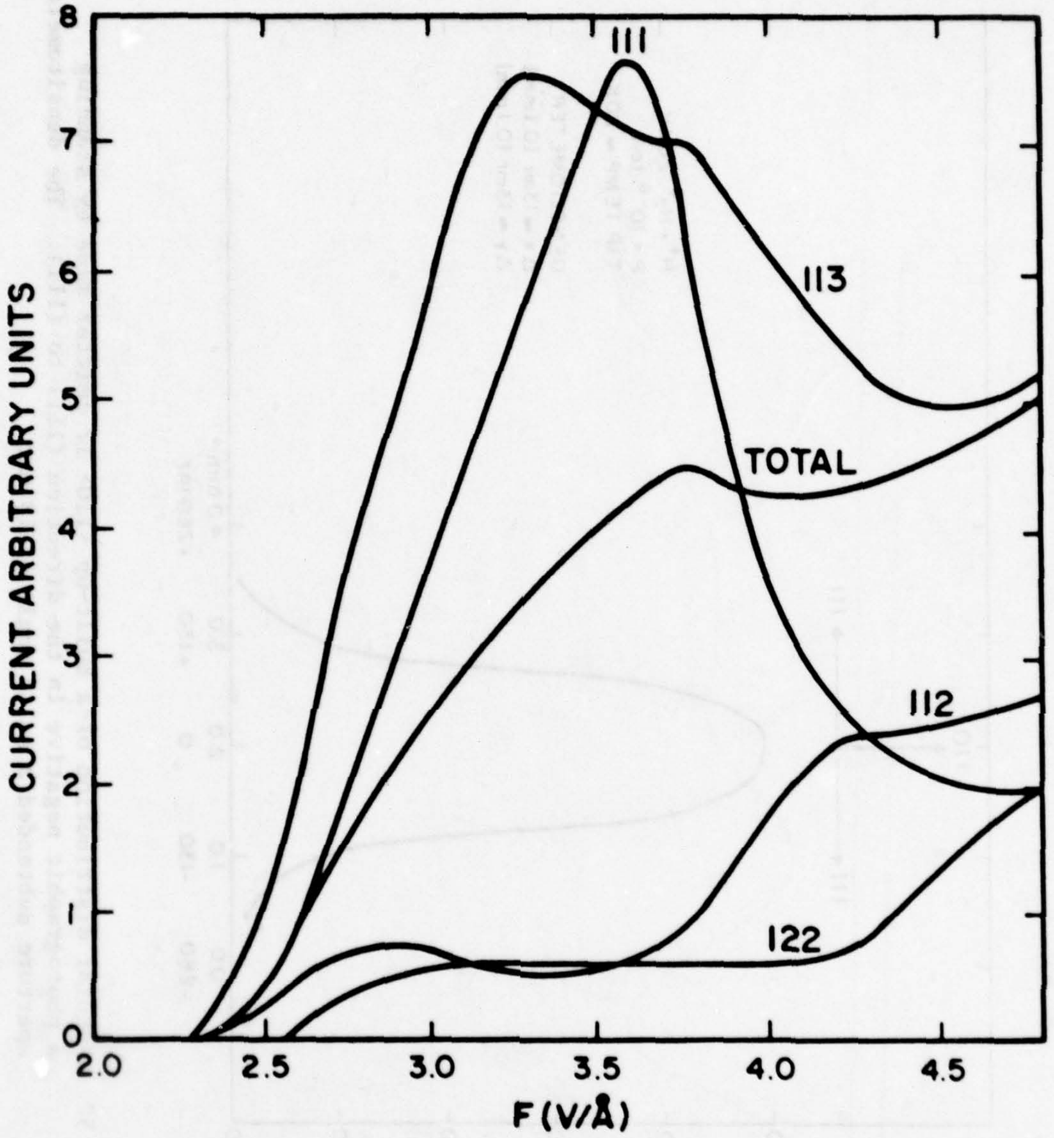

Figure 51. Current-voltage characteristics of different crystalline facets of a W emitter showing the effects of local field variation (reproduced from unpublished work of Swanson, Bell and Crouser).

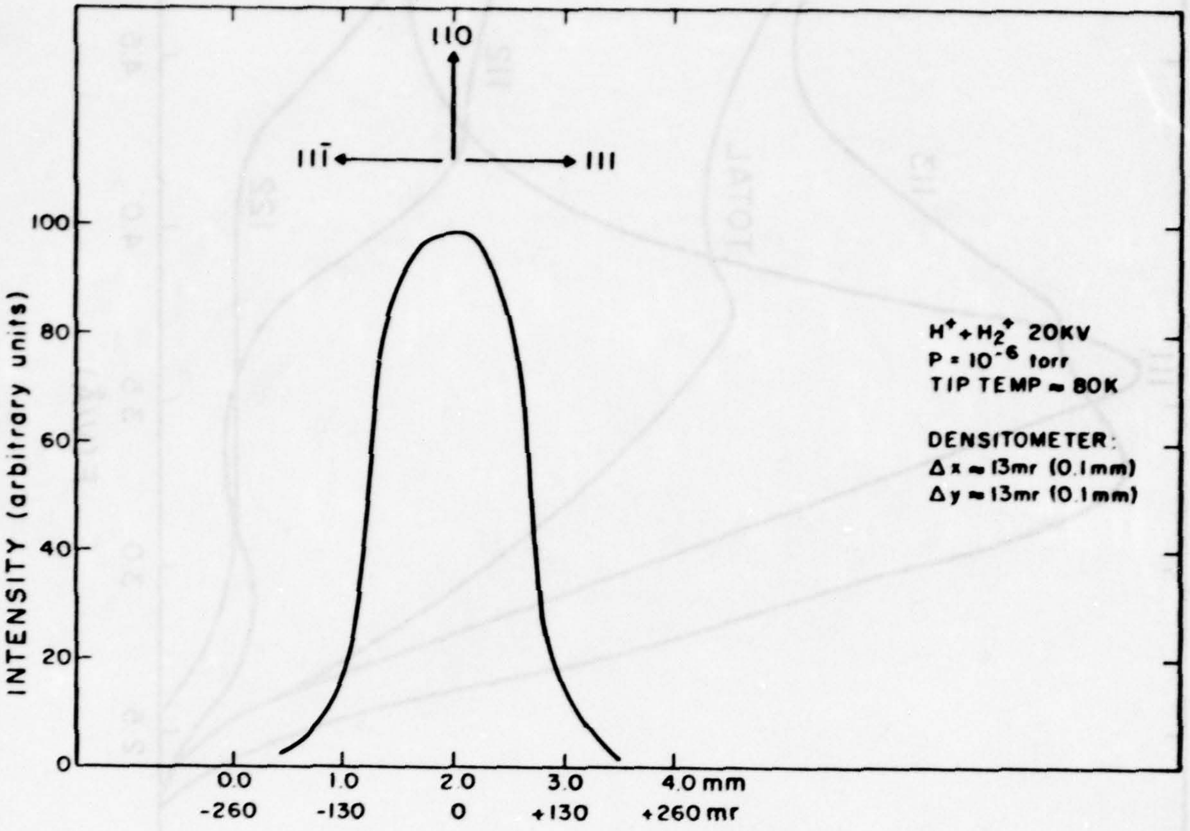

Figure 52. Angular distribution of a built-up <110> Ir emitter made by scanning a photographic negative in the direction (11$\bar{1}$) to (111). The densitometer aperture subtended a solid angle of 13 msr.

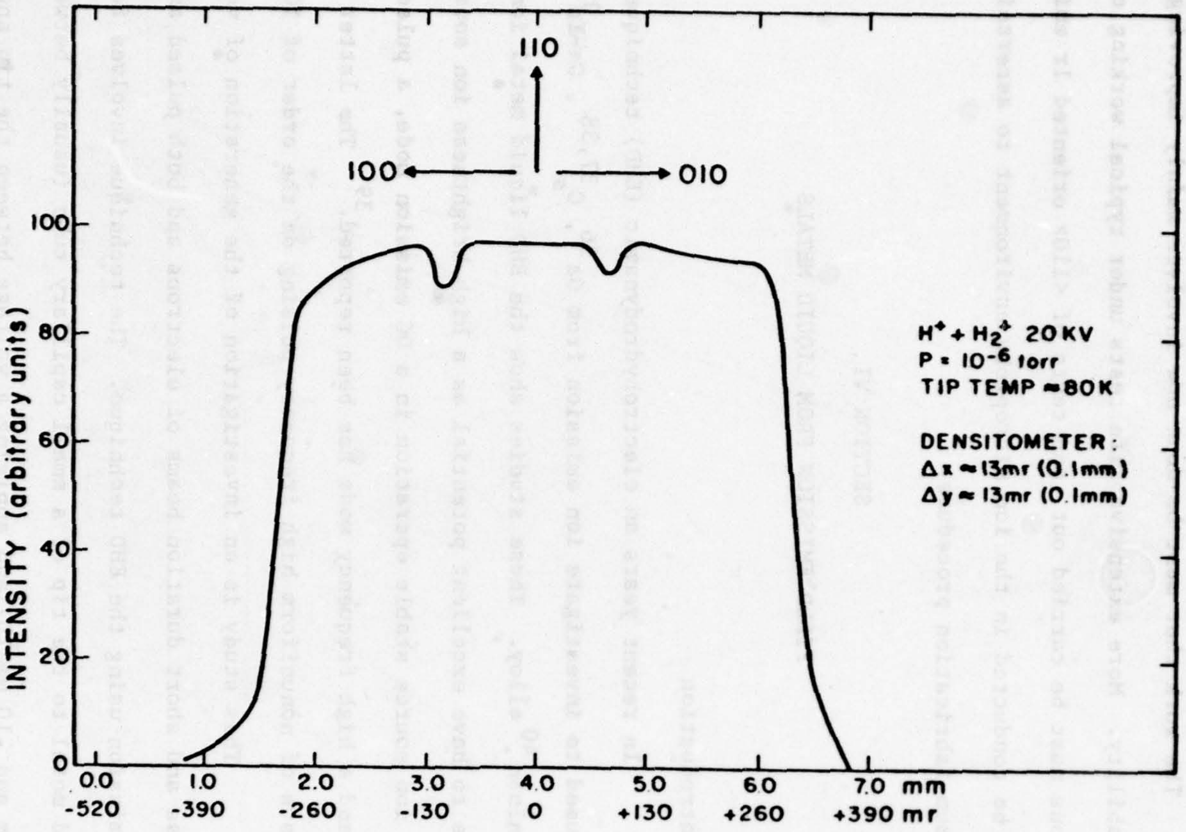

Figure 53. Same as Figure 52 except scan was along (100) to (010) direction.

We are confident of the ability of the FI source to provide useful amounts (>10^{-11} A) of ion current at resolutions of ≈ 1000 Å.

The work that must be done now involves mainly improving reliability. More extensive life tests under typical working conditions must be carried out, and tests of <110> oriented Ir emitters must be conducted in the ion microprobe environment to ascertain the optimum fabrication procedure.

SECTION VI

FIELD EMISSION FROM LIQUID METALS

A. Introduction

In recent years an electrohydrodynamic (EHD) technique has been used to investigate ion emission from Ga[36], C_s[37,38], Ga-In[39], and GaInSn[40] alloy. These studies show the EHD liquid metal ion source to have excellent potential as a high brightness ion source. As an ion source stable operation in a DC emission mode, a pulse mode and a high frequency mode has been reported.[39] The latter mode consists of nonuniform high frequency pulsing on the order of 100 kHz.

This study is an investigation of the generation of very intense and short duration beams of electrons and both pulsed and dc ion emission using the EHD technique. The technique involves feeding liquid metal to the tip of a small capillary tube (usually between .02 mm and .10 mm ID) and applying a voltage between the tip and an extractor electrode. The interaction of the electrostatic and surface tension forces causes the liquid metal meniscus to form a sharply peaked cone.[41] The electric field at the liquid metal-vacuum interface near the cone apex is sufficiently high to extract ions or electrons depending on the field polarity.

Taylor[41] showed that through the balance of electrostatic and surface tension forces a stable cone-shaped structure with a 49.3° cone half angle could be formed from the meniscus of a liquid protruding from the end of a small nozzle. The exact mechanism of emission, although not fully understood, appears to be a field emission initiated process for electron emission and field evaporation for ion emission.

In this study we have examined the emission characteristics from a Ga/12% In liquid metal alloy.

B. Experimental

Figure 54 gives a cross-sectional representation of the EHD electron emission tube used for these experiments. The inside of the glass tube has a thin electrical conducting coating providing an electrical connection to the viewing screen. A glass capillary tubing supports a tungsten nozzle through which the liquid metal is supplied. The pressure control system by which the level of the liquid metal is controlled consists of two valves, one connected to a mechanical pump and the other to an argon gas source. By adjustment of these valves a positive pressure differential is created which controls the level of the liquid metal meniscus in the capillary tubing. In a later design a mechanical plunger driven by a micrometer drive was used to force the liquid metal to the nozzle.

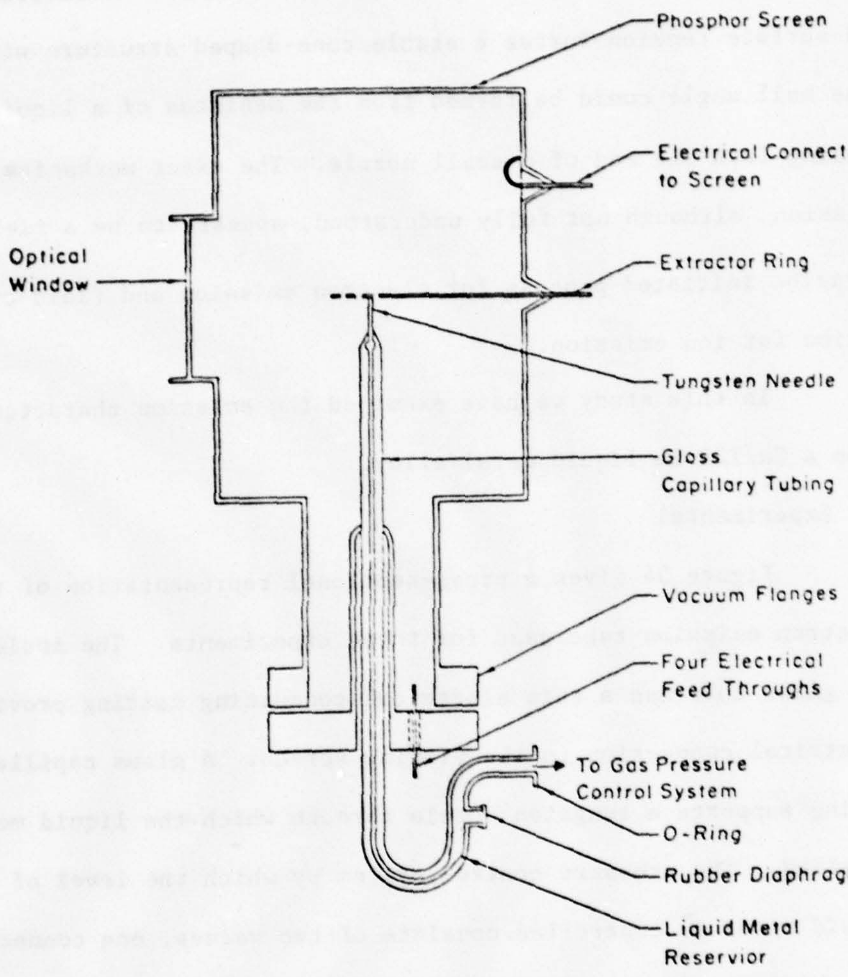

Figure 54. Diagram of the diode tube used to investigate the liquid Ga source.

The electrical circuit employed is shown in Fig. 55. The current limiting resistor, along with the tube capacitance, determined the time constant of the charging circuit. Average current measurements were made by replacing the attenuator and 50 Ω resistor with a parallel RC circuit across which the integrated pulse voltage level was measured. A high speed Tektronix Model 7904 oscilloscope was employed to examine the pulse shape.

Because of its resistance to attack by the liquid metal alloy, tungsten nozzles were used in this study (see Table 5). Tungsten was chosen not only because of its ability to resist attack by liquid Ga, but also its high surface tension. To aid the liquid metal in wetting the needle it is desirable for the needle to have as high a surface tension as possible. This is easily seen from the expression for the wetting angle of a liquid on a solid which is given by:

$$\cos\theta = \frac{\gamma_{SG} - \gamma_{SL}}{\gamma_{LG}}$$

where γ_{SG}, γ_{SL}, γ_{LG} are the interfacial tensions at the liquid-gas, solid-gas, and solid-liquid interfaces respectively. Table 6 which lists some metals and their surface tensions, shows W to be a good material in this respect because of the higher value of γ_{SG}.

Initial attempts with nozzles (a) and (b) of Fig. 56, were used to study emission from unsupported liquid metal cones. The emitter insert design of (c) consisted of a square cross section tungsten needle wedge fit into a 0.20 mm I.D. tungsten nozzle. The radius of curvature of the tip end of the tungsten needle formed by electrochemical etching

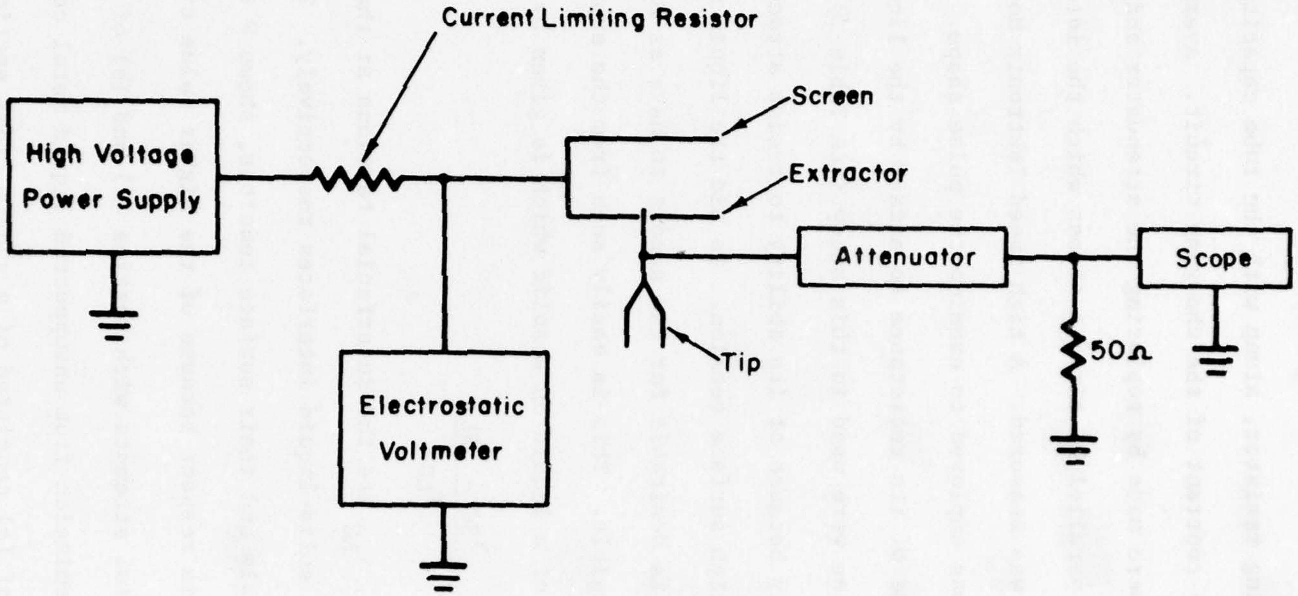

Figure 55. Circuit used to measure the pulse mode electron emission.

TABLE 5

RESISTANCE OF MATERIALS TO ATTACK BY GALLIUM [42]

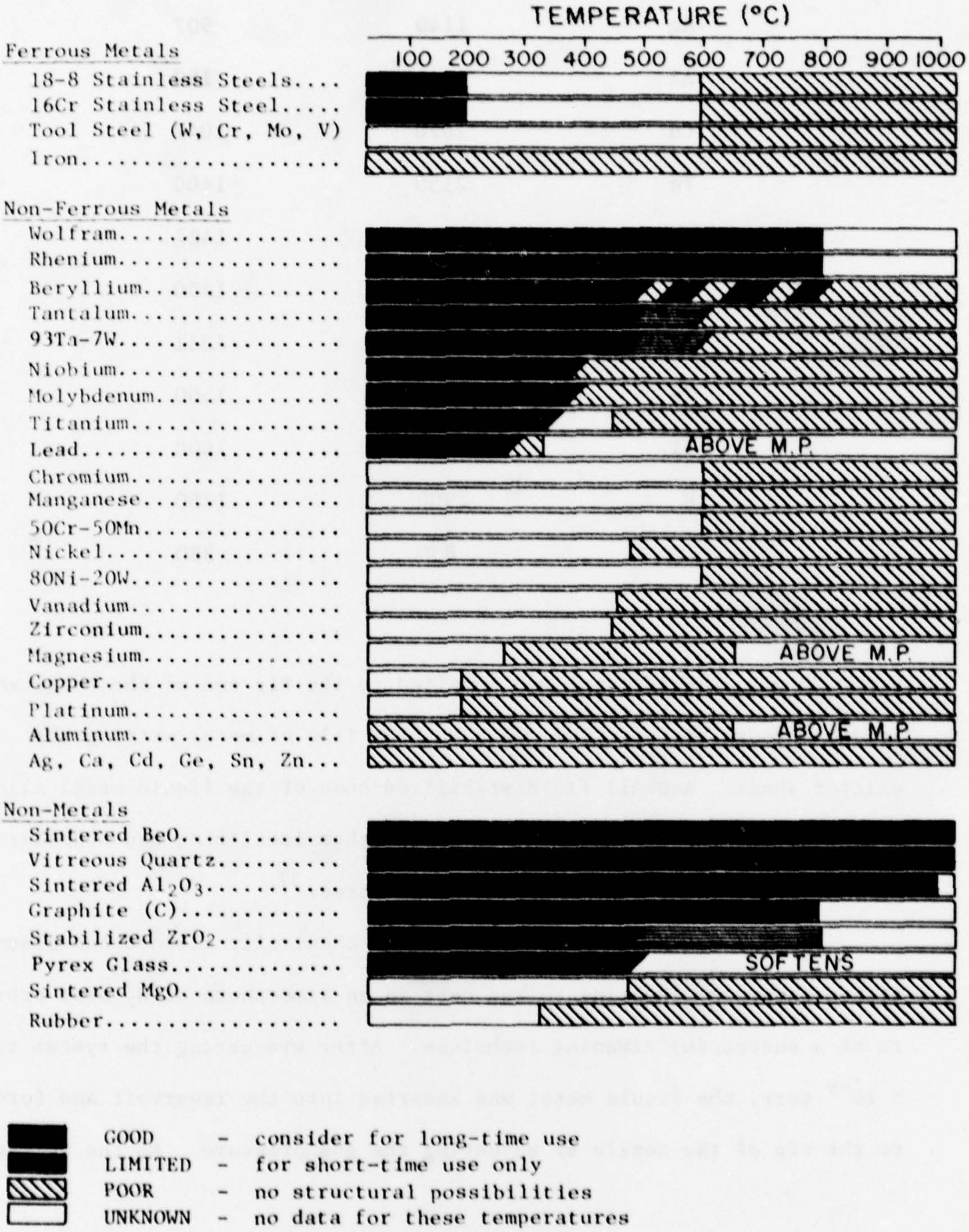

TABLE 6

SURFACE TENSION OF SELECTED SOLIDS[43]

Material	γ (dynes/cm)	T °C
Ag	1140	907
Al	1140	180
Cu	1670	1047
Fe	2150	1400
Mo	2200	1427
Ni	1850	1250
Pt	2340	1311
Ta	2680	1500
Ti	1700	1600
W	2900	1750
Zn	830	380

was ~ 20 μm. Liquid metal was supplied to the tip end of the tungsten needle through viscous flow via a surface film of metal wetting the emitter shank. A small field stabilized cone of the liquid metal alloy formed at the tip of the tungsten needle thus localizing and stabilizing the geometric position of the electron source.[37]

The nozzle structures were both chemically cleaned and plasma etched in argon. Heating to red heat in an atmosphere of H_2 also proved to be a successful cleaning technique. After evacuating the system to $\approx 10^{-7}$ torr, the liquid metal was inserted into the reservoir and forced to the tip of the nozzle by adjusting the gas pressure. As the voltage

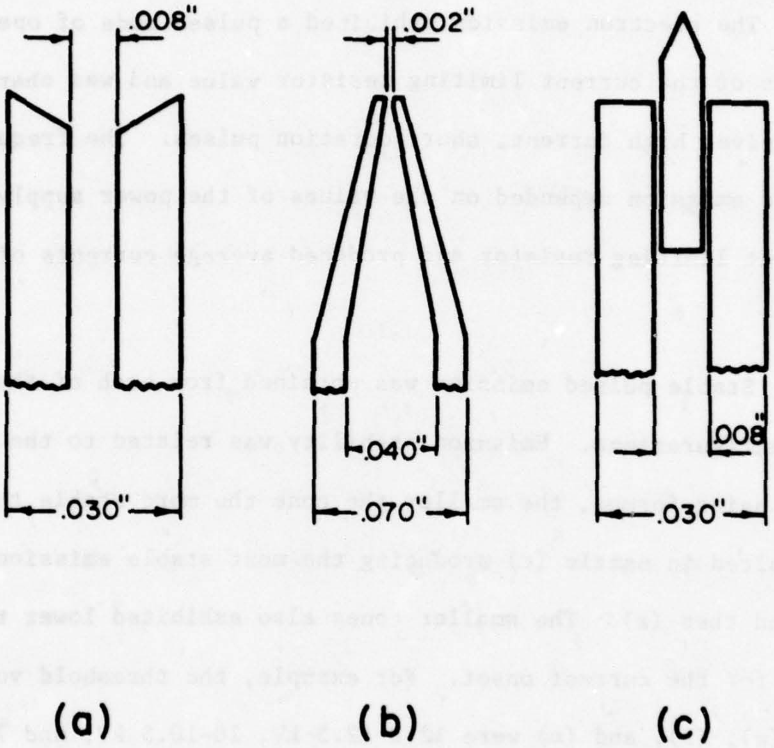

Figure 56. Diagram of the three tungsten nozzles used in this study.

was applied to the meniscus a cone was formed which could be easily observed through the 30 X microscope as shown in Fig. 57, for nozzle (b). The liquid metal used in this study was a Ga-In eutic alloy containing 12% In by weight which has a melting point of 18 C.

C. Electron Emission Results

The electron emission exhibited a pulsed mode of operation regardless of the current limiting resistor value and was characterized by repetitive, high current, short duration pulses. The frequency of the pulsed emission depended on the values of the power supply voltage and current limiting resistor and produced average currents of 1 μA to 6.5 mA.

Stable pulsed emission was obtained from each of the Fig. 56 nozzle configurations. Emission stability was related to the size of the cone being formed, the smaller the cone the more stable the emission. This resulted in nozzle (c) producing the most stable emission, followed by (b) and then (a). The smaller cones also exhibited lower threshold voltages for the current onset. For example, the threshold voltages of nozzles (a), (b), and (c) were 12.0-12.5 kV, 10-10.5 kV, and 7.5-8.5 kV respectively. The threshold voltage was very sharply defined for each individual cone and remained constant with prolonged operation. An important factor in obtaining emission from any nozzle was the ability of the liquid metal to wet the nozzle. Sufficient wetting occurred only after removal of the oxide layer from the nozzle surface.

A typical current pulse shape produced by nozzles (b) and (c), as shown in Fig. 58 (a) and (b), consisted of a 2 nsec rise time,

(a) (b) (c)

Figure 57. Photomicrographs of the liquid metal cone formed in the nozzle (b) structure. Upper and lower horizontal lines indicate position of the cone apex and nozzle end respectively. Photo (a) shows nozzle with no applied voltage; photo (b) shows field stabilized cone just below the threshold voltage; photo (c) shows liquid metal cone during pulsed electron emission.

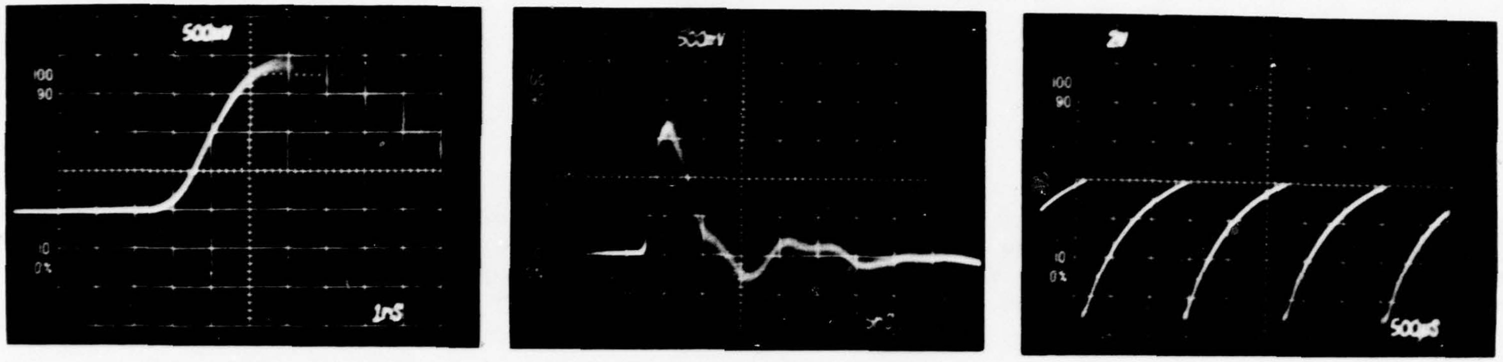

(a) (b) (c)

Figure 58. (a) and (b) current-time oscillograms from nozzle (b) in the repetitive free running mode where vertical scale is 15 A/division and horizontal scales are 1 and 5 nsec/division respectively. (c) repetitive traces of the anode voltage time curves showing the RC charging after each current pulse; vertical scale 2 kV/division and horizontal scale 0.5 msec/division.

3 to 5 nsec full width at half maximum (FWHM) and, 40 to 60 A peak current. Nozzle (a) gave a slightly different pulse shape which consisted of a 3 nsec rise time, 5 nsec FWHM and 90 to 120 A peak current. The ringing and broadening of the trailing edge of the pulse was due to external circuit factors. For any combination of load resistor R_L and voltage the pulse shape was unchanged although, with increase in average current, the peak current increased slightly.

The pulse rep rate was governed by R_L, stray tube capacitance C and power supply voltage. The voltage time trace at the anode, shown in Fig. 58 (c) for R_L = 50 mΩ, exhibits a form typical of an $R_L C$ charging, where C = 12 μμf. The remarkably sharp value of the threshold voltage at 8.0 kV is clearly depicted by the sudden drop in anode voltage as the current pulse short circuits the diode. Accordingly, the reciprocal of the charging time of the diode or, alternatively, the pulse rep rate increased with power supply voltage and decreased with increasing R_L as shown in Fig. 59. The measured value of the pulse rep rate varied from 40 to 8 x 10^4 pps corresponding to average currents of 4 μA to 6.5 mA respectively. The latter value was obtained from nozzle (c) at 10.6 kV for R_L = 0. This current was sufficient to heat the extractor electrode to a red glow within several seconds. Therefore, large rep rates with correspondingly higher average currents were not investigated.

Since the pulse shape was independent of the current limiting resistor and applied voltage, the average current was proportional to the rep rate as shown by comparing Figs. 59 and 60. The calculated average current based on the magnitude, duration and frequency of the individual pulse agreed with the measured average current.

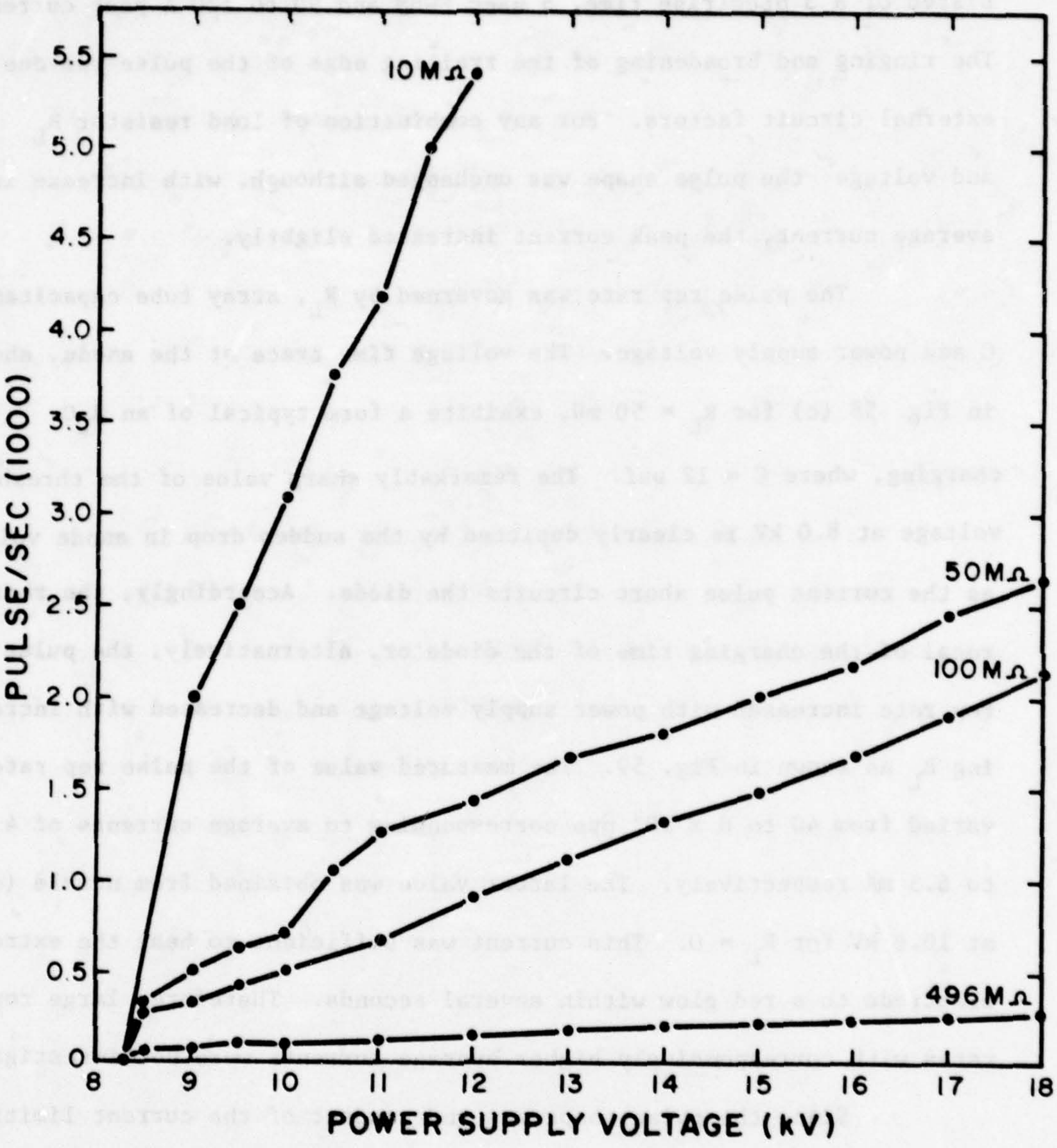

Figure 59. Electron emission pulse frequency vs voltage for various current limiting resistor values for nozzle (c).

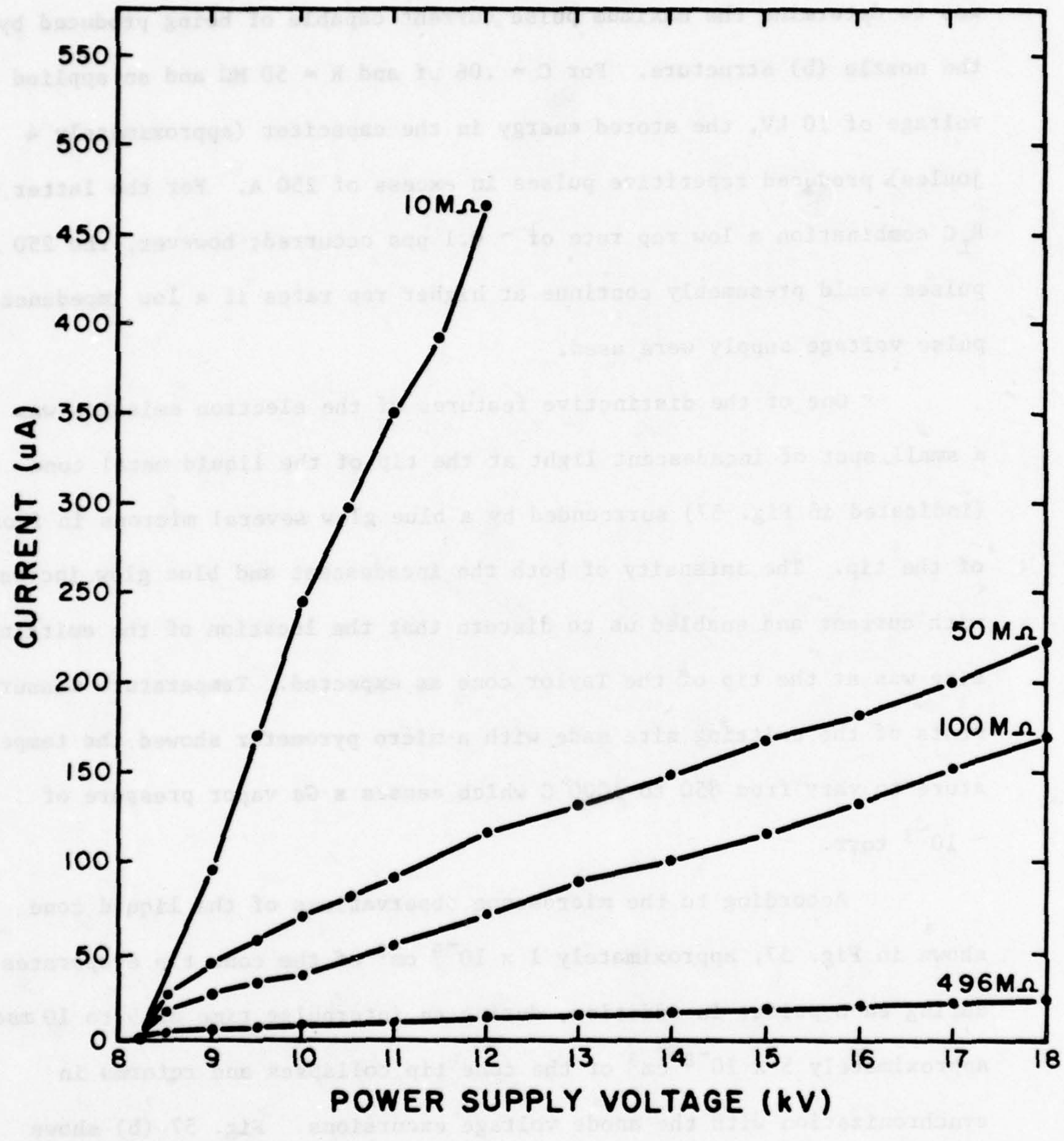

Figure 60. Average electron emission current vs voltage for various current limiting resistor values for nozzle (c).

In a separate experiment the anode shown in Fig. 55 was connected to ground through an external capacitor. The object of this arrangement was to determine the maximum pulse current capable of being produced by the nozzle (b) structure. For $C = .06\ \mu f$ and $R = 50\ M\Omega$ and an applied voltage of 10 kV, the stored energy in the capacitor (approximately 4 joules) produced repetitive pulses in excess of 250 A. For the latter $R_L C$ combination a low rep rate of ~ 0.1 pps occurred; however, the 250 A pulses would presumably continue at higher rep rates if a low impedance pulse voltage supply were used.

One of the distinctive features of the electron emission was a small spot of incadescent light at the tip of the liquid metal cone (indicated in Fig. 57) surrounded by a blue glow several microns in front of the tip. The intensity of both the incadescent and blue glow increased with current and enabled us to discern that the location of the emitting site was at the tip of the Taylor cone as expected. Temperature measurements of the emitting site made with a micro pyrometer showed the temperature to vary from 850 to 1000°C which causes a Ga vapor pressure of $\sim 10^{-3}$ torr.

According to the microscope observations of the liquid cone shown in Fig. 57, approximately $1 \times 10^{-9}\ cm^3$ of the cone tip evaporates during each pulse; in addition, during an interpulse time of 5 to 10 msec approximately $5 \times 10^{-8}\ cm^3$ of the cone tip collapses and reforms in synchronization with the anode voltage excursions. Fig. 57 (b) shows the cone formation just prior to the triggering of a pulse. From Fig. 57 (c), which shows the cone during pulsing at 85 pps, one can determine the position of the cone apex, as indicated, from the incadescent glow.

In addition, one can observe the profile of the cone just after evaporation, but before relaxation, of the cone tip. Because of the limited average time the cone exists in its smallest radius state, it was not possible to establish an experimental lower limit of the apex radius prior to pulse initiation.

The divergent electron beam emission distribution entirely filled the viewing screen and showed no discernable structure. Beam angular distribution measurements obtained from the relative density of negatives of the photographs taken of the viewing screen showed a uniform intensity with only a slight radial decrease of 1 to 3% at the far edges of the screen. Thus, the beam angular distribution is uniform over a 41° half angle. Time jitter in the free running pulse mode was less than ± 0.1 nsec. A single electron pulse could be triggered by capacitively coupling a 2 kV by 35 nsec triggering pulse in series with a D.C. bias voltage held 50 to 100 V below the threshold value for nozzle (b). The 35 nsec delay between the triggering pulse and the high current pulse, as shown in Fig. 61 (a), could be reduced to 20 nsec by increasing the magnitude of the triggering pulse from 2 kV to 3 kV, as shown in Fig. 61 (b). By increasing the D.C. bias closer to the threshold value for a free running pulse mode the triggering pulse could be reduced to 100 V.

Prior to application of the triggering pulse the D.C. bias voltage maintains a field stabilized cone shape as shown in Fig. 57 (b). Thus, during application of the triggering pulse the cone must grow from the Fig. 57 (b) shape to the sharp apex cone shape structure from which the explosive emission occurs.

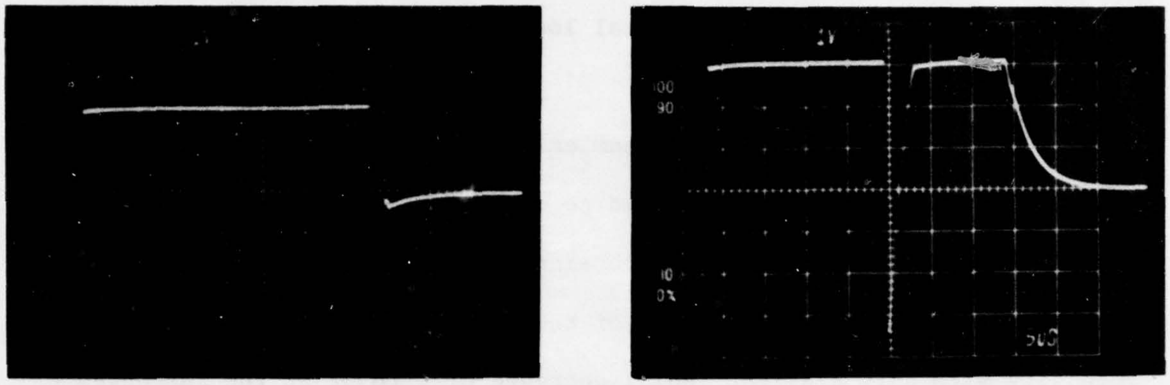

(a) (b)

Figure 61. Oscilloscope traces of a 35 μsec voltage pulse capacitively coupled to the anode with an applied D.C. bias voltage of 8.7 kV. Vertical scale is 1 kV/division. The discontinuity at the end (photo a) and middle (photo b) of the voltage pulse is due to the explosive current pulse.

A preliminary life study of the nozzle (c) structure was carried out during which time it operated continuously for 8 hrs. at an average current of 100 μA. No adjustment of the liquid Ga supply was required during the life test. In a separate experiment it was determined that the average emission current was unaffected by a background pressure between 10^{-3} and 10^{-8} torr.

D. Ion Emission Results

Ion emission exhibited three different modes of operation, a dc mode, high frequency mode, and a pulse mode. The dc mode emission was characterized by a large current, 1 to 500 μA, which was strongly voltage dependent as shown by typical data plotted in Fig. 62. A peak dc current of 500 μA was obtained at 11 kV and 10 MΩ current limiting resistance. This current was maintained only for several seconds because of excessive heating of the nozzle from secondary electron bombardment. For this reason, higher currents were not investigated.

In the high frequency mode the collected current exhibited a non-uniform high frequency on the order of 100 KHz. This mode always degenerated into the dc or pulse mode usually within several and always within 20 seconds.

The pulse mode has the same characteristics as the electron pulse and mode except the ion pulse is smaller, slower use time, slower pulse rate and smaller average currents. A typical pulse, as shown in Fig. 63, is 140 μA in magnitude and 20 usec in duration (half-maximum). During all modes of ion emission there was an incandescent glow surrounded by a blue glow present at the emitting site. Temperature measurements of

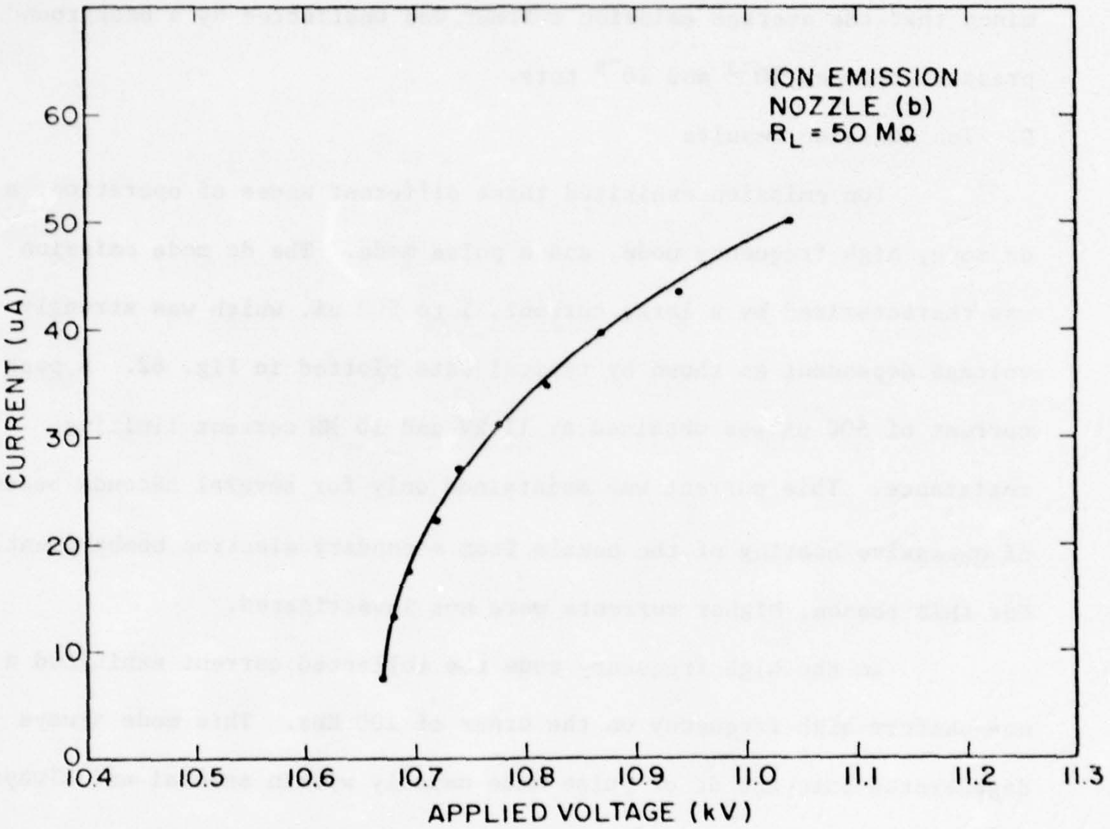

Figure 62. Curve shows the Ga ion current vs the voltage applied to the tube.

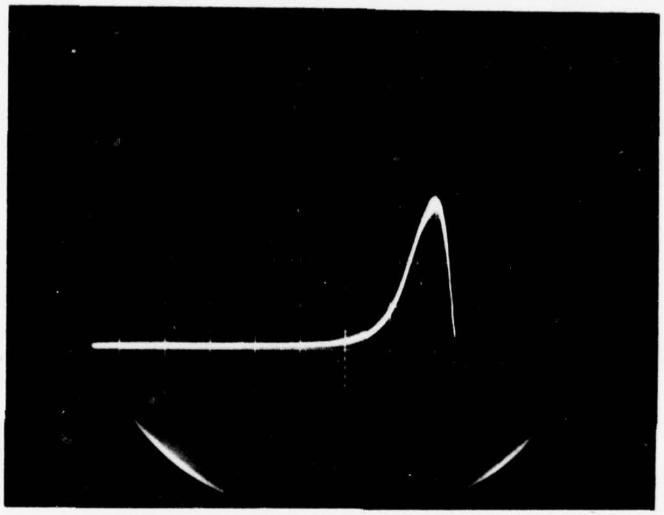

Figure 63. Pulse mode ion emission from nozzle (b). Vertical scale .40 μA/division; horizontal scale 20 μsec/div. Applied voltage 12.05 kV. Pulse repetitive rate 1430 sec^{-1}.

the incandescent glow made with a micropyrometer revealed the tip temperature to be 800 - 1000 C during both the pulse and dc emission modes.

The nozzle configuration had a major effect in determining which mode of emission was obtained. The most stable emission was produced by nozzle (c). With this nozzle the dc emission mode was dominant throughout all combinations of load resistance and applied voltage and the pulse and high frequency modes were rarely seen. The stability of operation obtained from this configuration was demonstrated by two life tests, which resulted in 15 and 25 hours of continuous dc emission. The current was a steady 35 μA at a power supply voltage of 11 KV and current limiting resistance of 100 MΩ.

Stable dc ion emission was easily obtained from nozzle (b), although the pulse and high frequency modes were observed during initial operation of the nozzle. The addition of a .0005 mf capacitor to ground on the high voltage side of the mode aided in obtaining dc emission.

Primarily pulse emission was observed with nozzle (a) with only a limited amount of dc emission. It was obtainable only with a 10 MΩ current limiting resistor in a limited power supply voltage range of 12-14 kV and could be maintained for approximately 60 seconds before it would degenerate into either the pulse or high frequency mode.

During dc emission a circular emission pattern centered on the nozzle's vertical axis could be observed on the phosphor screen. The pattern was uniform in intensity with well defined edges. The pattern size remained constant for all current values with the edges becoming slightly less defined as the current increased. The edges of the circular pattern correspond to a 18° emission half-angle which results in 62 and 308 μA sr^{-1} for total currents of 20 and 100 μA respectively.

Photographs of the liquid Ga cone forming and during dc ion emission are shown in Fig. 64. With careful examination one can see the incandescent glow present at the emitting site in Fig. 64(d). The cone appears to approach the theoretical half-angle of 49.3° during emission.

E. Discussion

For the liquid surface to exhibit a stable geometry it is necessary for the electrostatic stress, f_e, normal to the surface to be exactly balanced by the surface tension force, f_s. Taylor[41] has treated this problem in some detail. The electrostatic stress and the surface tension forces are given respectively by

$$f_e = \frac{F^2}{8\pi} \tag{39}$$

$$f_s = \gamma_s \left(\frac{1}{\rho_1} + \frac{1}{\rho_1} \right) \tag{40}$$

where γ_s is the surface tension and ρ_1 and ρ_2 are the principle radii of curvature. For a sphere, infinitely long cylinder, and a cone Eq.(40) becomes respectively

$$f_s \text{ (sphere)} = \frac{2\gamma_s}{\rho} \tag{41}$$

$$f_s \text{ (cylinder)} = \frac{\gamma_s}{\rho} \tag{42}$$

$$f_s \text{ (cone)} = \frac{\gamma_s \cot\alpha}{r} \tag{43}$$

where ρ is the respective radii, and α is the half cone angle and r is the distance along the cone axis from the apex. Combining the above equations

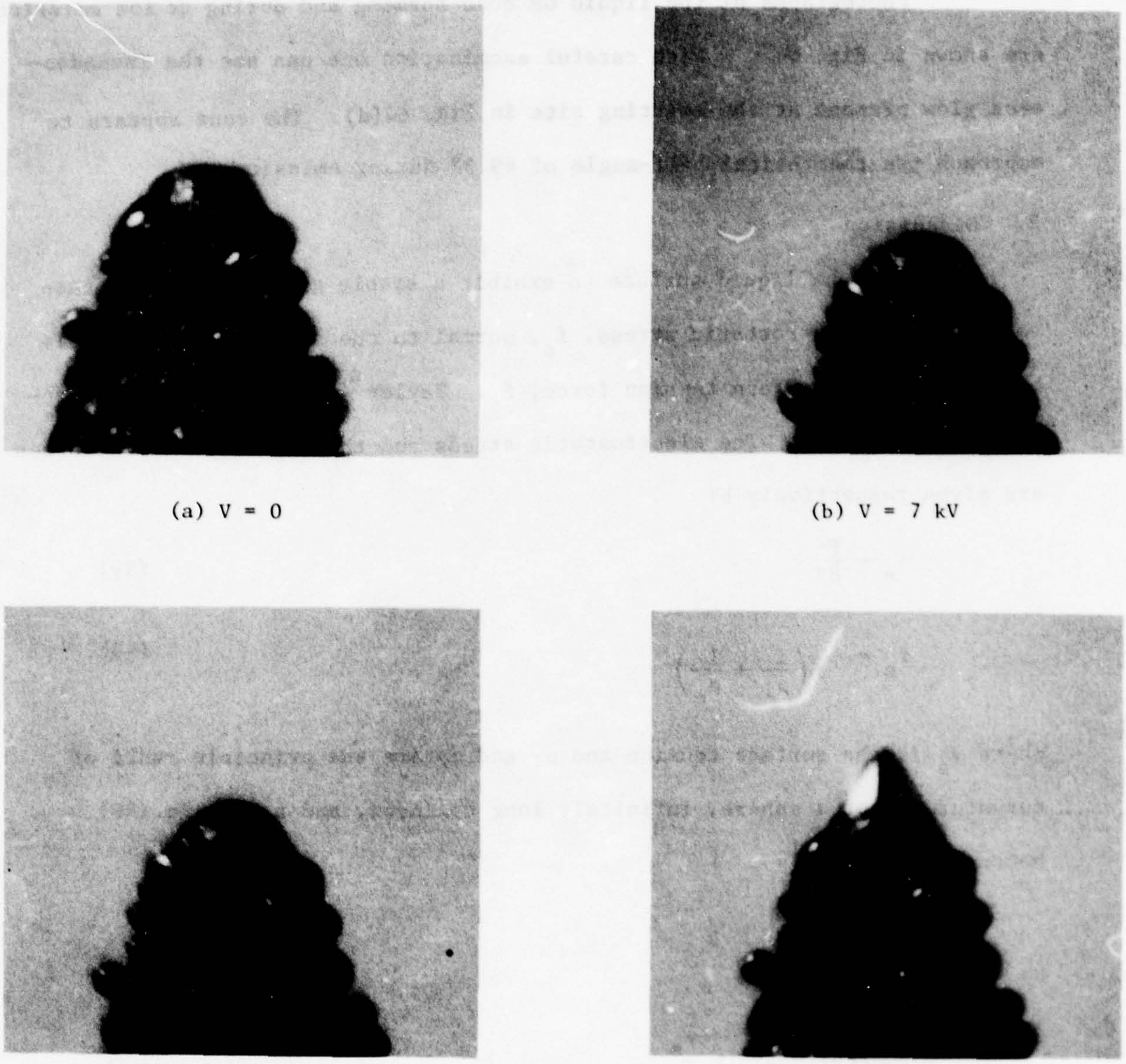

(a) V = 0

(b) V = 7 kV

(c) V = 8 kV

(d) V = 8.5 kV

Figure 64. Cone formation at the indicated voltages during ion emission from nozzle (b).

with Eq. (39), the conditions for equilibrium between the external electrostatic stress and the internal surface tension forces are

$$F\ (\text{sphere}) = 4\left(\frac{\pi\gamma_s}{\rho}\right)^{1/2} \tag{44}$$

$$F\ (\text{cylinder}) = \left(\frac{8\pi\gamma_s}{\rho}\right)^{1/2} \tag{45}$$

$$F\ (\text{cone}) = \left(\frac{8\pi\gamma_s\ \cot\alpha}{r}\right)^{1/2} \tag{46}$$

For the cone, the angle α must be found such that electrostatic and surface tension forces exactly balance along the cone. Taylor[41] showed that this occurred only if $\alpha = 49.3°$, in which case Eq.(46) becomes

$$F\ (\text{cone}) = .93\left(\frac{8\pi\gamma_s}{r}\right)^{1/2} \tag{47}$$

Most experimental studies have confirmed that the liquid surface under the influence of electrostatic forces forms a cone of half angle $\alpha \cong 49.3°$ as predicted. However, it is not known what actual geometry and radius the liquid surface assumes at the apex of the cone. A cone which approaches an extremely small radius would, as shown by Eqs. (44) to (46), require a very large electric field at the apex.

Let us consider a field electron emission model based on the Fowler-Nordheim equation[44] where the current density, J, is given by

$$J = \frac{1.54 \times 10^{-6}\ F^2}{\phi}\ \exp\ (10.4/\phi)\ \left[\exp(-6.44 \times 10^7\ \phi^{3/2}/F)\right] (\text{A/cm}^2) \tag{48}$$

where J is in A/cm^2 when F is in V/cm, and the work function ϕ in eV. The total current is then approximately given by

$$I = J\bar{A} \qquad (49)$$

where $\bar{A}$ is the effective emitting area and can be approximated by $c\rho^2$, where c is a constant. If one considers the conical shaped structure to be terminated by a hemisphere, then by combining Eqs.(44), (48) and (49) one obtains the total current as a function of radius, work function, and surface tension as follows:

$$I(\text{sphere}) = \frac{6.96\, c\gamma_s \rho}{\phi} \exp(9.52/\phi) \exp\left(-2.99 \times 10^4\, \rho^{1/2}\phi^{3/2}\gamma^{-1/2}\right) \qquad (50)$$

This relation is correct for I in Amperes, ρ in cm, ϕ in eV and γ_s in dynes/cm. As shown by Fig. 65 there is a fairly well defined range of radii values between 1 to 10 Å which produce the maximum total current. Obviously, the concept of a constant value for surface tension must break down at such small values of ρ, however, this exercise shows the very sharp increase in I as ρ decreases below a few hundred angstroms. The similarity of Eqs.(44) to (46) indicates that results similar to Fig. 65 should be obtained for a cone truncated by a spherial or cylindrical geometry.

A comparison of Eqs. (44) and (47) reveals that the field required to stabilize a sphere of radius ρ and a cone truncated at $r = \rho$ differ only by a factor of 1.5. This implies that a geometry which is a combination of a cone terminated by a hemisphere is quite feasible. Some experimental studies have reported a small cylindrical column extending from the cone apex.[41]

If an anode is a distance R from the surface of the cone, the voltage required to satisfy the conditions of Eq.(47) is

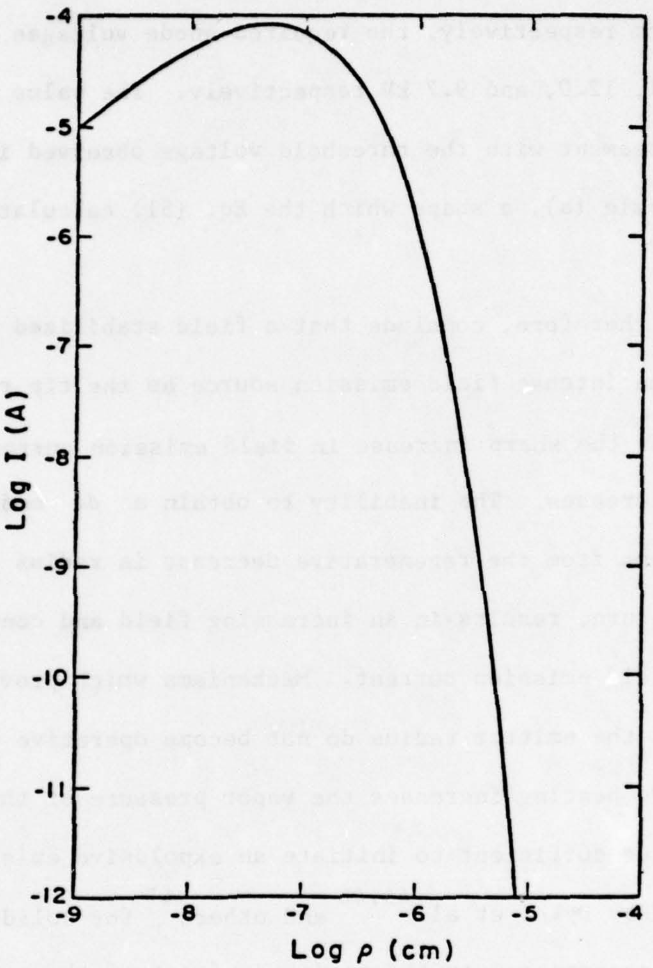

Figure 65. Plot of total current for a Ga sphere vs radius based on Eq.50 with $c = 1.0$, $\phi = 4.1$ eV and $\gamma_s = 735$ dyne/cm.

$$V\text{ (cone)} = 1.4 \times 10^3 \gamma_s^{1/2} R^{1/2} \qquad (51)$$

where V is in volts, γ_s in dynes/cm and R in cm. According to Eq.(51) the anode voltage required to stablize a liquid cone depends only on γ_s and R. For Cs, Rb, K, Ga and Hg, whose values of γ_s are 60, 76, 86, 735 and 480 dyne/cm respectively, the required anode voltages for R = 1 mm are 3.4, 3.9, 4.11, 12.0, and 9.7 kV respectively. The value of 12.0 kV for Ga is in good agreement with the threshold voltage observed in this study for the larger nozzle (a), a shape which the Eq. (51) calculation more accurately represents.

We, therefore, conclude that a field stabilized cone forms whose apex becomes an intense field emission source as the tip radius decreases. Fig. 65 depicts the sharp increase in field emission current as the cone-apex radius decreases. The inability to obtain a dc mode electron emission apparently stems from the regenerative decrease in radius of the Taylor cone tip which, in turn, results in an increasing field and concomitant rapid increase in field emission current. Mechanisms which provide a lower limit on the size of the emitter radius do not become operative until current induced resistive heating increases the vapor pressure of the liquid alloy to a critical value sufficient to initiate an expolosive emission process of the type described by Dyke, et al.[45,46] and others[47] for solid field emitters. The blue glow emanating from the region in front of the cone apex is undoubtedly due to the 4033 and 4172 Å emission lines of excited Ga atoms vaporized into the plasma which propagates the explosive emission.

A possible energy source which creates the observed localized heating is the energy exchange processes attending field emission during electron emission. This process, which has been studied previously,[48] causes the temperature of the tip T_o relative to the temperature T_1 at the base of the cone to vary according to

$$T_o - T_1 = \frac{kT_o \cot(\pi\rho)}{K} \; \frac{I}{\alpha\rho} + \frac{\rho(T_o)}{2K\pi^2} \; \frac{I^2}{\alpha\rho} \qquad (52)$$

where K is the thermal conductivity, $\rho(T)$ is the electrical resistivity, ρ is the radius of the cone at the point of truncation and p is a dimensionless parameter which is a function of electric field and work function and whose value is $0 \leq p < .7$. The first term in Eq. (52) is due to the so-called "Nottingham heating" and the second term, which dominates at high currents, is due to resistive heating. A plot of Eq. (52) in Fig. 66 shows that in order to achieve sufficient heating to produce an incandescent glow either a large current or a small radius is necessary.

Eq. (52) is the steady state solution; for pulse mode emission, when the Nottingham effect is neglected, it has been shown[49] that T_o varies with pulse length, t_o, and pulse separation, t_i, according to the expression:

$$\left(T_o - T_1\right)_{\text{pulse}} = \left(T_o - T_1\right)_{\text{dc}} \left[\frac{\frac{2t_o}{t_c}}{1 + 2.63\sqrt{\frac{t_o}{t_c}} + \frac{2t_o}{t_c}} \right] \times \left[1 + \frac{0.74}{\frac{t_i}{t_c}\sqrt{2.2 + \frac{t_i}{t_c}}} \right] \qquad (53)$$

where t_c is a time constant characteristic of the emitter material and cone half angle and given by:

$$t_c = \frac{c_v}{K\delta}\left(\frac{\rho}{\alpha}\right)^2 \qquad (54)$$

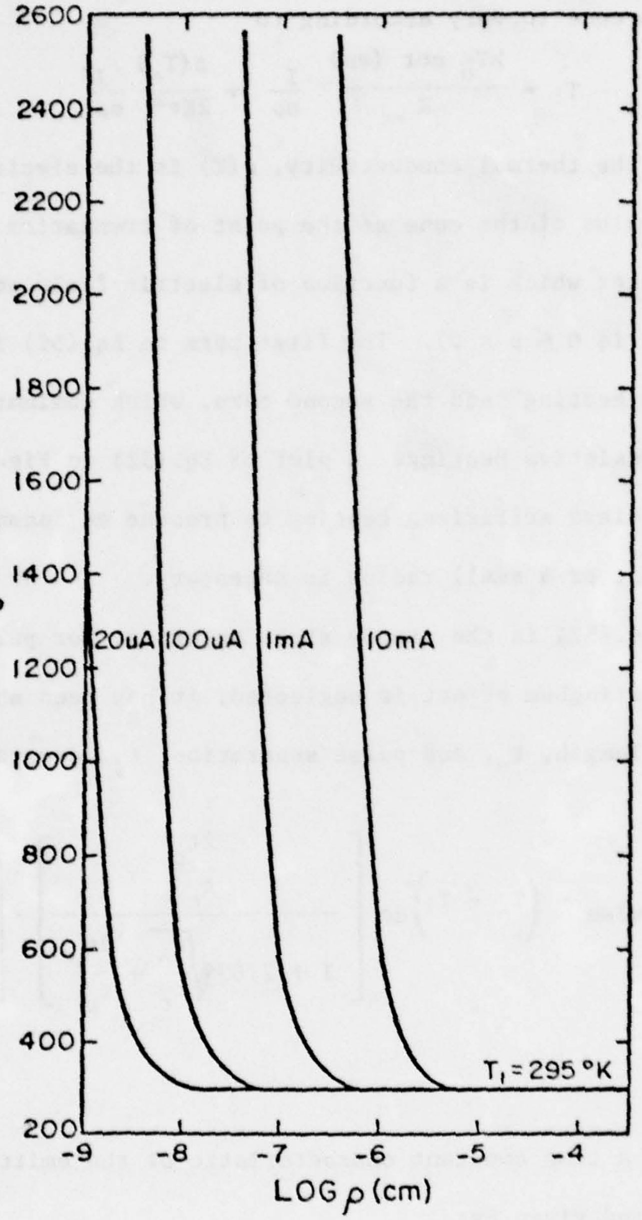

Figure 66. Apex temperature of a Ga cone due to heating by energy exchanges attending field emission vs cone apex radius. Values of $\rho(T)$ = 17.4 micro ohm-cm, K = .328 watts/cm-K were used.

where c_v is the specific heat and δ, the density of the emitter material.

The first bracket of Eq.(53) represents the effect of pulse length on T_o at the end of the pulse. For $t_o = t_c$ the tip temperature rise is 36% of the steady state value and for t_o appreciably larger than t_c, the tip is heated close to its steady state temperature during the pulse. The second bracket represents the effect of repetition rate. If t_1 is appreciably longer than t_c then almost complete cooling of the emitter tip occurs between pulses.

The Nottingham effect and vaporization are ignored in the derivation of Eq.(53) in order to obtain an analytical solution. However, the Nottingham effect causes the emitter tip to receive an additional input of energy localized at the tip at a rate which decreases as tip temperature increases. Therefore, it in effect reduces the time constant, t_c, below the value indicated by Eq.(54).

For a Ga cone of half angle 49.3° and c_v = .089 cal/gram

$$t_c \approx 200\ \rho^2 \tag{55}$$

Combining Eqs.(53) and (55) it is easily shown that during a 2 nsec pulse that $(T_o - T_1)_{PULSE} \cong .68\ (T_o - T_1)_{DC}$ for $\rho = 100$ Å. Furthermore, for $\rho < 100$ Å we find that the temperature rise at the end of the 2 nsec pulse is equal to the respective steady state temperature given in Fig. 66. Thus, if $\rho < 100$ Å one may surmise from Fig. 66 that a D.C. current of ~ 10 mA is sufficient to account for the observed emitter temperature rise of 1000°. According to the field stabilized field emission model described by Eq.(50) and Fig. 65, it is readily shown that if $c \cong 5$ and $\phi = 3$ eV, then the required emitter radius to achieve an emission current level in excess of 1 mA, and to initiate the observed plasma induced explosive emission, is ~ 100 Å. Thus a self consistency between the emission heating mechanisms and the field emission, field stabilized cone model has been achieved.

Further evidence that the expolsive emission process is field emission initiated is given by the amplified oscilloscope trace of the leading edge of the Fig. 58(a) pulse shown in Fig. 67. The slow linear increase in current for ~ 3 nsec prior to the onset of the explosive current increase is believed to be a pure field emission current which increases with decreasing radius of the cone apex. Upon reaching a value $\tilde{>}$ 40 mA the plasma induced explosive emission mode, initiated by the above mentioned emission heating, occurs with a rapid current increase which ultimately terminates as a small protion of the apex is volatilized. Thus, a consistent set of experimental results have been obtained which supports the model put forth to explain this unusual electron source.

Let us next consider ion emission from liquid metals based on a field evaporation model. The field required for field evaporation, assuming singly charged ionic species being emitted, is approximately given by the following expression[38]

$$F_{FE} = e^{-3}\left(H_{vap} + I - \phi - kT\,\ell n\,\frac{\tau}{\tau_o}\right)^2 \qquad (56)$$

or

$$F_{FE} = .069\left(H_{vap} + I - \phi - kT\,\ell n\,\frac{\tau}{\tau_o}\right)^2 \ (V/Å)$$

where H_{vap} is the heat of vaporization, I, the ionization potential, τ, the lifetime in respect to field evaporation and $\tau_o \cong 10^{-12}$ sec. The second expression is correct for H_{vap}, I, kT and ϕ in eV and F in V/Å.

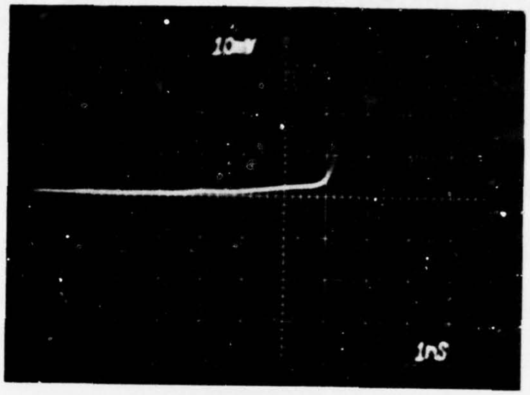

Figure 67. Current-time oscillogram as in Figure 58 but with vertical scale 0.30 A/division.

The maximum radius, r_{vap}, of a conducting liquid cone where the evaporation fields have the required magnitude for atomic ion emission is easily obtained by substituting values of F_{FE} into Eq.(47). Values of r_{vap}, F_{FE} at 300°K, and other relevant parameters for several liquids are listed in Table 7.

TABLE 7

EVAPORATION FIELDS FOR ION EMISSION FROM LIQUIDS

Element	Vaporization Energy H_{vap} (eV)	Ionization Potential I (eV)	Work Function ϕ (eV)	Surface Tension γ (dyn/cm)	Evaporation Field F_{FE} (V/Å)	Evaporation Radius r_{vap} (Å)
Cs	.81	3.87	1.81	60	.36	10.5
Rb	.85	4.16	2.09	76	.32	16.8
K	.93	4.32	2.24	86	.40	12.1
Na	1.12	5.12	2.28	206	.78	7.7
Ga	2.82	5.97	4.12	735	1.14	12.8
Hg	.64	10.39	4.53	480	2.44	1.8

Small charged droplets, rather than ions, are in some cases emitted from the cone. Mahoney et. al.[38] concluded that ion, as opposed to droplet, formation will occur if the tensile strength of the liquid is large compared to the electrostatic stress required for field evaporation, i.e. f_t/f_e is large. The theoretical tensile strength of a liquid column can be estimated by

$$f_t = 2\gamma_s/r_o \tag{57}$$

where r_o is the interatomic spacing. Mahoney, et. al.[38] have tabulated values of r_o, f_t, and f_e which are reproduced in Table 8.

TABLE 8

RATIO OF SURFACE ELECTROSTATIC STRESS AT ION EVAPORATION FIELD STRENGTHS TO THEORETICAL STRESSES NECESSARY TO RUPTURE A LIQUID COLUMN

Element	Interatomic Distance r_o (Å)	Tensile Strength $f_t \times 10^{10}$ (dyn/cm^2)	Electrostatic Stress $f_e \times 10^{10}$ (dyn/cm^2)	Force Ratio f_t/f_e
Cs	5.31	.226	.0545	4.15
Rb	4.97	.307	.0428	7.15
K	4.70	.365	.0691	5.28
Na	3.70	1.12	.263	4.26
Ga	2.77	5.3	.562	9.43
Hg	3.07	3.14	2.57	1.22

A favorable material for liquid field evaporation and field electron emission should possess a large f_t/f_e force ratio, be a conducting liquid at room temperature, and have a large H_{vap} value, or alternatively a low vapor pressure. The latter property limits the gas phase electron impact ionization of the material during electron emission and limits the gas phase ionization during ion emission.

Heating of the cone by electron or ion bombardment was shown by Clampitt[50] to vary according to

$$T_o - T_1 = \frac{IV}{K\pi\tan\theta}\left(\frac{1}{r_o} - \frac{1}{r_1}\right) \qquad (58)$$

where I and V are the incident current and energy respectively and r_o and r_1 are the radii of the cone at T_o and T_1 respectively. Since usually $r_1 \gg r_o$, the $1/r_1$ term can be ignored.

To achieve sufficient heating by this means, as shown by Fig. 68, either a relatively large IV value or a small radius is necessary. A large IV value is easily obtained if the bombarding particles originate at or near the screen and thereby are accelerated by ≈ 10^4 volts. However, these particles would strike the entire cone and result in unlocalized heating. Also, preliminary experiments in preferential biasing of the screen to eliminate particles originating at the screen form reaching to the emitter seem to produce no reduction in the localized heating. Thus, it appears the incident particles must originate close to cone meaning they possess only a few eV in energy and to achieve a large IV value necessitates a relatively large incident current. This seems feasible in the ion mode of operation but in the electron mode it seems unlikely to have as large incident ion current. Therefore, in order to create sufficient heating by this process a small radius is required.

The presence of the blue glow or excited Ga atoms in the space surrounding the cone is an unexpected result considering the very low vapor pressure of Ga. The vapor pressure, P, of a curved surface of radius r, relative to a flat surface is given by.[43]

$$\ln\left(\frac{P}{P_o}\right) = \frac{2\gamma V_m}{RTr} \qquad (59)$$

where V_m is the molar volume. Table 9 lists values of P for various radii and temperature and shows that the vapor pressure becomes large for radii less than 10 Å.

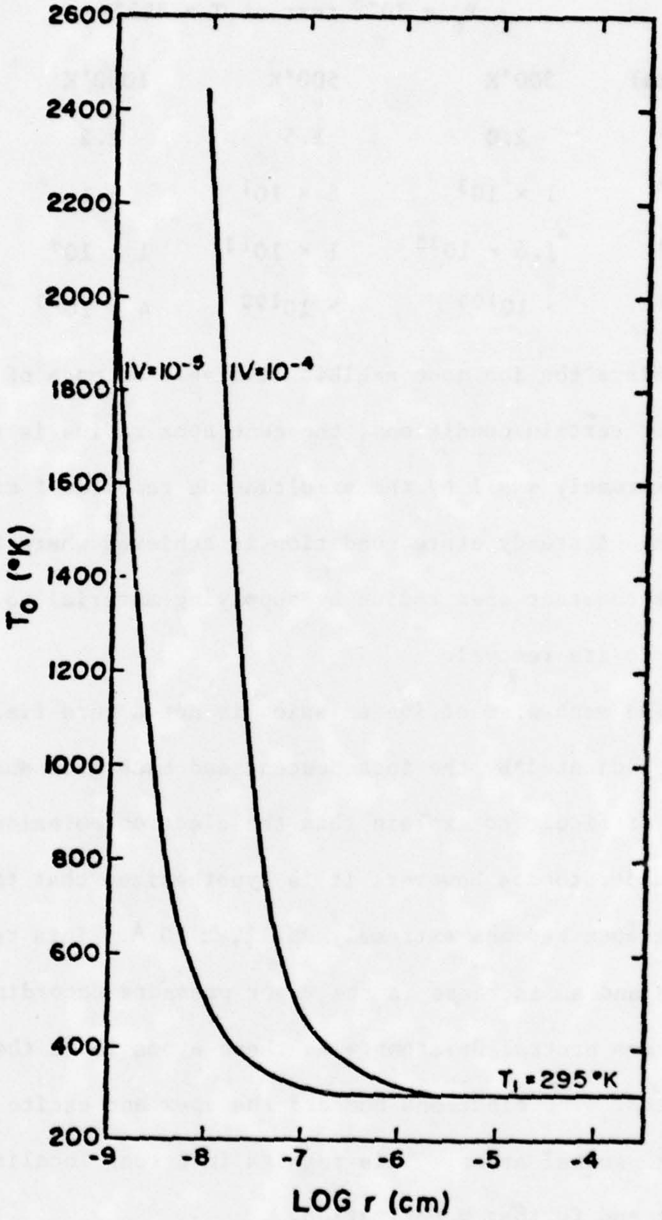

Figure 68. Apex temperature of a Ga cone due to heating by bombardment vs apex radius.

TABLE 9

VALUES OF P/P_o FOR A Ga CURVED SURFACE OF RADIUS r

$P_o = 10^{-8}$ torr at T = 825°K.

r (cm)	300°K	500°K	1000°K	2000°K
10^{-6}	2.0	1.5	1.2	1.1
10^{-7}	1×10^{3}	6×10^{1}	8.1	2.8
10^{-8}	1.6×10^{30}	1×10^{13}	1×10^{9}	3×10^{4}
10^{-9}	$> 10^{100}$	$> 10^{100}$	4×10^{90}	2×10^{45}

Since the ion mode exhibits a stable dc mode of operation, apparently, under certain conditions, the cone apex radius is prevented from becoming extremely small by the simultaneous removal of material by field evaporation. A steady state condition is achieved where the cone is maintained at a constant apex radius by supplying material to the apex at a rate equal to its removal.

The mechanism of ion emission is not a pure field evaporation process as indicated by the incandescent and blue glow and high currents. It is more difficult to explain than the electron emission process and is not fully understood. However, it is hypothesized that the radius of the liquid cone apex becomes extremely small, $\simeq 10$ Å. This results in field evaporation and an increase in the vapor pressure according to Eq.(59), which releases neutral Ga atoms. As these atoms leave the tip they are field ionized. The electrons bombard the apex and excite some to the evaporating neutral atoms. This results in strong localized heating of the apex and further vaporization.

A space charge effect would seem possible with the high density of Ga ions surrounding the emitter. Such an effect would result in the current showing a dependence on the $V^{3/2}$ or $(V - V_T{}^{3/2})$, where V_T is threshold voltage. The IV data in Fig. 62 does not exhibit such a dependence and, therefore, shows no space charge effect.

F. Conclusion and Summary

A novel, repetitive pulsed electron and dc ion source employing a liquid Ga/12% In cathode has been described. Repetitive current pulses as large as 250 A with an applied voltage of only 10 to 12 kV have been observed. The mechanism involves the formation of a field stabilized cone of the liquid cathode which forms a sufficiently small apex radius that a regenerative field electron current initiates an explosive emission process of the type described in detail for solid state emitters.[45-47,51] If the applied voltage is held just below threshold, a 100 V by 35 nsec pulse voltage is sufficient to initiate the high current pulse.

Several important differences between the liquid and solid phase explosive emission electron sources have been revealed. First, after the vaporization of a small amount of material from the cone apex during the pulse, the liquid phase source self heals, thereby yielding a repetitive pulse mode operation with a constant applied voltage. Secondly, there is no limit to the life, i.e., the number of pulses, attainable from the liquid emitter. Third, the current pulse rise time and duration are shorter for the liquid metal source. A remarkable feature of the liquid metal electron source when operated in the free running repetitive mode is the lack of measurable time jitter, < 0.1 nsec, between the onset of successive pulses and their uniform amplitude over the rep rate range 40 to 8×10^4 pps.

In the dc ion emission mode an angular intensity between 60 and 300 mA sr^{-1} has been measured. Thus, an extraordinary bright ion source has been demonstrated which provides a stable unattended dc current for several hours. Further studies involving the measurement of the total energy distribution and spectral distribution of the blue light will be necessary before the emission mechanism can be completely understood. At present a modified field evaporation mechanism appears to be most plausible.

We have calculated that with a simple accelerating two element electrostatic lens that several nA of Ga ion current could be focussed into a 0.1 μm beam spot size at 60 kV even if the energy spread was ~ 10 eV. Hopefully, this type of source will also be suited for ion beam information recording applications.

Presumably, other liquid metals which form a stable Taylor cone can be used in place of the Ga/12% In alloy employed in this study. It will be of interest to learn from future study whether properties of the liquid metal such as vapor pressure, resistivity, surface tension, etc. have perceptible effect on the emission characteristics.

REFERENCES

1. Oppenheimer, J. R., "Three Notes on the Quantum Theory of Aperiodic Effects," Phys. Rev, Vol. 31, pp 66-81, (1928).

2. Fowler, R. H. and Nordheim, L. W., "Electron Emission in Intense Electric Fields," Proc. Roy. Soc., Vol. A119, p 173 (1928).

3. Müller, E. W., "Electron-microscopic Observations upon Field Cathodes," Z. Physik, Vol. 106, p 541 (1937); "The Field-ion Microscope," Z. Physik, Vol. 131, p 136 (1951).

4. Langmuir, D. B., "Theoretical Limitations of Cathode Ray Tubes," Proc. Inst. Radio Eng., Vol. 25, p 977 (1937).

5. Worster, J., "The Brightness of Electron Beams," J. Phys., Vol. D2, p 457 (1969).

6. Worster, J., "The Brighness of Electron Emission Systems," J. Phys., Vol. D2, p 889 (1969).

7. Swanson, L. W. and Bell, A. E., "Recent Advances in Field Electron Microscopy," Adv. Elect. and Electr. Phys., Vol. 32, p 193 (1973).

8. Veneklasen, L. H., "Some General Considerations Concerning the Optics of the Field Emission Illumination System," Optik, Vol. 36, p 410 (1972).

9. Wiesner, J. C. and Everhart, T. E., "Point Cathode Electron Sources. Electron Optics of the Initial Diode Region," J. Appl. Phys., Vol. 44, p 2140 (1973).

10. Dyke, W. P., Trolan, J. K., Dolan, W. W., Barnes, G, "The Field Emitter: Fabrication, Electron Microscopy, and Electric Field Calculations," J. Appl. Phys., Vol. 24, p 570 (1953).

11. Orloff, J. and Swanson, L. W., "Study of a Field-ionization Source for Microprobe Applications," J. Vac. Sci. Technol., Vol. 12, p 1209 (1975).

12. Swanson, L. W. and Crouser, L. C., "Angular Confinement of Field Electron and Ion Emission," J. Appl. Phys., Vol. 40, p 4741 (1969); L. W. Swanson, "Comparative Study of the Zirconiated Built-up W Thermal-field Cathode," J. Vac. Sci. and Technol., Vol. 12, p 1228 (1975).

13. Swanson, L. W., and Martin, N. A., "Field Emission Cathode Stability Studies: Zirconium/Tungsten Thermal Field Cathode," J. Appl. Phys., Vol. 46, p 2029 (1975).

14. Wolfe, J. E., Ledges, G. E., Glascock, H. H., U.S. Patent 3,814,975 (1974).

15. Müller, E. W., and Tsong, T. T., Field Ion Microscopy, American Elsevier Publishing Co., p 120 (1969).

16. Elinson, M. I., and Kundintsevo, G. A., "Field Emission Cathodes of High-melting Metal Compounds," Rad. Eng. Elect. Phys., Vol. 7, p 1417 (1962).

17. Windsor, E. E., "Construction and Performance of Practical Field Emitters from Lanthanum Hexaboride," Proc. IEE, Vol. 116, p 348 (1969).

18. Swanson, L. W., Dickinson, J. T., and McNeely, D. R., "Fabrication and Surface Characterization of Composite Refractory Compounds Suitable for Thermionic Converters," NASA Contractor Report No. CR-2668 (1976).

19. Lebeau, P., and Eiguras, J., Compt. Rend. Vol. 127, p 393 (1898).

20. Aito, T., Kawabe, U., and Honda, Y., "Single Crystal Growth of Lanthanum Hexaboride in Molten Aluminum," Japan J. Appl. Phys., Vol. 13, p 391 (1974).

21. Verhoeven, J. D., Gibson, E. D., Noack, M. A., Conzemius, R. J., "An Arc Floating Zone Technique for Preparing Single Crystal Lanthanum Hexaboride," J. Cryst. Growth, Vol. 36, p 115 (1976).

22. Post, B., Moskowitz, D., and Glaser, F. W., "Borides of Rare Earth Metals," J. Am. Chem. Soc., Vol. 78, p 1800 (1956).

23. Barbour, J. P., Charbonnier, F. M., Dolan, W. W., Dyke, W. P., Martin, E. E., and Trolan, J. K., "Determination of the Surface Tension and Surface Migration Constants for Tungsten," Phys. Rev., Vol. 117, p 1452 (1960).

24. Good, R. H. and Müller, E. W.,

Handbuch der Physik, Vol. 21, p 176 (1956).

25. Bober, K. and Mireva, Z., "Study of Mercury Surface Diffusion on Tantalum With and Without an Electric Field by Means of a Field Emission Microscope," Surface Science, Vol. 51, p 513, (1975); Wang, J. L., and Vanselow, R., "Activation Energy for Surface Self-Diffusion of TA and Influence of Residual Gases on this Quantity in the Presence of High Electric Fields," Surface Science, Vol. 43, p 21 (1974).

26a. Barbour, J. P., Charbonnier, F. M., Dolan, W. W., Dyke, W. P., Martin, E. E., Trolan, J. K., "Determination of the Surface Tension and Surface Migration Constants for Tungsten," Phys. Rev., Vol. 117, p 1452 (1960).

26b. Bettler, P. C., Charbonnier, F. M., "Activation Energy for the Surface Migration of Tungsten in the Presence of a High-Electric Field," Phys. Rev., Vol. 119, p 85 (1960).

27. Bettler, P. C., Barnes, G., "Field-Emission Studies of Surface Migration for Tungsten, Rhenium, Iridium, and Rhodium," Surface Science, Vol. 10, p 165 (1958).

28. Melmed, A. J., "Surface Self-Diffusion of Nickel and Platinum," J. Appl. Phys., Vol. 38, p 1885 (1967).

29. Gadzuk, J. W., Plummer, E. W., "Energy Distributions for Thermal Field Emission," Phys. Rev. B, Vol. 3, p 2125 (1971).

30. Murphy, E. L., Good, R. H., "Thermionic Emission, Field Emission, and the Transition Region," Phys. Rev., Vol. 102, p 1464, (1956).

31. Gadzuk, J. W., Plummer, E. W., "Hot-Hole Electron Cascades in Field Emission from Metals," Phys. Rev. Lett., Vol. 26, p 92 (1971).

32. Gadzuk, J. W., Lucas, A. A., "Field Emission Tails and Tunneling Lifetimes," Phys. Rev. B, Vol. 7, p 4770 (1973).

33. Hasker, J., "Anomalous Electron Velocity Distributions," Philips Res. Repts., Vol. 24, p 263 (1969).

34. Dyke, W. P., Dolan, W. W., "Field Emission," Advances in Electron Phys., Vol. 8, p 89 (1956).

35. Lea, C., Gomer, R., "Evidence of Electron-Electron Scattering from Field Emission," Phys. Rev. Lett., Vol. 25, p 804 (1970).

36. Krohn, V. E., Ringo, G. R., "Ion Source of High Brightness Using Liquid Metal," Appl. Phys. Lett., Vol. 27, p 479 (1975).

37. Clampitt, R., Aitken, K. L., Jefferies, D. K., "Abstract: Intense Field-emission Ion Source of Liquid Metals," J. Vac. Sci. Technol., Vol. 12, p 1208 (1975).

38. Mahoney, J. F., Yahiku, A. T., Daley, H. L., Moore, R. D., Perel, J., "Electrohydrodynamic Ion Source," J. Appl. Phys., Vol. 40, p 5101 (1969).

39. Swatik, D. S., Hendricks, C. D., "Production of Ions by Electrohydrodynamic Spraying Techniques," AIAA J., Vol. 6, p 1596 (1968).

40. Colby, B. W., Evans, C. A., Jr., "Electrohydrodynamic Ionization Mass Spectrometry," Anal. Chem., Vol. 45, p 1887 (1973).

41. Taylor, G., "Disintegration of Water Drops in an Electric Field," Proc. Roy. Soc. (London), Vol. A280, p 383 (1964).

42. Kelman, L. R., Wilkinson, W. D., Yaggee, F. L., Resistance of Materials to Attack by Liquid Metals, Argonne Nat'l. Lab., p 4417 (1950).

43. Green, M., Solid State Surface Science, Marcel Dekker, New York (1973).

44. Swanson, L. W., Martin, N. A., "Field Emission Cathode Stability Studies: Zirconium/Tungsten Thermal Field Cathode," J. Appl. Phys., Vol. 46, p 2029 (1975).

45. Dyke, W. P., Trolan, J. K., Martin, E. E., Barbour, J. P., "The Field Emission Initiated Vacuum Arc. I. Experiments on Arc Initiation," Phys. Rev., Vol. 91, p 1043 (1953).

46. Dolan, W. W., Dyke, W. P., Trolan, J. K., "The Field Emission Initiated Vacuum Arc. II. The Resistively Heated Emitter," Phys. Rev., Vol. 91, p 1054 (1953).

47. Fursei, G. N., Vorontsov-Velyminov, P. N., "A Qualitative Model of Vacuum Arc Initiation: II A Field Emission Mechanism of Initiating Vacuum Arc," Soviet Phys. Tech. Phys., Vol. 12, p 1370 (1968).

48. Swanson, L. W., Crouser, L. C., Charbonnier, F. M., "Energy Exchanges Attending Field Electron Emission," Phys. Rev., Vol. 151, p 327 (1966).

49. Martin, E. E., Charbonnier, F. M., Dolan, W. W., Dyke, W. P., Pitman, H. W., Trolan, J. K., "Research on Field Emission Cathodes," Wright Air Development Division Techn. Report 59-20 (1960).

50. Clampitt, R., Aitken, K. L., Jefferies, D. K., "Field Ionisation of Liquid Caesium on Sharp Wires," ESTEC Contract Report 2050/73 (1975).

51. Zhukov, V. M., Fursei, G. N., "Explosive Electron Emission from Copper Points," Sov. Phys. Tech. Phys., Vol. 21, p 1112 (1976).

©U.S.Government Printing Office: 1979 — 657-002/01